TOPOLOGICAL STATE ENGINEERING

DISSERTATION

zur Erlangung des Grades eines

Doktors der Naturwissenschaften (Dr. rer. nat.)

am Fachbereich Physik
der Freien Universität Berlin

vorgelegt von

Sergio Acero González

Berlin, 2020

ERSTGUTACHTER: Prof. Felix von Oppen, PhD

ZWEITGUTACHTER: Prof. Dr. Piet W. Brouwer

DISPUTATION AM: 25. September, 2020

SELBSTSTÄNDIGKEITSERKLÄRUNG

NAME: Acero González
VORNAME: Sergio

Ich erkläre gegenüber der Freien Universität Berlin, dass ich die vorliegende Dissertation selbstständig und ohne Benutzung anderer als der angegebenen Quellen und Hilfsmittel angefertigt habe. Die vorliegende Arbeit ist frei von Plagiaten. Alle Ausführungen, die wörtlich oder inhaltlich aus anderen Schriften entnommen sind, habe ich als solche kenntlich gemacht. Diese Dissertation wurde in gleicher oder ähnlicher Form noch in keinem früheren Promotionsverfahren eingereicht. Mit einer Prüfung meiner Arbeit durch ein Plagiatsprüfungsprogramm erkläre ich mich einverstanden.

Berlin, 2020

Sergio Acero González

DECLARATION OF AUTHORSHIP

LAST NAME: Acero González
FIRST NAME: Sergio

I declare to the Freie Universität Berlin that I have completed the submitted dissertation independently and without the use of sources and aids other than those indicated. The present thesis is free of plagiarism. I have marked as such all statements that are taken literally or in content from other writings. This dissertation has not been submitted in the same or similar form in any previous doctoral procedure. I agree to have my thesis examined by a plagiarism examination software

Berlin, 2020

Sergio Acero González

ABSTRACT

In the past two decades theoretical and experimental efforts have brought forth numerous advances in the field of topological matter. Notably, theoretical predictions like the Quantum Spin Hall phase in mercury/cadmium telluride quantum well structures have subsequently been confirmed experimentally. Another example is the prediction of topological superconductivity in systems combining Zeeman splitting, spin-orbit coupling and conventional superconductivity which has been tentatively confirmed in various experiments. These efforts are motivating further research on how to realize systems hosting topological phases and are bringing forward the possibility of engineering physical devices using topological states of matter.

One of the first examples of the engineering of a topological phase out of topological domain-wall states was recently reported in two experiments. Also following a theoretical prediction, the experiments used graphene nanoribbons of alternating width to create an effective Su-Schrieffer-Heeger chain composed of the topological domain-wall states arising at the interfaces of nanoribbon regions of different width. In this thesis we provide a theoretical toy model that captures the basic physics of these systems. We show the possible end state configurations of the model and how the end states of the engineered topological phase can interact with those of the underlying topological system.

With most of the theoretical foundations already in place, the research has focused on finding strategies to realize topological phases in a more reliable, stable manner and provide unequivocal signatures of the sought-for topological states. Within this context, magnetic adatom chains on superconducting substrates have attracted attention as they are predicted to realize topological superconductivity and host Majorana quasiparticles at their ends. Due to an enhanced lateral extension of the Yu-Shiba-Rusinov wave functions of the magnetic adatoms in two dimensional superconductors, substrates such as $NbSe_2$ have been proposed. This enhancement increases the coupling between the adatoms leading to a more robust topological phase. In this doctoral thesis we show that the effects of the charge-density modulation present in $NbSe_2$ must be taken into account for an optimal engineering of topological superconductivity.

The signatures of the presence of Majorana quasiparticles at the ends of a topological superconducting phase are sometimes compatible with those of other (conventional) states. These states can have near-zero energies and thus be confused with the desired zero-energy Majorana quasiparticles. In this dissertation, we develop a theory of photon-assisted Andreev reflections resonantly enhanced by subgap states. Our theory is in excellent agreement with a recent experiment which shows deviations from the Tien-Gordon model, widely successful in explaining photon-assisted processes. Of relevance in its own right, our theory also provides a technique to measure near-zero energies of the subgap states. Indeed, separate threshold conditions for electron and hole tunneling processes lead to a higher sideband multiplicity in the case of small but non-zero subgap state energies. Experiments with tunable photon energies can benefit from this fact to measure the subgap state energy.

KURZFASSUNG

In den letzten zwei Jahrzehnten wurden zahlreiche theoretische sowie experimentelle Fortschritte auf dem Gebiet der topologischen Materie erzielt. Insbesondere wurden theoretische Vorhersagen, wie die Quantum Spin Hall-Phase in Quecksilber/Cadmium-Tellurid-Quantentopfstrukturen, experimentell bestätigt. Ein weiteres Beispiel ist die Vorhersage der topologischen Supraleitung in Systemen, die Zeeman-Effekt, Spin-Bahn-Kopplung und konventionelle Supraleitung kombinieren, was in verschiedenen Experimenten vorläufig bestä-tigt wurde. Diese Erkenntnisse motivieren weitere Forschung daran, wie Systeme, die topologische Phasen enthalten, konstruiert werden können und eröffnen damit die Möglichkeit der Entwicklung von physikalischen Geräten unter Verwendung topologischer Materiezustände zu konstruieren.

Vor Kurzem wurde von zwei Experimenten berichtet, in denen topologische Phasen aus topologischen Domän-Wand-Zustäden konstruiert wurden. Graphene-Nanobänder mit wechselnder Breite wurden verwendet, um ein effektives Su-Schrieffer-Heeger-Modell zu erstellen, bestehend aus topologischen Domänen-Wand-Zuständen, welche an den Grenzflächen von Nanobändern unterschiedlicher Breite entstehen. Wir stellen ein theoretisches Toy-Modell vor, welches die physikalischen Grundlagen dieser Art von Systemen beschreibt. Wir zeigen die möglichen Endzustandskonfigurationen des Modells und wie die Endzustände der konstruierten topologischen Phase mit dem des zugrunde liegenden topologischen Systems interagieren können.

Da die meisten theoretischen Grundlagen bereits vorhanden sind, fokussiert sich die Forschung darauf, Strategien zu finden, um topologische Phasen verlässlicher und stabiler herzustellen und die topologischen Zustände unverwechselbaren Signalen zuzuteilen. In diesem Zusammenhang, erlangten magnetische Adatomketten auf supraleitenden Substraten Aufmerksamkeit, da vorausgesagt wurde, dass sie topologisch supraleitend sind und an ihren Enden Majorana-Quasiteilchen aufweisen. Die Verwendung von zweidimensionalen Substraten, wie NbSe$_2$, wurde vorgeschlagen, da die Yu-Shiba-Rusinov-Wellenfunktionen der magnetischen Adatome seitlich langsamer abfallen als bei dreidimensionalen Supraleitern. Dies erhöht die Kopplung zwischen Zuständen, was zu einer robusteren topologischen Phase führt. Wir zeigen, dass die Auswirkungen der Ladungsdichtemodulation in NbSe$_2$ für das optimale Herstellen einer topologischen Supraleitung berücksichtigt werden müssen.

Die Signale, hervorgerufen durch die Majorana-Quasiteilchen an den Enden einer topologischen, supraleitenden Phase, sind manchmal vertauschbar mit denen anderer (konventioneller) Zustände. Diese Zustände können nahezu verschwindende Energien haben und daher mit den gewünschten Null-Energie-Majorana-Quasiteilchen verwechselt werden. In der vorliegenden Arbeit, entwickeln wir eine Theorie über photonenunterstütze Andreev Reflexionen, die von Subgap-Zuständen resonant verstärkt werden. Unsere Theorie stimmt hervorragend mit einem kürzlich durchgeführten Experiment überein, welches Abweichungen von der Tien-Gordon Theorie aufweist. Unsere Theorie ist für sich genommen von Bedeutung, bietet aber auch zudem eine Technik zur Messung von Energien nahe Null der Subgap-Zustände. Tatsächlich, führen unabhängige Schwellwertbedingungen für Elektronen- und Lochtunnelprozesse zu höheren Seitenband Multiplizitäten im Fall von kleinen aber nicht verschwindenden Energiewerten der Subgap-Zustände. Experimente mit einstellbaren Photonenenergien können davon profitieren und damit die Energie des Subgap-Zustands messen.

Contents

1 | INTRODUCTION

Since the first application of topology-related concepts in condensed matter physics in the 1970s, the field of topological states of matter has developed greatly. Numerous theoretical efforts have defined and predicted a plethora of topological phases in a wide variety of systems. At the same time experimental advances in fields like heterostructure growth, nanowire growth or atomic scale manipulation, have confirmed some of these predictions and opened the door for possible applications of the topological phases, bringing forth the field of topological state engineering.

Topological state engineering comprises two different lines of work. The first of them consists on the use of topological states of matter as building blocks for the engineering of quantum systems or devices. This objective has motivated a large amount of research in the past decade. The paradigmatic goal of these efforts is the realization of a quantum computer using Majorana quasiparticles. Strongly motivated by the first, the second line of work consists on how to engineer materials or heterostructures to stably realize topological phases of matter. A prominent example is the recipe for topological superconductivity through the combination of Zeeman splitting, spin-orbit coupling and conventional superconductivity.

In this thesis we present our scientific contributions to topological state engineering. Closely related to recent experiments, our contributions fall within the first or the second line of work. Topological boundary states are associated and confined in space to the domain walls between topologically distinct regions. Their robust character is the reason they are proposed as ideal candidates for the construction of devices or interesting physical systems. Recently, the experimental realization of a topological phase out of topological domain-wall states was reported for the first time. In this thesis, we introduce a pedagogical toy model that reproduces the basic physics of these experiments and provides a playground to understand the interplay between the engineered topological phase and the underlying topological states that compose it.

The prospect of achieving non-abelian quantum computation using Majorana quasiparticles has resparked interest in Yu-Shiba-Rusinov (YSR) states. Indeed, it was predicted that magnetic adatom chains could realize topological superconductivity and host Majorana quasiparticles at their ends. Experiments have since reported promising, though not always unequivocal signatures. Our contributions in this context are two-fold. Two- and quasi-two-dimensional materials such as $NbSe_2$ have been proposed as superconducting substrates to enhance the coupling between the YSR states. Unfortunately, low-dimensional materials often develop charge-density modulations that can affect the YSR state and thus have an impact on the engineering of the magnetic adatom chain. In this thesis we discuss the effects of the charge-density wave in $NbSe_2$ on the energies and wave functions of the YSR states.

Our second contribution is the development of a full theory for photon-assisted Andreev reflections resonantly enhanced by subgap states. Crucially, superconductors can support individual states with energies within their superconducting gap such as Majorana, YSR or Andreev bound states. Tunneling from a lead into the superconductor can be resonantly enhanced by the subgap state and have a single-particle or two-particle (Andreev) character. Our theory is interesting beyond the field of topological state engineering as it is in excellent agreement with a recent experiment which notably deviates from the conventional Tien-Gordon theory, an approach that has been widely successful in explaining photon-assisted tunneling processes. As an interesting by-product of our theory, we propose a photon-based technique to measure small but non-zero subgap state energies. This technique can be instrumental to distinguish conventional near-zero-energy states from zero-energy Majorana quasiparticles.

This doctoral thesis is organized as follows. Chapter 2 serves as an introduction to basic concepts of topological states of matter, including the bulk-boundary correspondence and Majorana quasiparticles. It also includes the road map to topological superconductivity that motivates part of our work. Chapter 3 introduces the Yu-Shiba-Rusinov states, central to Chapters 5, 6, and 7. We present a derivation of these subgap states and their conductance signatures in STM experiments with superconducting tips. In Chapter 4 we propose a theoretical toy model that captures the essential physics of two recent experiments on graphene nanoribbons. We explore the phase space of our model, which constitutes an example of the engineering of systems of interest using topological states of matter as building blocks. Chapter 5 presents our research on the effects of a charge density modulation in the substrate on the energy and wave function of a YSR state. In this collaboration with an experimental group of the Freie Universität Berlin, we unveil the importance of these effects in the engineering of topological superconductivity with magnetic adatom chains in charge-density modulated superconductors such as $NbSe_2$. In Chapter 6 we present an experiment that tests the applicability of the Tien-Gordon theory for photon-assisted tunneling in superconductor-superconductor junctions. The experiment shows how this theory, while successful for bare superconducting junctions, breaks down for resonant-Andreev reflection via YSR states at high junction conductances. Motivated by this experiment, we develop a theory of photon-assisted Andreev reflections resonantly enhanced by subgap states in Chapter 7. We focus on YSR resonances and obtain a full picture of the photon-assisted processes in excellent agreement with the experiment. We extend our results to Majorana quasiparticles and we argue that our findings can be instrumental in distinguishing conventional subgap states from Majorana quasiparticles. Finally, a summary of the results is provided in Chapter 8.

2 | TOPOLOGICAL STATES OF MATTER

2.1 INTRODUCTION

The field of topology in condensed matter systems has become one of the central pillars of research in condensed matter physics in the last decades. In this Chapter, we aim to illustrate some basic concepts of topological matter that play a role in this thesis and are important to understand the potential of topological states of matter as building blocks for the engineering of quantum systems.

Before the discovery of topological phases of matter it was widely believed that Landau's theory of symmetry breaking sufficed to describe all possible phases of matter and their phase transitions. In this very general theory, the value of a local order parameter distinguishes between two phases of matter. For example, in ferromagnetic materials, the value of the magnetization distinguishes between a symmetric state (zero magnetization) and a symmetry-broken state (finite magnetization in one direction). In the 1970s the existence of distinct phases of matter which cannot be distinguished by a local order parameter was realized [Ber70; Weg71; KT73; Tho+82; Wen95]. These phases became known as topological phases and are characterized by global (i.e. non-local) properties. The global character of topological order is key to understanding its properties. Very generally, a quantity associated with a topological phase is robust against local perturbations, that is, against perturbations that are not able to change the global property defining the phase. This robustness against perturbations makes topological states of matter promising building blocks for the engineering of quantum systems, among which quantum computation has a prominent place [Nay+08; Ali12].

The first electronic topological phase observed experimentally was the Integer Quantum Hall Effect (IQHE) by Klitzing et. al. [KDP80]. In their experiment, a two-dimensional electron gas under high magnetic fields showed a quantized Hall conductivity. This quantization was found to be exceedingly precise and has since been measured to 1 part in 10^9 [Kli05]. At the heart of this precise quantization lie some concepts common to most topological phases: the bulk-boundary correspondence, the exponential localization and gap closings, all closely related to one another. After its discovery, the IQHE was explained in terms of a topological invariant known as a Chern number. This number is the global property distinguishing between the topological and trivial phases of this system and is related to the Berry curvature [Ber84].

Since the discovery of the Quantum Hall Effect a wide variety of topological phases have been identified. These include interacting systems like the Fractional Quantum Hall Effect, symmetry protected phases like Topological Insulators, Higher-Order Topological Insulators or Topological Superconductivity among others. For a more complete account of the field we refer the reader to the literature [HK10; BH13; Chi+16; WZ17; Sch+18; CDS19].

2.2 BULK-BOUNDARY CORRESPONDENCE

In this Section we illustrate the bulk-boundary correspondence by a simple example. Generally, the bulk-boundary correspondence relates the presence of edge states at the boundary of a topological system to its bulk properties. Indeed, as indicated above, a topological phase is determined by a global (bulk) property that fixes a topological invariant. In band and topological insulators, topological invariants are related to gaps in the spectrum of the bulk systems. Two ground states belong to the same topological phase if they can be related by a local unitary transformation or parametrical changes that do not close the spectral gap [CGW10]. Thus, a topological invariant can not change in value as long as the gap remains opened, being insensitive (robust) to perturbations that do not close the gap. Consider now two different adjacent regions of space with different values of a topological invariant. At the boundary between these two regions there must be a closing of the gap such that the topological invariant can change. The states that close the gap are called edge states and are exponentially localized at the boundary. These states are said to be topologically protected, meaning that their presence is insensitive to topology-preserving perturbations.

In the paradigmatic example of the Quantum Hall Effect, the two-dimensional electron gas has a Chern number n related to the number of filled Landau levels. At the boundary of the system with the vacuum (with Chern number equal to zero) n edge states arise, each allowing the Chern number to change by one unit. These edge states can be pictured semiclassically as skipping orbits which can move only in one direction. Thus, these states are chiral and transport current perfectly even in the presence of impurities because backscattering is not possible. In a finite experimental sample a chiral state and the one moving in the opposite direction are on opposite sides of the sample, separated by the bulk. Their exponential localization at the sample edges ensures that a backscattering process is highly unlikely and, thus, the conductance of these edge states is quantized with high accuracy.

In the following, we introduce a two-dimensional low-energy model, which corresponds to a massive Dirac equation, where the edge states arise due to the bulk-boundary correspondence in a transparent and understandable manner. The Hamiltonian of the model is:

$$H = k_x\sigma_x + k_y\sigma_y + m\sigma_z = \mathbf{h}(\mathbf{k}) \cdot \boldsymbol{\sigma}, \tag{2.1}$$

where k_x and k_y are the momentum, m the mass term and σ_i the Pauli matrices. The spectrum is $E(\mathbf{k}) = \pm|\mathbf{h}(\mathbf{k})|$. This model is a low energy limit of the BHZ model [BHZ06], which consists of a two-dimensional square lattice with two orbitals per site. The first tight-binding model realizing a Chern insulator was proposed by Haldane featuring a honeycomb lattice [Hal88]. The Chern number is an intrinsic property of a band and is related to the Berry phase gathered by completing a loop in momentum space that encloses the Brillouin zone:

$$\nu = \frac{i}{2\pi} \oint d\mathbf{k} \cdot \langle u(\mathbf{k}) | \partial_{\mathbf{k}} u(\mathbf{k}) \rangle \,, \tag{2.2}$$

with $|u(\mathbf{k})\rangle$ the eigenstate of the band. In two dimension this can be rewritten in terms of the gauge invariant Berry curvature [Tho+82; HK10]:

$$\nu = \frac{1}{2\pi} \int_{BZ} d^2\mathbf{k}\Omega_{k_x,k_y}, \tag{2.3}$$

where the Berry curvature Ω_{k_x,k_y} for a band is defined in general by:

$$\Omega_{k_\mu,k_\nu} = 2\mathrm{Im} \left\langle \frac{\partial u(\mathbf{k})}{\partial k_\mu} \middle| \frac{\partial u(\mathbf{k})}{\partial k_\nu} \right\rangle. \tag{2.4}$$

In a multiband model, the total Chern number is obtained summing the individual Chern numbers of the occupied bands. The Berry curvature for a general vector $\mathbf{h}(\mathbf{k})$ of Eq. (2.1) can be shown to be [QWZ06]:

$$\Omega_{k_\mu k_\nu} = \frac{1}{2}\hat{\mathbf{h}} \cdot (\partial_{k_\mu}\hat{\mathbf{h}} \times \partial_{k_\nu}\hat{\mathbf{h}}), \tag{2.5}$$

where $\hat{\mathbf{h}} = \mathbf{h}(\mathbf{k})/|\mathbf{h}(\mathbf{k})|$. For the specific $\mathbf{h}(\mathbf{k})$ of the Hamiltonian of Eq. (2.1) this yields:

$$\Omega_{k_x,k_y} = \frac{1}{2}\frac{m}{(k_x^2 + k_y^2 + m^2)^{3/2}}, \tag{2.6}$$

which yields a Chern number

$$\nu = \frac{\mathrm{sign}(m)}{2}. \tag{2.7}$$

Here some remarks are necessary. First, the rigorous mathematical definition of a Chern number implies that it is an integer [Che45; Nak03]. Nevertheless, in Eq. (2.7) we obtained a half-integer. The reason for this is that our model is not regularized, i.e., its bands extend to infinity with the momentum. This effectively "pushes" the other half of the Chern number to infinity. Also note that in the integral of Eq. (2.3) the Brillouin Zone is taken to be all of k-space. These are all consequences of working with the low-energy model. The regularized, tight-binding BHZ model has a properly defined Brillouin Zone and the Chern number always attains integer values.

The important fact we want to focus on is that the Chern number changes by a unit between two regions with opposite sign of the mass, a fact that is well captured by the low-energy model of Eq. (2.7). For the mass to change sign it has to go through zero, effectively closing the gap in a region of space. The bulk-boundary correspondence predicts the existence of a gapless mode localized at the boundary where the mass sign, i.e., the Chern number, changes. To illustrate this we consider the same low energy model for a spatially varying mass $m(x)$. Specifically, we choose the mass to change sign at $x = 0$ so that close to the origin it can be approximated by $m(x) \approx \lambda_0 x$:

$$H_0(x) \approx k_x\sigma_x + k_y\sigma_y + \lambda_0 x\sigma_z. \tag{2.8}$$

In the following, we show how this Hamiltonian leads to a topological boundary state localized at $x = 0$. The same type of behavior will play an important role in Chapter 4. The presence of a spatially varying mass implies that k_x is no longer a good quantum number. Inversion symmetry leads to a symmetric spectrum around zero energy allowing one to diagonalize the Hamiltonian by squaring it:

$$H_0(x)^2 = k_x^2 + \lambda_0^2 x^2 + k_y^2 - \lambda_0\sigma_y. \tag{2.9}$$

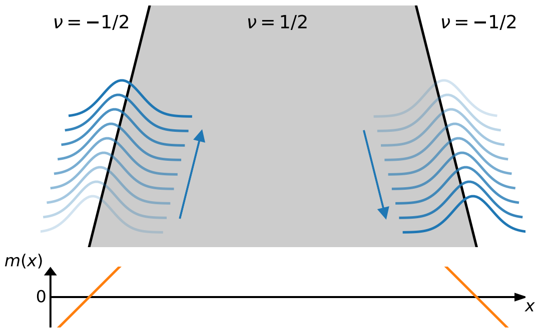

FIGURE 2.1: Schematic representation of the bulk-boundary correspondence for a system defined by the Hamiltonian of Eq. (2.8) where the mass changes sign twice, defining three regions whose Chern number vary accross a boundary. The slope of the sign change sets the chirality of the edge states arising at the boundary.

In orbital space, $H_0(x)^2$ is diagonalized by the eigenstates of σ_y, $|\pm\rangle_y$. As for the x direction of space, one identifies the first two terms on the r.h.s. of Eq. (2.9) as an harmonic oscillator with frequency $\omega = 2|\lambda_0|$. Thus, the eigenenergies of the Hamiltonian are given by:

$$E_n = \pm\sqrt{2|\lambda_0|(n+\frac{1}{2}) + k_y^2 \mp \lambda_0}, \quad \text{for} \quad |\pm\rangle_y\,, \tag{2.10}$$

with $n \geq 0$. Thus, the natural basis for the linearized Hamiltonian can be written as $|n,\pm\rangle_y$, with n denoting the n-th harmonic oscillator eigenstate. Consider now the case $\lambda_0 > 0$. In this case one finds the eigenstate and the eigenenergy of $H_0(x)$ for $n = 0$ to be:

$$|0,+\rangle_y \quad \rightarrow \quad E_0 = k_y. \tag{2.11}$$

That is, the lowest energy eigenstate is a chiral gapless mode with positive velocity in the y-direction. The wave function along the x-direction is the 0th harmonic oscillator wave function, i.e. a gaussian centered at $x = 0$. Moreover, this mode is topologically protected: its energy is independent of the value of the slope λ_0 and will be present in the system as long as the mass changes sign. This chiral gapless mode is the one predicted by the bulk-boundary correspondence for this specific model. The closing of the gap at the boundary allows for the topological invariant to change. Imagine now that for a positive x_0 the mass changes sign again. This time the sign-change slope is $\lambda_{x_0} < 0$ and the eigenstate and eigenenergy of the gap-closing state are found to be:

$$|0,-\rangle_y \quad \rightarrow \quad E_0 = -k_y. \tag{2.12}$$

Thus, at this second boundary one finds a chiral gapless mode propagating in the opposite direction. The system described is depicted in Figure 2.1, where two changes of sign of the mass $m(x)$ define three distinct regions with different Chern numbers. At the boundaries, the two counterpropagating chiral states are depicted. These two chiral modes are localized to their boundaries with a localization length l_λ and separated from each other by x_0. As long as $l_\lambda/x_0 \ll 1$, the presence of any defects along one of the boundaries has an exponentially small probability of causing backscattering. As a consequence, the conductance of these modes is robustly quantized. This simple model illustrates the kind of physics present in the IQHE.

For completeness we write the eigenstates of $H_0(x)$ for $n > 0$ again for $\lambda_0 > 0$:

$$|\mathcal{N}\rangle = \frac{1}{\sqrt{2E_n}} \left(\sqrt{E_n + k_y}\, |n, +\rangle_y + \sqrt{E_n - k_y}\, |n{-}1, -\rangle_y \right). \tag{2.13}$$

Thus, for higher energies the eigenstates are a combination of the two σ_y eigenstates with different harmonic oscillator wave functions. These eigenstates are gapped but still localized to the boundary. The energies and eigenstates presented above correspond to the linearized-mass Hamiltonian of Eq. (2.8). In a more generic case the presence of a zero-energy state and its exponential (though perhaps not Gaussian) decay is still guaranteed.

In Chapter 4 we introduce a one-dimensional model whose properties are closely related to the ones of the Hamiltonian in Eq. (2.8). Indeed, the low-energy model presented in this Section can be straightforwardly reduced to one dimension by setting $k_y = 0$. The chiral gapless edge modes reduce to end states pinned at zero energy. The model we introduce in Chapter 4 consists of a modified version of the celebrated SSH model [SSH79], presented in the following Section. Our model has a spatially dependent gap creating boundaries where the sign of the gap changes. We show how a succession of states localized at the different boundaries can be engineered to form a topological system of their own.

The topological protection of the edge states make them attractive for potential applications as well as for being used as building blocks of more complex nano-systems. Their exponential localization grants them protection against local perturbations as could be caused by thermally excited quasiparticles. The first application a topological state of matter had was the use of the IQHE quantization to measure with high precision h/e^2, whose value became a standard of resistance calibration [PS09]. The most exciting prospect of the application of topological states of matter is the realization of fault-tolerant quantum bits for the construction of a quantum computer. The topological protection would play a crucial role in guaranteeing high-fidelity quantum bits and minimizing undesired decoherence.

2.3 SU-SCHRIEFFER-HEEGER MODEL

In the 1970s the electronic properties of organic polymers were being researched for their potential technological applications [Hee+88]. Polyacetylene is one of the simplest possible polymers, consisting of (CH) units forming a quasi-one-dimensional lattice (see Fig. 2.2a). Attending to the orbital hybridization (sp^2 forming the quasi-1D chain, and a free p_z orbital) one expects a half filled p_z band, that is, one expects metallic behavior. However, the quasi-one-dimensional polymer spontaneously dimerizes leading to a gapped band structure at the Fermi energy. This is due to the so-called Peierls instability [Pei96], caused by the electron-phonon coupling in one dimension. Su, Schrieffer, and Heeger proposed a toy model of such a dimerized system, known today as Su-Schrieffer-Heeger (SSH) model [SSH79].

The SSH model has since been extensively studied for its (at the time not fully recognized) topological properties. Indeed, this simple toy model exhibits a gapped topological phase and charge fractionalization. In this Section we introduce the SSH model, which was the base of our work [AGO20] presented in Chapter 4. The SSH model consists of a tight-binding chain where the hopping alternates between strong and weak hopping. This is depicted in the lower part of Fig. 2.2a with two lines and one lines indicating the strong and weak hopping respectively. The Hamiltonian of the model can be written as:

$$\mathcal{H} = \sum_j \left[t + (-1)^j \Delta/2\right] c_j^\dagger c_{j+1} + \text{h.c.}, \tag{2.14}$$

where c_j annihilates a fermion at site j of the chain, t is the average hopping between sites and Δ the parameter leading to the dimerization of the hopping to $t \pm \Delta$. Transforming to Fourier space one finds the Bloch Hamiltonian:

$$H_k = \begin{pmatrix} 0 & t_+ + t_- e^{-2ik} \\ t_+ + t_- e^{2ik} & 0 \end{pmatrix} = \mathbf{h}(k) \cdot \boldsymbol{\sigma}. \tag{2.15}$$

For this model $\mathbf{h}(k) = (t_+ + t_- \cos 2k, t_- \sin 2k, 0)$, and the Brillouin zone is defined by $k \in [-\frac{\pi}{2}, \frac{\pi}{2}]$. The two band Hamiltonian has energies:

$$E_k = \pm\sqrt{(t^2 - \Delta^2)\cos^2 k + \Delta^2}. \tag{2.16}$$

Thus, the dimerization parameter Δ opens a gap at the edges of the Brillouin zone. Close to the edges, H_k can be expanded into a Dirac Hamiltonian of the form of H_0 of Eq. (2.1). The trivial and topological phases differ again by the sign of the gap. It is easy to check that for $\Delta = 0$ one recovers the band structure of a simple tight-binding chain albeit with an artificially doubled unit cell. The eigenstates of the positive and negative energy bands are:

$$|u_\pm(k)\rangle = \frac{1}{\sqrt{2}} \begin{pmatrix} 1 \\ \pm e^{i\phi(k)} \end{pmatrix}, \quad \text{with} \quad \tan\phi(k) = \frac{h_y(k)}{h_x(k)} = \frac{t_- \sin 2k}{t_+ + t_- \cos 2k}. \tag{2.17}$$

The topological properties of the SSH model are characterized by its symmetries. Not allowing for other terms, the Hamiltonian of Eq. (2.14) presents time-reversal, particle-hole and chiral symmetry, placing the model in the BDI symmetry class, which is characterized by a $\mathbb{Z}$ topological index in one dimension [Chi+16]. The presence of the chiral antisymmetry allows for $\mathbb{Z}$ to be defined as a winding number. Furthermore, the SSH model presents inversion symmetry about the center of the unit cell or about the middle point between unit cells. Due to the inversion symmetry, the so-called Zak phase can only take the values 0 or π, serving also to characterize the topological phases of the SSH model. The winding number and the Zak phase are closely related in the SSH model and can be used interchangeably to define its topological and trivial phase. For more complex models like the one introduced in Chapter 4, there is no such one-to-one correspondence between the two quantities. In the following, we begin the discussion with the introduction of the Zak phase.

As in the previous Section, one can calculate the Berry phase gathered upon completing a loop in momentum space. In one-dimensional band systems this has become known as the Zak phase, defined for a band j by [Zak89; RBB17; CDS19]:

$$\gamma_j = i \int_{BZ} dk \, \langle u_j(k) | \partial_k u_j(k) \rangle \, . \tag{2.18}$$

Given the gauge freedom of the overall phases of the eigenstates, the Zak phase is only defined $\mod 2\pi$. With the eigenstates of Eq. (2.17) the Zak phase of the

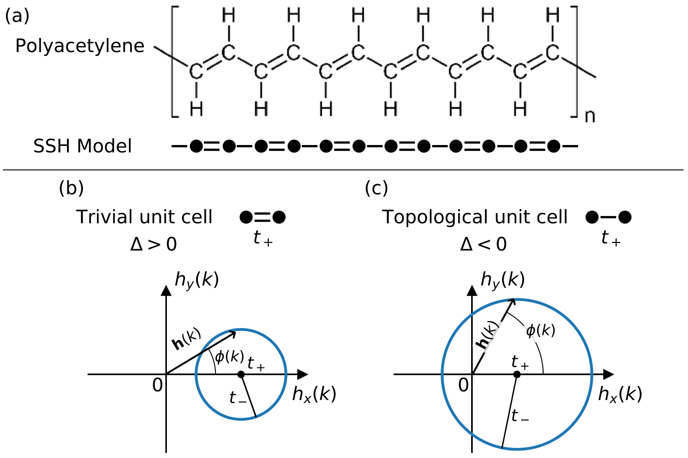

FIGURE 2.2: (a) Polyacetylene structural diagram (up, taken from commons.wikimedia.org) and SSH model simplified version of it (down). (b) and (c) mapping of the Brillouin zone to $|\mathbf{h}(\mathbf{k})|$ in the trivial (b) and in the topological phase (c).

negative energy band is:

$$\gamma_- = \frac{1}{2}\int_{-\pi/2}^{\pi/2} dk\phi'(k) \mod 2\pi. \tag{2.19}$$

This integral measures the change in the phase $\phi(k)$ as k completes a loop in the Brillouin zone. Thus, the integral can be zero ($\phi(k)$ changes but it retraces its steps back to zero) or a multiple of 2π ($\phi(k)$ winds an integer number of times). One can thus define the integer γ_-/π as the topological invariant of the SSH model. As advanced above, the winding number $\mathbb{Z}$ is closely related to the Zak phase in this model. It can be defined as the number of times the trajectory of the vector $\mathbf{h}(k)$ winds around zero in a mapping from the Brillouin zone. The mapping to $\mathbf{h}(k)/|\mathbf{h}(k)|$ is also commonly used. The mapping to the vector $\mathbf{h}(k)$ leads to a circle centered at $(t_+, 0)$ with radius t_-. The two possible cases are depicted in Fig. 2.2(b) and (c). Panel (b) corresponds to the topologically trivial case. The dimerization parameter $\Delta > 0$ causes the intracell bond t_+ to be of the strong kind. As $t_- < t_+$ the circumference does not enclose zero meaning $\mathbb{Z} = 0$. Equivalently, the angle $\phi(k)$ remains smaller than $\pi/2$ retracing its change to its initial value and leading to a zero Zak phase. Panel (c), with opposite sign of Δ, corresponds to the topological phase. With $\Delta < 0$, the roles of t_+ and t_- are interchanged, i.e. $t_+ < t_-$). In this case the trajectory of $\mathbf{h}(k)$ winds once around zero so that $\mathbb{Z} = 1$. Equivalently, the angle $\phi(k)$ continuously grows from 0 to 2π, yielding a π Zak phase. In more complex models there is not such one-to-one correspondence between the winding number and the Zak phase. At best, for inversion symmetric models, the Zak phase indicates the parity of the integer topological index $\mathbb{Z}$.

As shown above, the sign of the gap Δ distinguishes between the trivial and the topological phase. A finite chain built with topological unit cells (i.e. weak intracell hopping) exhibits localized states at its ends. The limit $\Delta = -t$ is particularly transparent as the intracell hopping becomes zero leaving two uncoupled sites separated by pairs of coupled sites. In a half-filled chain, an exponentially weak hybridization leads to an occupied electronic state with equal weight at both ends of the chains. Thus, a fractional charge of $e/2$ is associated with each boundary [Hee+88]. The charge fractionalization in the SSH model constitutes the tight-binding version of the previously discovered fermion number fractionalization in quantum field theory [JR76]. It is also possible to derive this fractionally-charged domain wall from a massive Dirac Hamiltonian for which the gap in a region of space is adiabatically taken to its opposite-sign value. Goldstone and Wilczek [GW81] found that this transports half an electronic charge leaving behind a domain wall with charge $e/2$. In the last decades, cold atom experiments have been able to reproduce the SSH lattice [SS+06; F+̈07], reporting the observation of its Zak phase and its topological end states [Ata+13; MAG16].

In Chapter 4 we introduce a modified SSH model in which we define a spatially varying gap Δ. We engineer this spatial variation such that the bound states arising at the domain walls between topological and trivial regions constitute an SSH system on their own.

2.4 TOPOLOGICAL SUPERCONDUCTIVITY

In this Section we explain the physics behind the emergence of Majorana quasiparticles in condensed matter systems. In the past two decades, the condensed matter community has produced a lot of research in Majorana quasiparticles, both theoretical and experimental [Lut+18]. Chapters 5, 6, and 7 of this thesis present basic research motivated by this strong interest. The reason driving this interest is the potential application of Majorana quasiparticles for the engineering of a fault-tolerant quantum computer. The suitability of Majoranas for this task originates from two of their properties:

- First, as edge states of topological systems they enjoy topological protection. We will not enter into the details on how Majorana quasiparticles form a quantum bit (qubit). Suffice it to say, a qubit is defined by the same-fermion-parity subspace spanned by four Majoranas [Bra06; Aas+16]. In a quantum computer the different qubits must be able to entangle with each other and maintain quantum coherence for times longer than a calculation would take. The topological protection makes Majoranas less susceptible to quasiparticle poisoning and decoherence.

- Second, Majorana quasiparticles exhibit non-abelian statistics [Iva01]. As opposed to bosons or fermions, where the order of successive exchanges of particles has no influence on the resulting state (i.e. they have abelian statistics), a successive exchange of Majoranas is affected by the particular order of the exchanges (frequently referred to as braiding). This allows one to implement logic gates between qubits in a topologically protected manner [Nay+08]. Although this is surely advantageous, it must be noted that additional not-topologically-protected gates are needed to achieve a universal set of quantum gates, necessary for the realization of a quantum computer.

We begin this Section by introducing the basics of the Majorana physics. We introduce the Kitaev chain and its similarities and differences with the SSH model. Finally, we explain the most promising proposal for the engineering of Majoranas in condensed matter systems.

2.4.1 MAJORANA BASICS

In this Section we introduce the basic theoretical concepts to understand the emergence of Majorana quasiparticles. The defining property of Majorana quasiparticles is that they are their own antiparticles or, in other words, their creation operator is equal to their annihilation operator:

$$\gamma = \gamma^{\dagger}. \tag{2.20}$$

Indeed, Majoranas owe their name to Ettore Majorana, who found a charge-conjugation invariant solution to the high-energy-physics Dirac equation [Maj37]. Contrary to these predicted free-standing particles, condensed matter Majoranas do not have dynamics of their own and are associated with the domain walls of topological systems. Furthermore, the building blocks at our disposal in condensed matter systems are electrons, that is, fermions so that condensed matter Majoranas are of the form

$$\gamma \sim c + c^{\dagger}, \tag{2.21}$$

where c is a fermionic operator. It turns out that the type of systems where such emergent quasiparticles can arise are spinless p-wave superconductors, also known as topological superconductors. Below we explain how to realize such "spinless" systems out of the spinful electrons present in materials.

In the following we introduce the Kitaev Chain [Kit01], a minimal tight-binding model of a spinless p-wave superconductor that shares some similarities with the SSH model. Its Hamiltonian is given by:

$$\mathcal{H} = \sum_j \left[-\mu c_j^{\dagger} c_j - t(c_{j+1}^{\dagger} c_j + c_j^{\dagger} c_{j+1}) + \Delta(c_{j+1} c_j + c_j^{\dagger} c_{j+1}^{\dagger}) \right]. \tag{2.22}$$

Thus, the Kitaev chain consists of a simple tight-binding chain with superconducting correlations among neighboring sites. Transforming to Fourier space and writing the Bloch Hamiltonian in Nambu space $\psi_k = (c_k, c_{-k}^{\dagger})^T$ one finds:

$$H_k = \begin{pmatrix} \xi_k & 2i\Delta \sin k \\ -2i\Delta \sin k & -\xi_k \end{pmatrix} = \mathbf{h}(k) \cdot \boldsymbol{\sigma}, \tag{2.23}$$

with $k \geq 0$. For this model $\mathbf{h}(k) = (0, -2\Delta \sin k, \xi_k)$, with $\xi_k = -2t \cos k - \mu$. At this level one can already draw similarities with the SSH model. In momentum space, both the Kitaev chain and the SSH model exhibit chirally-symmetric Hamiltonians. One could even perform a rotation in Pauli matrix space for both models to involve the same Pauli matrices. Thus, in both models the energies come in pairs of opposite energies. Also, the chiral symmetry allows one to define a winding number in the Kitaev chain in the same manner as defined above for the SSH model. This leads to a phase diagram for the Kitaev chain, for which one also finds different winding numbers upon sign changes of the gap Δ. Although the two models present these structural similarities the character of their solutions is very different. At the root of this is the fact that, while for the SSH chain the space of the two-by-two Hamiltonian is spanned by the two sites of the unit cell (i.e. two fermionic sites), in the case of the Kitaev chain the Hamiltonian is written in Nambu space (i.e. particle-hole space). This difference becomes more apparent when considering their respective topological end states. To this end, it is convenient to write the Kitaev chain in terms of Majorana operators:

$$c_j = \frac{1}{2}(\gamma_{A,j} + i\gamma_{B,j}). \tag{2.24}$$

Writing the inverse relations one can check that

$$\{\gamma_\alpha, \gamma_\beta\} = 2\delta_{\alpha,\beta}, \tag{2.25}$$

where α and β can represent more than one subindex. In terms of these Majorana operators the Hamiltonian of Eq. (2.22) is given by:

$$\mathcal{H} = \sum_j \Big[-(t+\Delta)\gamma_{A,j}\gamma_{B,j+1} + (t-\Delta)\gamma_{B,j}\gamma_{A,j+1} - \frac{\mu}{2}(1 + i\gamma_{A,j}\gamma_{B,j})\Big]. \tag{2.26}$$

Thus, one obtains two dimerized Majorana-operator chains uncoupled from each other in the case $\mu = 0$. Furthermore, each of these chains has a weak bond at opposing ends of a finite Kitaev chain. Recall that for the SSH chain, the particular case $\Delta = -t$ yielded two uncoupled sites one at each end of a finite chain. This means that there are two fermionic states with exactly zero energy, leading to a four-fold degenerate many-body ground state. An equivalent special case for the Kitaev chain is found at $\Delta = -t$, $\mu = 0$:

$$\mathcal{H}_{\mathrm{s}} = 2t \sum_j \gamma_{B,j}\gamma_{A,j+1}. \tag{2.27}$$

It is easy to see that, in a finite N-site chain, one Majorana operator at each end is uncoupled, yielding two zero-energy Majorana modes. These two Majoranas, $\gamma_{A,1}$ and $\gamma_{B,N}$, define a single highly-non-local fermionic operator

$$d_{\mathrm{M}} = \frac{1}{2}(\gamma_{A,1} + i\gamma_{B,N}). \tag{2.28}$$

As a consequence, the many-body degenerate ground state of a Kitaev chain with two isolated Majoranas is two-fold degenerate. From this discussion it is easy to understand why Majoranas are often referred to as "half fermions". These specific cases for both the SSH and Kitaev chain are particularly transparent but we must remark that the character of their solutions extends to all points of the topological regions of their parameter spaces. As a final remark, we want to point out that the difference in the character of the topological end states of the SSH and the Kitaev chain are a hallmark of their different respective short- and long-range entanglement underlying their topological phases [RG00; CGW10].

In conclusion, the Kitaev chain is a very didactic toy model, wonderful to get acquainted with topological superconductivity and Majorana quasiparticles. The lack of readily-available spinless fermions in physical condensed matter systems makes it an oversimplification of what one can achieve in real materials. The following Section presents a general recipe to engineer topological superconductivity in real condensed matter systems.

2.4.2 ENGINEERING A TOPOLOGICAL SUPERCONDUCTOR

At the time of the writing of this thesis, a notable number of theoretical proposals for systems hosting Majorana quasiparticles have been put forward. Examples of these are the fractional QHE at $5/2$ filling [MR91], intrinsic $p + ip$ superconductivity as predicted for some materials [Kal12] or topological insulator edges proximitized by a superconductor [FK08; FK09]. In this Section, we present the at-the-time most promising proposal: one-dimensional systems combining Zeeman splitting, spin-orbit coupling and s-wave superconductivity [LSS10; ORO10; NP+13]. For a more complete account of the different proposals and experimental advances we refer the reader to the literature [Ali12; Bee13; EF15; SF16; Lut+18].

We begin the Section with a basic account on how one-dimensional electronic systems can be driven into a topological superconducting phase. As mentioned above, spinless fermions are not readily available in condensed matter and we are forced to make use of spinful electrons and holes. The goal is obtaining an effective BdG-Hamiltonian of the type:

$$H_p = \xi_k \tau_z + \Delta_{\text{eff}} k \tau_x, \tag{2.29}$$

which is a low energy limit of the Kitaev Bloch Hamiltonian of Eq. (2.23), bar a rotation of Pauli matrices. The strategy to achieve this is to combine three easily accessible physical ingredients: Zeeman splitting, spin-orbit coupling (SOC), and s-wave superconductivity. Following [LSS10; ORO10], this can be achieved in one-dimensional semiconductor nanowires in the presence of magnetic fields proximitized by a conventional superconductor. Such a wire would be described by the following BdG Hamiltonian:

$$H_{\text{wire}} = (\xi_k + \alpha k \sigma_x)\tau_z - B\sigma_z + \Delta \tau_x, \tag{2.30}$$

where the Nambu basis $\Psi = (\psi_{k_\uparrow}, \psi_{k_\downarrow}, \psi^\dagger_{-k_\downarrow}, -\psi^\dagger_{-k_\uparrow})^T$ is used, with ψ_{k_σ} the electron annihilation operator of momentum k and spin σ. Here αk is the spin-orbit coupling, B a magnetic field, and Δ the s-wave pairing. To understand how the three ingredients lead to topological superconductivity we follow [OPP17] to show that this Hamiltonian can be reduced to the one in Eq. (2.29) in the correct parameter regime. We begin by considering a one-dimensional band in the presence of a magnetic field and then include SOC and superconductivity perturbatively:

1. Magnetic field: in condensed matter, a "spinless-fermion system" is best approximated by a system with electrons of only one spin orientation. If the magnetic field $B > |\mu|$ only the spin-up band has occupied states. In this situation one can project out the spin-down band and work in the basis:
$$\begin{aligned} |e_\uparrow\rangle &= (1,0,0,0)^T, \\ |h_\uparrow\rangle &= (0,0,0,1)^T. \end{aligned} \tag{2.31}$$

2. Spin-orbit coupling: s-wave superconducting pairing can not induce superconducting correlations between spin-up electrons and holes, $\langle e_\uparrow| \Delta\tau_x |h_\uparrow\rangle = 0$. The crucial role of SOC consists of allowing a degree of mixing between the two spin flavours. Including the SOC term perturbatively, the basis of Eqs. (2.31) changes to:
$$\begin{aligned} |e_\uparrow\rangle &= (1,-\alpha k/2B,0,0)^T, \\ |h_\uparrow\rangle &= (0,0,-\alpha k/2B,1)^T, \end{aligned} \tag{2.32}$$
where the spin is no longer fully polarized.

3. s-wave pairing: introducing the superconducting term again perturbatively one finds:
$$\langle e_\uparrow|\Delta\tau_x|h_\uparrow\rangle = \langle h_\uparrow|\Delta\tau_x|e_\uparrow\rangle = -\alpha k\Delta/2B, \tag{2.33}$$

and zero diagonal terms. The projected Hamiltonian in the $\{|e_\uparrow\rangle, |h_\uparrow\rangle\}$ basis results:

$$H'_p = (\xi_k - B)\tau_z - \frac{\alpha\Delta}{B} k\tau_x, \tag{2.34}$$

that is, an effective p-wave superconductor of the form of Eq. (2.29) where one can identify $\Delta_{\text{eff}} = -\alpha\Delta/B$.

The above derivation makes the interplay and role of each of the three ingredients B, αk and Δ transparent. Nevertheless, it is not hard to diagonalize the full H_{wire} Hamiltonian, for which one finds the energies:

$$E_k = \pm\sqrt{\xi_k + (\alpha k)^2 + B^2 + \Delta^2 \pm \sqrt{\xi_k^2(\alpha k)^2 + B^2(\xi_k^2 + \Delta^2)}}. \tag{2.35}$$

At $k = 0$ the spectrum is generally gapped:

$$E_{k=0} = \pm|B - \sqrt{\mu^2 + \Delta^2}|. \tag{2.36}$$

The gap closing given by the relation $B = \sqrt{\mu^2 + \Delta^2}$ defines the topological phase transition of the model, with $B > \sqrt{\mu^2 + \Delta^2}$ corresponding to the topological phase.

Using this recipe a long list of experiments have reported signatures consistent with the presence of Majorana quasiparticles. Most of these use semiconductor nanowires with SOC proximitized by a superconductor in the presence of a magnetic field (or an insulating ferromagnet). The first such experiments appeared in 2012 [Mou+12; RLF12; Den+12; Das+12] reporting either robust zero bias peaks or signatures related to a 4π-periodic Josephson junction, which the presence of Majoranas is predicted to lead to [Lut+18]. One relies on these signatures given the difficulty of experimentally probing the non-abelian statistics of the Majoranas, which would be an unequivocal evidence of their presence. Concerns were raised about the compatibility of these signatures with other non-topological effects such as the Kondo effect or disorder among others [Lee+12; Liu+12; Chu+13; KMB12; Chu+13]. Progress on the growth techniques of semiconductor nanowires partially covered with a superconductor have led to cleaner surfaces and more transparent interfaces providing more reliable data on the presence of Majorana quasiparticles in these systems [Den+16; Suo+17; Che+17; Zha+17a; G+̈18; Vai+20].

There is another kind of systems that also follows the above recipe for topological superconductivity. They consist of chains of magnetic adatoms on top of a superconducting substrate. Chapters 5, 6, and 7 present research done during this doctoral thesis in the context of this kind of systems. The magnetic adatoms lead to spin-polarized in-gap states known as Yu-Shiba-Rusinov states. Due to their importance for this thesis we dedicate Chapter 3 to introducing them.

3 | YU-SHIBA-RUSINOV STATES

3.1 INTRODUCTION

Chapters 5 and 7 of this thesis contain theoretical framework and calculations developed to explain the results of two experiments performed by Katharina Franke's group. The two experiments investigate different aspects of Yu-Shiba-Rusinov (YSR) states. Theoretically predicted in the second half of the 1960s [Yu65; Shi68; Rus69], these are bound states localized around magnetic impurities placed on top or within a superconductor. The pioneering experimental study of a YSR using a STM of Yazdani et. al. [Yaz+97] sparked the interest into this type of bound states and the local electronic properties of superconductors they open a window into.

More recently, chains of magnetic adatoms have been proposed as a platform for topological superconductivity [NP+13; PGO13]. The research presented in Chapters 5, 6, and 7 provides important results for the engineering of topological superconductivity with NbSe_2 substrates and a radiation based technique to improve the energy measurement of the sought-for Majorana quasiparticles. This Chapter introduces the basics of YSR states and their relevant aspects for the subsequent Chapters.

3.2 YSR STATE ENERGY AND WAVE FUNCTION

The origin of the magnetic moment and the resulting exchange coupling between an impurity and the electrons in a metal can be understood starting with an Anderson model and its mapping to a Kondo Hamiltonian in the absence of valence fluctuations [Hew93]. However, YSR states are typically well described within a model which treats the impurity spin in the Kondo model as classical [Yu65; Shi68; Rus69]. In the following, we derive the basic properties of a YSR state, namely its energy and the long range behaviour of its wave function. This derivation follows the lines of [PGO13], further extended in [Mén+15] to include the wave function behavior for 2D superconductors.

A magnetic adatom on top of a 2D or 3D superconductor can be described by the following Bogoliubov-de Gennes (BdG) Hamiltonian:

$$H = \xi_{\hat{\mathbf{p}}}\tau_z + \Delta\tau_x + (K\tau_z - J\mathbf{S}\cdot\boldsymbol{\sigma})\delta(\hat{\mathbf{r}}), \tag{3.1}$$

where the first two terms correspond to a translationally invariant superconductor, with $\xi_{\hat{\mathbf{p}}} = \hat{\mathbf{p}}^2/2m - \mu$ the band dispersion measured from the chemical potential μ, Δ the superconducting gap and the Pauli matrices $\boldsymbol{\tau}$ acting in particle-hole space. The terms proportional to the delta function correspond to an impurity placed at the origin, with potential scattering K and exchange coupling J between the classical impurity spin $\mathbf{S}$ and the electrons' spin $\boldsymbol{\sigma}$. This Hamiltonian is written in the Nambu basis $\Psi = (\psi_\uparrow, \psi_\downarrow, \psi_\downarrow^\dagger, -\psi_\uparrow^\dagger)^T$, with $\psi_\sigma = \psi_\sigma(\mathbf{r})$ the electronic field operator of spin σ.

Choosing $\mathbf{S}$ parallel to the z-axis splits the 4×4 Hamiltonian (3.1) into two 2×2 independent blocks related by particle-hole symmetry $P = i\tau_y\mathcal{K}$, with $\mathcal{K}$ denoting complex conjugation. We focus on the block corresponding to $\Psi_{e\uparrow} = (\psi_\uparrow, 0, \psi_\downarrow^\dagger, 0)^T$, for which we solve the eigenvalue equation:

$$[\xi_{\hat{\mathbf{p}}}\tau_z + \Delta\tau_x + (K\tau_z - JS)\delta(\hat{\mathbf{r}})]\,\varphi(\mathbf{r}) = E\varphi(\mathbf{r}), \tag{3.2}$$

with $\varphi(\mathbf{r}) = (u_\uparrow(\mathbf{r}), v_\downarrow(\mathbf{r}))^T$. Fourier transforming to momentum space:

$$\varphi(\mathbf{r}) = \int \frac{d\mathbf{p}}{(2\pi)^d} e^{i\mathbf{p}\cdot\mathbf{r}} \varphi_{\mathbf{p}}, \tag{3.3}$$

where $d = 2, 3$, one finds

$$[E - \xi_{\mathbf{p}}\tau_z - \Delta\tau_x]\,\varphi_{\mathbf{p}} = (K\tau_z - JS)\varphi(\mathbf{0}). \tag{3.4}$$

Solving for $\varphi_{\mathbf{p}}$ and transforming back to real space yields:

$$\varphi(\mathbf{r}) = \int \frac{d\mathbf{p}}{(2\pi)^d} \frac{e^{i\mathbf{p}\cdot\mathbf{r}}}{E^2 - \xi_{\hat{\mathbf{p}}}^2 - \Delta^2} [E + \xi_{\mathbf{p}}\tau_z + \Delta\tau_x]\,(K\tau_z - JS)\varphi(\mathbf{0}). \tag{3.5}$$

From this equation one can calculate the shape of the wave function as well as the energy of the YSR state. The details on how to perform the integral can be found in [PGO13; Mén+15; Bry+15]. The steps are: changing the momentum integral to an energy integral ($\int \frac{d\mathbf{p}}{(2\pi)^d} \to \nu_0 \int d\xi_{\mathbf{p}} d\Omega^d$), linearising $p(\xi_{\mathbf{p}})$ on the energy, performing the contour integral for the energies and, finally, the angular integral. We have introduced the normal state density of states ν_0. To find the energy of the YSR state one evaluates Eq. (3.5) at $\mathbf{r} = 0$ which, after performing the integrals, yields:

$$\left[1 + \frac{\pi\nu_0}{\sqrt{\Delta^2 - E^2}}(E + \Delta\tau_x)(K\tau_z - JS)\right]\varphi(\mathbf{0}) = 0. \tag{3.6}$$

There is a subgap solution found at the energy:

$$E_{\text{YSR}} = \text{sign}(J)\frac{\Delta(1 - \gamma^2 + \kappa^2)}{\sqrt{4\gamma^2 + (1 - \gamma^2 + \kappa^2)^2}}, \tag{3.7}$$

with $\gamma = \pi\nu_0|J|S$ and $\kappa = \pi\nu_0 K$. Due to the particle-hole symmetry, the energy of the $\Psi_{e\downarrow} = (0, \psi_\downarrow, 0, -\psi_\uparrow^\dagger)^T$ subspace has the opposite sign. Note that for vanishing exchange interaction ($J = 0 \to \gamma = 0$) there is no subgap solution.

An important property of the YSR energy E_{YSR} is that it can change sign, going through zero at the critical value $\gamma_c = \sqrt{1 + \kappa^2}$. This change of sign entails a quantum phase transition (QPT) between two distinct ground states. This was first discussed in [Sak70] and has since been experimentally studied [FSP11; Far+18]. For $\gamma_c < \sqrt{1 + \kappa^2}$ and antiferromagnetic coupling ($J < 0$) the YSR state has negative energy meaning that the state corresponding to the spin-up electron and spin-down hole subspace is occupied in the ground state. This ground state, being on the same side of the QPT as the $\gamma = 0$ state, is similar in form to the BCS ground state, consisting only of Cooper pairs, and thus has a net zero electron spin [BVZ06]. For $\gamma_c > \sqrt{1 + \kappa^2}$ this state is empty in the ground state, and the one of the spin-down electron and spin-up hole subspace is occupied, leading to a total electron spin of -1. The physical picture behind this is that when the exchange coupling of the impurity becomes strong enough to overcome the superconducting pairing potential a Cooper pair is broken and a single electron is bound to the impurity.

It is experimentally challenging to assess to which side of this quantum phase transition an YSR state is. This has been achieved exploiting the flexibility of molecules containing a magnetic atom [Far+18]. This flexibility allows for tuning of the exchange coupling between the magnetic impurity and the substrate. For example, if when increasing the coupling one observes a decrease of the YSR state energy, according to Eq. (3.7), the system is still in the weakly coupled regime. This knob is generally not available for single adatoms, for which the exchange coupling depends on the non-tunable adsorption site. In Chapter 5 we show how a similar knob may be available for materials exhibiting a charge density wave modulation that affects the local density of states in the vicinity of the adatom.

Finally, we focus on the shape of the YSR wave function. Again, integrating from Eq. (3.5) one finds the following expressions:

$$u_{3D}(r), v_{3D}(r) = \frac{1}{\sqrt{N}} \frac{\sin(k_F r + \delta^{\pm})}{k_F r} e^{-r/\xi}, \tag{3.8}$$

for the three-dimensional case, and:

$$u_{2D}(r), v_{2D}(r) = \frac{1}{\sqrt{N}} \frac{\sin(k_F r - \pi/4 + \delta^{\pm})}{\sqrt{\pi k_F r}} e^{-r/\xi}, \tag{3.9}$$

for the two-dimensional one. $u_i(r)$ and $v_i(r)$ stand for the electron and hole parts of the wave function, $\delta^{\pm} = \arctan(\kappa \pm \gamma)$, k_F is the Fermi momentum and $\xi = \hbar v_F / \sqrt{\Delta^2 - E_{\text{YSR}}^2}$ a decay length related to the coherence length of the superconductor. In both cases, the wave functions are asymptotic expressions for $k_F r \gg 1$, $k_F \gg \xi^{-1}$.

The relevant difference between the wave functions in two and three dimensions is their short-range decay. This goes like $\sim 1/\sqrt{r}$ for 2D and like $\sim 1/r$ for 3D. A proposal for the engineering of Majorana boundstates consists in the coupling of several YSR states forming a one-dimensional chain [PGO13; NP+13; Cho+11; NTN13; BS13; Kli+13; VF13; Kim+14; Bry+15; Rub+15a; NP+14]. As will be explained below, this kind of setup has the necessary ingredients for the emergence Majorana particles. Going from three to two dimensions provides an enhancement in the spatial extent of the YSR wave functions which facilitates the manipulation and coupling of different YSR states.

3.2.1 YSR GREEN'S FUNCTION

Another way of deriving the emergence of a subgap bound state is through the superconducting Green's function [Rub+15b]. This derivation is closely related to the one presented above so we do not go through it in detail. The Green's function of a superconductor with an magnetic impurity can be calculated through the Dyson equation:

$$g(\omega)^{-1} = g_0(\omega)^{-1} - (K\tau_z - JS), \tag{3.10}$$

where

$$g_0(\omega) = -\frac{\pi \nu_0}{\sqrt{\Delta^2 - \omega^2}} (\omega + \Delta \tau_x) \tag{3.11}$$

is the bare superconducting Green's function (see App. A). Inverting equation (3.10) one finds:

$$g(\omega) = \frac{\pi\nu_0(\omega + \Delta\tau_x + (\gamma + \kappa\tau_z)\sqrt{\Delta^2 - \omega^2})}{2\gamma\omega - (1 - \gamma^2 + \kappa^2)\sqrt{\Delta^2 - \omega^2}}, \tag{3.12}$$

which has a pole at the YSR state energy (3.7). Finally one can expand the Green's function in the vicinity of this energy yielding:

$$g(\omega) \approx \varphi \frac{1}{\omega - E_{\text{YSR}}} \varphi^\dagger, \tag{3.13}$$

with $\varphi = \varphi(\mathbf{0}) = (u, v)^T$, with u and v the electron and hole part of the YSR wave function evaluated at the origin:

$$u^2, v^2 = \frac{2\gamma\Delta\pi\nu_0(1 + (\gamma \pm \kappa)^2)}{[4\gamma^2 + (1 - \gamma^2 + \kappa^2)^2]^{3/2}}. \tag{3.14}$$

Equation (3.13) represents the contribution of the YSR state to the total substrate Green's function. This YSR Green's function will be used in Chapter 7 to calculate the current between a STM tip and a superconducting substrate through a YSR resonance.

3.3 YSR STATES IN STM MEASUREMENTS

Since the first observation of YSR states by STM [Yaz+97], experimental advances have greatly improved the resolution of YSR resonances, mainly due to lower temperature setups and the use of superconducting tips in STM measurements [HPF18]. In this Section, we want to give a brief account of the signatures of the YSR states which play a role in Chapter 5 and, specially, in Chapters 6 and 7. In particular, we present the results of [Rub+15b], where the interplay between single-particle and two-particle (Andreev) tunneling was studied as a function of the junction resistance.

We start the discussion by introducing the four quantities that account for the different current signatures a single YSR state can lead to. These are Γ_1, Γ_2, Γ_e and Γ_h. Γ_1 is the rate at which a quasiparticle in the YSR state can be thermally excited into the quasiparticle continuum of the substrate. Γ_2 is the rate of the opposite process, a thermally excited quasiparticle in the continuum relaxes into the YSR state. Γ_e can be understood as the tunneling rate of electrons to or from the positive-energy YSR state. Conversely Γ_h is the tunneling rate of holes to or from the negative-energy YSR state. For superconducting STM tips, these two quantities are frequency dependent:

$$\begin{aligned} \Gamma_e(\omega) &= 2\pi|u|^2|t|^2\nu(\omega), & (3.15) \\ \Gamma_h(\omega) &= 2\pi|v|^2|t|^2\nu(\omega) & (3.16) \end{aligned}$$

with t the tunneling amplitude across the junction and the BCS density of states

$$\nu(\omega) = \nu_0 \frac{|\omega|}{\sqrt{\omega^2 - \Delta^2}} \theta(|\omega| - \Delta). \tag{3.17}$$

Figure 3.1 provides a schematic representation of the single- and two-particle processes across a junction formed by two equal-gap superconductors in the presence of a YSR state. In every panel the left hand side superconductor

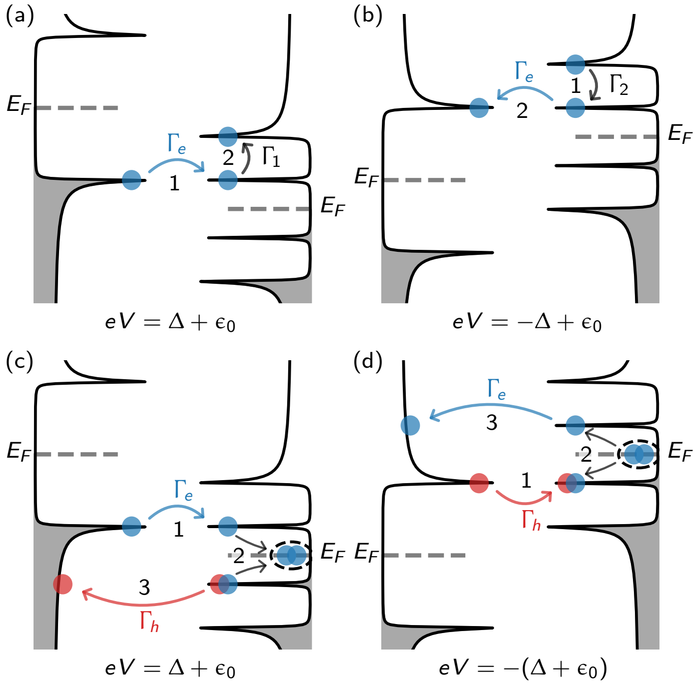

FIGURE 3.1: Single- and two-particle processes in a junction consisting of a superconducting tip (left superconductor) and a superconducting substrate (right superconductor) with a YSR state. Only processes involving the YSR state are shown. Panels (a) and (b) depict single-particle processes involving the relaxation rates Γ_1 and Γ_2 to and from the quasiparticle continuum and Γ_e. Analogous processes at opposite bias involve Γ_h. Panels (c) and (d) depict resonant Andreev reflection processes at positive and negative bias respectively.

represents the superconducting tip, which shifts by the applied bias eV indicated at the bottom of each panel relative to the right hand side superconductor, which includes the YSR resonances at the energies $\pm\epsilon_0$. The single-particle processes involving Γ_e are depicted in panels (a) and (b). Panel (a) shows the junction at a bias $eV = \Delta + \epsilon_0$. At this bias, electrons from the tip can tunnel into the positive-energy YSR state at a rate Γ_e, and are then excited into the continuum at a rate Γ_1. Note that this process was not possible at any smaller positive bias due to the lack of states within the tip superconducting gap. Also, the current due to this process is maximal at this point due to the high density of states of the BCS coherence peak. For this reason, one speaks of the bias $eV = \Delta + \epsilon_0$ as a threshold bias for the electron tunneling rate Γ_e beyond which such tunneling becomes possible. In a experiment, this onset of the current translates into a peak in the differential conductance. Such peaks can be observed in the YSR spectra displayed in Fig. 3.2, for which $\Delta = 1.35\text{meV}$ and $\epsilon_0 \approx 0.25\text{meV}$.

In a similar manner, at $eV = -\Delta + \epsilon_0$, the opposite single-particle process becomes possible. This is depicted in panel (b), where electrons from the continuum can relax into the positive-energy YSR state at a rate Γ_2 and then tunnel into the tip at a rate Γ_e. Analogous single-particle processes involving Γ_h take place at biases with opposite signs of those in panels (a) and (b), with corresponding opposite sign thresholds. The value of these thresholds plays an important role in Chapters 6 and 7 where they become important to understand the intriguing structures of the sidebands of the two-particle current in the presence of radiation. For this reason we explicitly write the threshold values:

$$\begin{aligned} eV^{\mathrm{th}}_{e\pm} &= \pm\Delta + \epsilon_0, \\ eV^{\mathrm{th}}_{h\pm} &= \pm\Delta - \epsilon_0. \end{aligned} \tag{3.18}$$

Panels (c) and (d) show Andreev reflection processes resonantly enhanced by the YSR state. In panel (c), at positive bias, an electron first tunnels from the tip into the positive-energy YSR state and then combines with another electron to form a Cooper pair leaving a hole in the negative-energy YSR state. Lastly, the hole tunnels into the tip. In panel (d), at opposite bias, charge travels in the other direction, breaking a Cooper pair in the substrate. Note that for these processes to be allowed both Γ_e and Γ_h must be above threshold. Expressions for the tunneling currents were derived in [Rub+15b]:

$$I_{\Gamma_1}(V) = \frac{e}{h}\int \mathrm{d}\omega \frac{\Gamma_1\left[\Gamma_e^{n_\mathrm{F}}(\omega_-) - \Gamma_h^{n_\mathrm{F}}(\omega_+)\right]}{(\omega-\epsilon_0)^2 + \Gamma(\omega)^2/4}, \tag{3.19}$$

$$I_{\Gamma_2}(V) = \frac{e}{h}\int \mathrm{d}\omega \frac{-\Gamma_2\left[\Gamma_e^{1-n_\mathrm{F}}(\omega_-) - \Gamma_h^{1-n_\mathrm{F}}(\omega_+)\right]}{(\omega-\epsilon_0)^2 + \Gamma(\omega)^2/4}, \tag{3.20}$$

$$I_a(V) = \frac{2e}{h}\int \mathrm{d}\omega \frac{\Gamma_h(\omega_+)\Gamma_e^{n_\mathrm{F}}(\omega_-) - \Gamma_e(\omega_-)\Gamma_h^{n_\mathrm{F}}(\omega_+)}{(\omega-\epsilon_0)^2 + \Gamma(\omega)^2/4} \tag{3.21}$$

where $\Gamma(\omega) = \Gamma_1 + \Gamma_2 + \Gamma_e(\omega_-) + \Gamma_h(\omega_+)$ and $\omega_\pm = \omega \pm eV$, and where we defined:

$$\Gamma_e^{n_\mathrm{F}}(\omega) = 2\pi t^2 |u|^2 \nu(\omega) n_\mathrm{F}(\omega), \tag{3.22}$$

$$\Gamma_e^{1-n_\mathrm{F}}(\omega) = 2\pi t^2 |u|^2 \nu(\omega)[1 - n_\mathrm{F}(\omega)], \tag{3.23}$$

for compactness. The corresponding definitions for $\Gamma_h^{n_\mathrm{F}}$ and $\Gamma_h^{1-n_\mathrm{F}}$ differ by replacing $|u|^2 \to |v|^2$. The total current is the sum of the three contributions: I_{Γ_1} and I_{Γ_2} account for the single-particle current and I_a accounts for the resonant Andreev current. The shape of the integral consists of a Lorentzian-shaped resonance centered at the YSR energy ϵ_0 with a broadening $\Gamma(\omega)$. Note that, in many cases, tunneling currents are treated perturbatively in the tunneling amplitude t, as this is normally a small parameter. As a consequence, in such treatments, the tunneling rates Γ_e and Γ_h do not appear in the broadening of resonances. The derivation of [Rub+15b], which we generalize to include exposure to radiation in Chapter 7, includes the tunneling to all orders. This is very relevant when the junction conductance is increased, i.e. the tip-to-sample distance reduced. Indeed, this was precisely the focus of their experiment, which studied how the relative contribution of the single-particle and Andreev current to the total current can be tuned by changing the junction conductance.

Figure 3.2 shows experimental data of two YSR spectra of a Mn adatom deposited on top of a Pb substrate. Though there is more than one YSR state associated with the Mn adatom, we focus on the lowest energy one, which leads to all the conductance peaks labeled in the plot. At $eV = \pm 2\Delta$ the BSC coherence peaks are visible. The blue line corresponds to large tip-to-sample distances, yielding a differential conductance orders of magnitude smaller than in the shorter tip-to-sample distance case, in orange. At large tip-to-sample distances, the single-particle current dominates over the Andreev current, the latter being of higher order in the tunneling amplitude t. In this situation, Γ_1 and Γ_2 dominate the broadening $\Gamma(\omega)$. One can identify each peak with a contribution to the single particle current as labeled in the plot, where the Fermi distributions

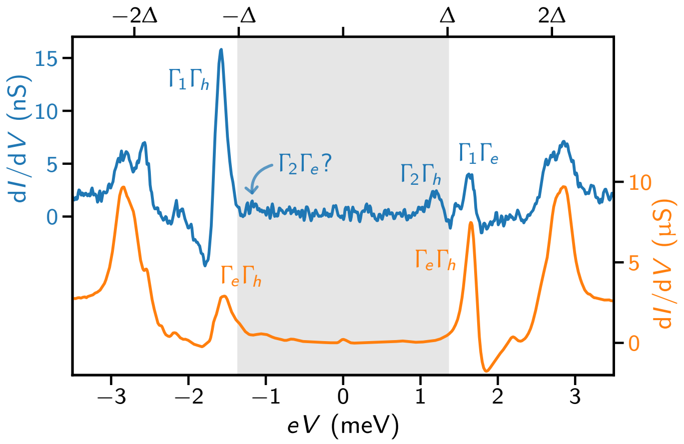

FIGURE 3.2: YSR spectra of an Mn adatom on top of superconducting Pb taken with a superconducting STM tip. At low junction conductances (blue line) the current is dominated by single-particle tunneling. The peaks of the lowest lying YSR state are identified with the corresponding rates involved. At high junction conductances (orange line) the current is dominated by resonant Andreev reflections. The tunneling rates dominate the broadening of the resonance leading to peaks of inverted height with respect to the low junction conductance case (see text).

were omitted for compactness. The peaks corresponding to I_{Γ_1} appear at the biases $eV = \pm(\Delta + \epsilon_0)$ and the ratio of their peak heights is a direct signature of the ratio of the YSR state electron and hole wave function components at the adatom position $|v/u|^2$. In this case this ratio is highly asymmetric $|v/u|^2 \approx 4$. The same ratio is expected for the conductance peaks of I_{Γ_2}.

For small tip-to-sample distances (orange line) the Andreev current dominates over the single-particle current. Note that in this case there are no distinctive features within the shaded region. This is due to the above-mentioned fact that both Γ_e and Γ_h must be above their thresholds for the Andreev current to be possible. In this case, the tunneling rates Γ_e and Γ_h dominate over the relaxation rates Γ_1 and Γ_2 in the broadening. This has an important consequence for the relative height of the peaks. Due to the asymmetry in the wave function weights $|u^2|$ and $|v^2|$, the denominator is bigger at the threshold bias of Γ_h, i.e. $eV^{\text{th}}_{h_-} = -(\Delta + \epsilon_0)$, than at the threshold bias of Γ_e, i.e. $eV^{\text{th}}_{e_+} = \Delta + \epsilon_0$. This leads to a lower broader peak at negative bias. The relation of the peak heights is found to be $|u/v|^{10/3}$ [Rub+15b].

These relations can all be derived from Eqs. (3.19)-(3.21). We dedicate the rest of this Section to derive the peak heights of the conductance due to the resonant Andreev current in the regime where it dominates over the single-particle current. We consider two possible situations of electron or hole rate dominating the broadening. These considerations play an important role in Chapter 7. We focus on biases in the vicinity of $eV \simeq eV^{\text{th}}_{e_+} = \Delta + \epsilon_0$. Near this bias the hole tunneling rate is non-singular and we neglect its weak dependence on ω:

$$\Gamma_h(\omega + eV^{\text{th}}_{e_+}) = \Gamma^{\text{th},e}_h \simeq \gamma_h \frac{\Delta + 2\epsilon_0}{\sqrt{(\Delta + \epsilon_0)4\epsilon_0}} \simeq \gamma_h \sqrt{\frac{\Delta}{4\epsilon_0}}, \tag{3.24}$$

where we have assumed that the broadening is small compared to ϵ_0 such that the current integral has weight for ω close to the resonance ϵ_0. For simplicity, we further assumed $\epsilon_0 \ll \Delta$ though one must note that this is in no way essential.

In contrast, the electron tunneling rate becomes singular,

$$\Gamma_e(\omega - eV_{e_+}^{\mathrm{th}}) \simeq \gamma_e \sqrt{\frac{\Delta}{2(\epsilon_0 - \omega)}}\,\theta(\epsilon_0 - \omega). \tag{3.25}$$

Neglecting Γ_1 and Γ_2 in the broadening and considering Eq. (3.21) for $V = eV_{e_+}^{\mathrm{th}} + \delta V$ one can write:

$$I(V) \simeq I_a(V) \simeq \frac{2e}{h}\int \mathrm{d}\omega \frac{\Gamma_e(\omega_-)\Gamma_h^{\mathrm{th},e}}{(\omega-\epsilon_0)^2 + \frac{1}{4}[\Gamma_e(\omega_-) + \Gamma_h^{\mathrm{th},e}]^2}, \tag{3.26}$$

where we also set the Fermi distributions to one and zero, respectively. To find the differential conductance peak it is convenient to shift the integration variable $\omega \to \omega + \delta V$ and then perform the bias derivative:

$$\left.\frac{\mathrm{d}I}{\mathrm{d}V}\right|_{\mathrm{peak},+} \simeq \frac{4e^2}{h}\int \mathrm{d}\omega \frac{(\epsilon_0 - \omega)\Gamma_e(\omega - eV_{e_+}^{\mathrm{th}})\Gamma_h^{\mathrm{th},e}}{\left[(\omega-\epsilon_0)^2 + \frac{1}{4}[\Gamma_e(\omega - eV_{e_+}^{\mathrm{th}}) + \Gamma_h^{\mathrm{th},e}]^2\right]^2}. \tag{3.27}$$

From this expression one can consider two different regimes. Consider first the situation where the hole tunneling dominates the broadening of the resonance. Then, the range $\epsilon_0 - \omega \approx \Gamma_h^{\mathrm{th},e}$ dominates the integral. Inserting this into Eq. (3.25) one finds the characteristic electron tunneling rate $\Gamma_e^{\mathrm{th},e} = \gamma_e[\Delta/2\Gamma_h^{\mathrm{th},e}]^{1/2}$. Comparing the two threshold rates in the broadening one finds that the hole tunneling rate dominates provided that $\Gamma_h^{\mathrm{th},e} \gg (\gamma_e^2\Delta)^{1/3}$. Note that this is possible for highly asymmetric electron-hole wave functions and $\epsilon_0 \ll \Delta$. Neglecting the electron tunneling rate in the broadening one can write:

$$\begin{aligned}\left.\frac{\mathrm{d}I}{\mathrm{d}V}\right|_{\mathrm{peak},+} &\simeq \frac{4e^2}{h}\int_{\epsilon_0}^{\infty} \mathrm{d}\omega \frac{\Gamma_e^{\mathrm{th},e}\sqrt{\frac{\epsilon_0-\omega}{\Gamma_h^{\mathrm{th},e}}}}{(\Gamma_h^{\mathrm{th},e})^2\left[(\frac{\epsilon_0-\omega}{\Gamma_h^{\mathrm{th},e}})^2 + \frac{1}{4}\right]^2} \\ &= \frac{4e^2}{h}\frac{\Gamma_e^{\mathrm{th},e}}{\Gamma_h^{\mathrm{th},e}}\int_0^{\infty}\mathrm{d}x \frac{x^{1/2}}{\left[x^2+\frac{1}{4}\right]^2} = \frac{8\pi e^2}{h}\frac{\gamma_e\epsilon_0^{3/4}}{\gamma_h^{3/2}\Delta^{1/4}}.\end{aligned} \tag{3.28}$$

If, on the contrary, the broadening is dominated by the electron tunneling rate, the integral is dominated by the range $\epsilon_0 - \omega \approx \Gamma_e(\omega - eV_{e_+}^{\mathrm{th}})$, which leads to a different characteristic electron tunneling $\Gamma_{e,2}^{\mathrm{th},e} = (\gamma_e^2\Delta/2)^{1/3} \gg \Gamma_h^{\mathrm{th},e}$. Analogously to the previous calculation one finds:

$$\left.\frac{\mathrm{d}I}{\mathrm{d}V}\right|_{\mathrm{peak},+} \simeq \frac{4e^2}{h}\frac{\Gamma_h^{\mathrm{th},e}}{\Gamma_{e,2}^{\mathrm{th},e}}\int_0^{\infty}\mathrm{d}x\frac{x^{5/2}}{\left[x^3+\frac{1}{4}\right]^2} = \frac{8\pi e^2}{9h}\frac{\gamma_h\Delta^{1/6}}{\gamma_e^{2/3}\epsilon_0^{1/2}}. \tag{3.29}$$

One thus finds two possible behaviors depending on the relation between the electron and hole tunneling rates. An analogous calculation can be carried out at the negative threshold bias $eV_{h_-}^{\mathrm{th}} = -\Delta - \epsilon_0$ for which the roles of the two rates interchange. Note that for very asymmetric electron and hole wave functions, say $v^2 \gg u^2$, the relation (3.28) is valid at positive bias, while the equivalent of (3.29) at negative bias would take place. This is the situation of the orange curve in Fig. 3.2, explaining why the conductance peak is larger at positive bias than at negative ones.

In summary, single-particle currents dominate the total current at low junction conductances while resonant Andreev reflections dominate at sufficiently high junction conductances. We have explained the different contributions to the current in terms of relaxation and tunneling rates. The activation thresholds of the latter are important to understand the peaks position in the bias voltage. The broadening induced by the tunneling rates plays a crucial role in the signatures at high junction conductances, revealing that a treatment to all orders in the tunneling amplitude is necessary. These concepts play a central role in Chapter 7, where we generalize these results to include photon-assisted tunneling processes across the junction.

3.4 YSR STATES AS A BASIS FOR MAJORANA QUASIPARTICLES

This Section explains how chains of magnetic adatoms can provide a platform for topological superconductivity. The initial proposals by [Cho+11; NP+13] has motivated a number of theoretical studies [NTN13; Kli+13; BS13; VF13; PGO13; PGO14; P+̈14; Pen+15b]. The basic idea is to use the subgap YSR states to create a one-dimensional band centered around the YSR state energy. To realize topological superconductivity it is necessary that this band crosses the Fermi energy. The band width is set by the magnitude of the coupling between the YSR states of the magnetic impurities. It is thus desirable to achieve strong coupling between the YRS states. This has motivated research into quasi-two-dimensional superconducting substrates such as $NbSe_2$ [Mén+15; Kez+18a; SM19; GO19; Lie+19] , where the wave functions of the YSR decay more slowly than for three-dimensional substrates, see Eq. (3.9).

Note that one has some control over several of the relevant physical quantities of this kind of setup. First, there are different possible choices for the magnetic adatom as well as the superconducting substrate. The different possible combinations provide a variety of YSR state energies, wave function shapes and spatial extents, superconducting gaps and spin-orbit couplings. Finally, one can also choose the distance between the adatoms to regulate their hybridization, thus controlling the width of the YSR band.

In Section 2.4.2, we explained how to engineer topological superconductivity out of three common physical ingredients: Zeeman splitting, spin-orbit coupling and s-wave superconductivity. Magnetic adatom chains on top of a superconducting substrate combine or emulate these ingredients. There are two possible magnetic orderings for a chain of magnetic adatoms: ferromagnetic ordering and a spin helix. Ferromagnetic ordering is perhaps more straightforward to understand as it more closely resembles the recipe given in Section 2.4.2 to obtain topological superconductivity. Due to the magnetic character of the adatoms, the one-dimensional band of the adatom chain is spin polarized, emulating the low energy band of a Zeeman-split pair of bands in the presence of a magnetic field. Spin-orbit coupling can be present in either the magnetic adatom or in the superconducting substrate. However, when originating in the adatoms it can be strongly suppressed due to the strong exchange coupling, a suppression not present when originating from the superconducting substrate [OPP17]. Finally, s-wave superconductivity is contributed by the substrate hosting the adatoms.

The formation of a spin helix was discussed in [NP+13; PGO13; VF13]. In this case, the magnetic orientation of the adatoms has a varying texture along the chain. Thus, the YSR states making up the chain are polarized in different directions and a Cooper pair of the superconducting substrate can tunnel into the chain provided its spin-up and spin-down electron enter through different sites of the chain. Such a process induces p-wave superconductivity without the need of spin-orbit coupling [OPP17]. It is worth noting, though, that these two possible spin orderings are related by a unitary transformation [Bra+10].

Shortly after the theoretical proposals, an experiment reported the observation of Majorana quasiparticles in ferromagnetic adatom chains [NP+14]. They reported the observation of zero-bias peaks at the ends of adatom chains consistent with the presence of Majorana quasiparticles. The ability to probe different positions of the chain with an STM is a considerable advantage with respect to nanowire experiments, which only rely on transport measurements. A subsequent experiment using superconducting STM tips found similar, yet non-conclusive evidence of the presence of Majorana quasiparticles in such adatom chains [Rub+15a]. Further experiments have reported similar findings [Paw+16; Fel+16; Kim+18].

4 | MODULATED SSH MODEL

4.1 INTRODUCTION

This Chapter is based on Ref. [AGO20]. The concept of the bulk-boundary correspondence explained in Section 2.2 and the Su-Schrieffer-Heeger (SSH) model introduced in Section 2.3 play a central role in the present Chapter.

Two recent experiments by Rizzo et al. [Riz+18] and Gröning et al. [Gr18] have reported the observation of energy bands engineered from a sequence of topological domain-wall states. Both experiments exploited graphene nanoribbons with alternating widths. The segments of different widths were predicted to be topologically distinct [CZL17], leading to the emergence of topological boundary states localized at the domain walls due to the bulk-boundary correspondence. These topological domain-wall states hybridize across the regions of fixed nanoribbon width and form bands which have themselves interesting topological properties.

Due to a difference in the bulk gaps, the domain-wall states decay with different localization lengths into the two types of segments, leading to alternating coupling strengths. Thus, the domain-wall states form an effective Su-Schrieffer-Heeger (SSH) chain [SSH79], and an analysis of the Zak phase of the system successfully predicts the presence or absence of edge states at the ends of the nanoribbon [Riz+18; Zak89; RBB17]. These two experiments are an excellent example of the potential of topological states of matter as building blocks of systems with interesting properties. The ability to place topological boundaries at will translates into spatial control over states whose energies are separated from the rest of the spectrum by a gap. This, together with the robust character of the domain-wall states, allows for the engineering of interesting systems.

Here, we propose a minimal model that is motivated by the essential physics of these experiments. Our model is a modified SSH model with a periodically modulated dimerization. As explained in Chapter 2.3, the SSH model is characterized by dimerized hopping strengths $t \pm \Delta/2$, which yield a two-band spectrum with band gap 2Δ. The topological and trivial phases are separated by a closing of this gap. In our modulated SSH model, we choose the dimerization Δ to be periodically varying along the chain. Sign changes of Δ and hence of the gap are associated with domain walls between different topological phases and host localized topological domain-wall states in the same fashion as in the graphene nanoribbon experiments. We design the model such that these domain-wall states realize emergent SSH chains and thoroughly analyze the resulting end states and spectrum. We show how the various configurations of end states exhibited by our model can be predicted on the basis of the Zak phases of its bands.

Our model is a generalized Aubry-André-Harper (AAH) model [GSS13] [LGC15; Zha+17b; ZCL16; Liu+17; CFG16], specifically, a so-called 'off-diagonal' AAH model. In addition to topological domain-wall states, the model also has interesting physics associated with commensurability effects between the periodicity of the lattice and the modulation of the dimerization. The original AAH model describes a chain with periodically varying onsite potential [Har55; AA80]. It has been broadly studied as it describes lattice electrons in two dimensions under a perpendicular magnetic field and exhibits a localization-delocalization transition. Its spectrum was found to depend fractally on the periodicity, as captured by the celebrated Hofstadter butterfly [Hof76]. In this Chapter, we present the corresponding butterfly spectrum of our model, which exhibits the topological domain-wall states and the emergent SSH chains they form.

4.2 THE MODEL

The Hamiltonian of the modulated SSH model takes the form

$$\mathcal{H}^{\text{SSH}} = \sum_j \left[t + (-1)^j \Delta_j/2\right] c_j^\dagger c_{j+1} + \text{h.c.}, \tag{4.1}$$

where c_j annihilates a fermion at site j of the chain. For a constant $\Delta_j = \Delta$, this is the conventional SSH model with dimerized hopping amplitudes $t \pm \Delta/2$. We consider the dimerization Δ_j to be modulated along the chain. For slowly-varying Δ_j, the chain is effectively locally dimerized and Δ_j controls the local gap between the two bands. We engineer this model to capture the main ingredients of the nanoribbon experiments, namely: (*i*) alternating topological and trivial regions and (*ii*) alternating hybridization of the states arising at the resulting domain walls. Ingredient (*i*) can be realized by a sinusoidal variation of the gap,

$$\Delta_j' = \beta \cos\left(2\pi\xi j + \phi\right), \tag{4.2}$$

where β is the amplitude, ξ its wavevector, and ϕ a phase. Regions of positive and negative Δ_j' correspond to distinct topological phases and domain-wall states arise near locations where $\Delta_j' = 0$. This leads to equally spaced domain-wall states with uniform hybridization. Ingredient (*ii*) is readily obtained by including a constant offset,

$$\Delta_j = \alpha + \beta \cos\left(2\pi\xi j + \phi\right). \tag{4.3}$$

The offset α must be chosen to satisfy $|\alpha| < |\beta|$ for Δ_j to change sign. The wavevector ξ, together with the ratio between α and β, determine the lengths of the alternating topological and trivial phases. The dimerization only allows for unit cells with an even number of lattice sites for commensurate ξ. For this reason, we write general commensurate ξ as $\xi = p/2q$ with p and q coprime integers, giving a modulated SSH chain with $2q$ sites per unit cell and $2q$ bands.

With a dimerization as defined in Eq. (4.3), the distance and the gap between the topological domain-wall states alternate. Thus, their hybridization dimerizes and these states form an effective SSH chain on their own, similar to the topological domain-wall states of the graphene nanoribbon experiments [Riz+18; Gr18]. This emergent SSH chain is depicted in Fig. 4.1a, where Δ_j is plotted for a finite chain. The emergent SSH chain behaves just like a conventional SSH chain. It has a trivial, as well as a topological phase with its associated end states. Notably, the modulated SSH chain exhibits more intricate physics as we show below.

The modulated SSH model (4.1) retains time-reversal and chiral symmetries of the original SSH chain. The chiral symmetry $\hat{\mathcal{S}}$ has its origin in that $\mathcal{H}$ involves only nearest-neighbor hopping terms. It acts on the site operators as:

$$\hat{\mathcal{S}} c_j \hat{\mathcal{S}}^{-1} = (-1)^j c_j^\dagger, \tag{4.4}$$

leaving the Hamiltonian (4.1) invariant:

$$\hat{\mathcal{S}} \mathcal{H} \hat{\mathcal{S}}^{-1} = \mathcal{H}. \tag{4.5}$$

In first quantization language, chiral symmetry is a unitary operator that anticommutes with the hamiltonian. For example, the low-energy continuum form of the modulated SSH model, valid for slowly-varying Δ_j,

$$H_{\mathrm{c}} = 2tk\sigma_z + \Delta(x)\sigma_y, \tag{4.6}$$

where σ_i $(i = x, y, z)$ denotes Pauli matrices acting in the basis of left and right movers, has $S = \sigma_x$ as its chiral symmetry operator. Indeed, as H_c does not involve σ_x, it anticommutes with this Pauli matrix, $\{\sigma_x, H_c\} = 0$. The chiral symmetry is responsible for the existence of the zero-energy states at the end of the chain and at the domain walls, it forces the eigenenergies of first-quantized non-interacting hamiltonians to come in pairs of opposite sign implying that isolated zero-energy states are protected against local perturbations. The original SSH chain also has, by construction, an inversion-symmetric unit cell. This is not necessarily true for the modulated SSH model, in which the phase ϕ can shift the modulation of the gap within the unit cell. A unit cell spanning from sites $j = 1$ to $j = 2q$ is inversion-symmetric for $\phi = 0, \pi$.

For slowly-varying $\Delta(x)$ and close to one of its zeros, one can linearize the mass term in Eq. (4.6),

$$H_{\mathrm{c}}^{\mathrm{SSH}}(x) \approx 2tk\sigma_z + \lambda(x - x_0)\sigma_y, \tag{4.7}$$

with $|\lambda| = 2\pi\xi\sqrt{\beta^2 - \alpha^2}$ the slope of the mass variation. This Hamiltonian has has the same structure as the one-dimensional case of Eq. (2.8) (with $k_y = 0$) differing only by a rotation in Pauli matrix space. Thus, the results of Chapter 2.3 also apply for the Hamiltonian of Eq. (4.7): it is diagonalized by harmonic-oscillator-like eigenfunctions localized at x_0 with energies,

$$E_n^{\mathrm{SSH}} = \pm 2\sqrt{t|\lambda|n}, \tag{4.8}$$

where n is a non-negative integer. Thus, each domain wall hosts a discrete set of localized domain-wall states. Those states with energies below the maximal value of Δ_j are localized at their respective domain wall. This implies that the modulated SSH chain can generate not only one but several emergent SSH chains.

Incidentally, similar physics is also present in the AAH model [Har55; AA80]. When the onsite potential is close to perfect dimerization (i.e., has a period close to two lattice sites), the low-energy description of the AAH model is also a Dirac Hamiltonian with a slowly-varying mass. As in the modulated SSH model, sign changes of the mass constitute topological domain walls and support topological states.

4.2.1 EFFECTIVE MODEL OF THE EMERGENT SSH CHAINS

Taking the n-th domain-wall state arising at each zero of Δ_j and keeping the hopping only to immediate neighbors, one obtains an effective Hamiltonian for the n-th emergent SSH chain,

$$H_n = E_n \mathbb{I} + (t_{n1} + t_{n2} \cos 2k)\sigma_x + t_{n2} \sin 2k \sigma_y, \tag{4.9}$$

where, for small ξ, E_n is well approximated by Eq. (4.8) and $t_{n1/2}$ are the intra- and intercell hoppings to immediate neighbors (assumed real). This Hamiltonian corresponds to an SSH chain shifted in energy by E_n, and thus preserves chiral symmetry about E_n,

$$E = E_n \pm \sqrt{(t_{n1} - t_{n2})^2 + 4t_{n1}t_{n2} \cos^2 k}. \tag{4.10}$$

The relation between the intra- and the intercell hoppings sets the emergent SSH chain into the trivial ($t_{n1} > t_{n2}$) or the topological ($t_{n1} < t_{n2}$) phase. In either case, due to the exponential localization of the domain-wall states, the weak hopping is exponentially smaller than the strong one and the resulting bands are weakly dispersing, that is

$$E \simeq E_n \pm (t_{ns} + t_{nw} \cos 2k), \tag{4.11}$$

with t_{ns} (t_{nw}) the stronger (weaker) hopping.

For energies $|E_n|$ comparable to the maximal value of $|\Delta_j|$, it is no longer justified to keep only immediate neighbors as the wave functions extend over greater distances. The SSH model with long-range hopping was studied in Refs. [LXC14; PG+19]. In particular, including the hopping to third neighbors breaks chiral symmetry due to a term $t_3 \cos 2k\mathbb{I}$.

4.2.2 END STATES

To understand and classify the end states of the modulated SSH chain, one needs to consider the nature of both the microscopic and the emergent SSH chains. The microscopic SSH chain is in the topological (non-topological) phase if it terminates in weak (strong) bonds, i.e., if the outermost bonds of the chain are of the type $t - \delta$ with δ positive (negative). The emergent SSH chains can be characterized in an analogous manner. Thus, there are four possible configurations which we label as $\{(m, e)\} = \{(n, n), (n, t), (t, n), (t, t)\}$, where the first and second entries correspond to the microscopic and the emergent SSH chains, respectively, and n and t stand for 'non-topological' and 'topological'. Considering a finite chain defined by Eqs. (4.1) and (4.3), with $\phi = 0$ and spanning from $j = 1$ to $j = N$, these four configurations are uniquely determined by the signs of α and β. The one-to-one correspondence with the configurations ordered as written above is $\{(\text{sgn}(\alpha), \text{sgn}(\beta))\} = \{(-1, -1), (+1, -1), (+1, +1), (-1, +1)\}$. Each of these configurations gives rise to a different set of end states, differing in their number and in their energetics. The (n, n) configuration is trivial and we do not discuss it further.

We explore these configurations by diagonalizing finite chains. We first focus on $p = 1$ referring to a discussion of more general cases below. We begin with the (n, t) configuration (Fig. 4.1). This configuration is the most transparent as its topological properties arise only from the emergent SSH chains. These,

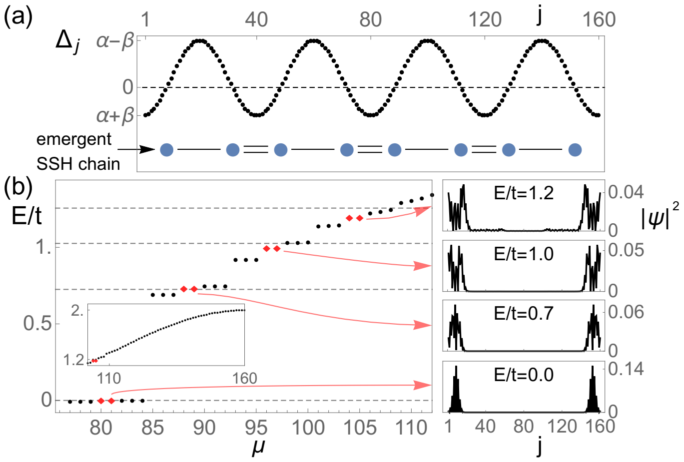

FIGURE 4.1: (n, t) configuration. (a) Plot of Δ_j for a finite chain of four unit cells with parameters $4\alpha = -\beta = t$, $p = 1$, $q = 20$ and $\phi = 0$. The blue dots below represent the domain-wall states arising at the zeros of Δ_j. The weaker (one line) and stronger (two lines) bonds indicate that they form an emergent SSH chain. (b) Eigenenergies up to $|\alpha| + |\beta|$ in ascending order with μ enumerating the states. Four different sets of eight states with gaps between them are visible. Higher energy states are plotted in the inset. The dashed lines correspond to $0.93E_n^{\text{SSH}}$ for $n = 0, 1, 2$ and 3, see Eq. (4.8). The red diamonds represent the end states of the emergent SSH chains. The probability density of one of the two end states of each group is plotted to the right of the main panel, with a pink arrow indicating the correspondence.

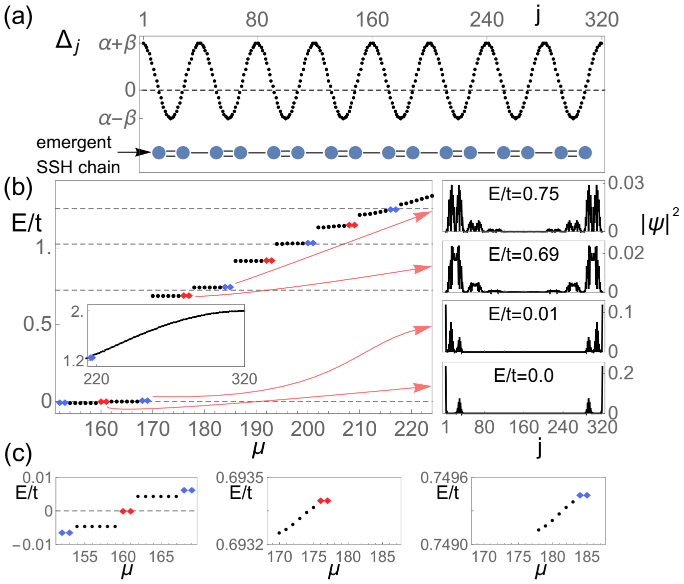

FIGURE 4.2: (t, n) configuration. Equivalent plots to those in Fig. 4.1 for $4\alpha = \beta = t$ and a twice as long chain (eight unit cells). A longer chain was chosen to make the exponential localization of the end states more visible. In this case, the emergent SSH chains are not in the topological phase. Nonetheless, there are edge states due to the microscopic SSH chain terminating in a weak bond. These states appear close in energy to the emergent SSH bulk states and extend over great distances in units of site spacing. End states within emergent SSH band gaps are shown in red, while those between emergent SSH chains with neighboring n are shown in blue. The panels in (c) are closeup regions of the main panel in (b) corresponding to the $n = 0$ (left) and the $n = 1$ (middle and right) emergent SSH chains. The latter was separated into two plots to show the small bandwidth of the emergent-SSH bulk states (black dots).

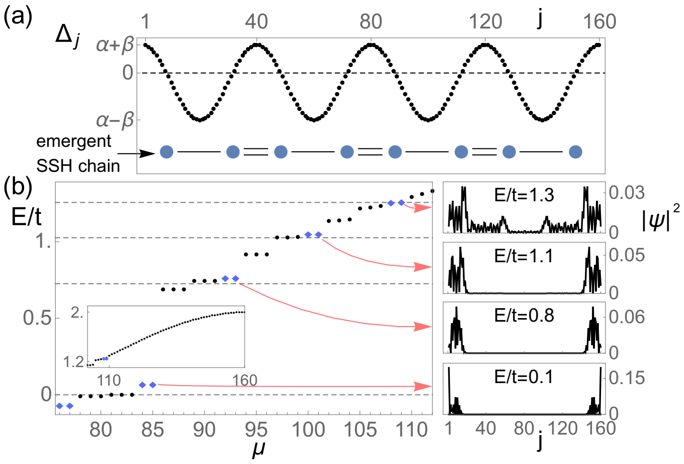

FIGURE 4.3: (t, t) configuration. Equivalent plots to those in Fig. 4.1 for $-4\alpha = \beta = t$. The emergent SSH physics remains the same but the energies of the edge states increases, sitting in the gaps between emergent SSH chains with neighboring n (blue diamonds). The microscopic SSH end states hybridize with the $n = 0$ emergent SSH end states.

schematically depicted in the lower part of Fig. 4.1a, are terminated at both ends by weak bonds and are thus in the topologically nontrivial phase. Hence, they are expected to support end states falling in energy within the energy gaps of the corresponding emergent SSH bands. For illustration, we diagonalize a finite modulated SSH chain with a Δ_j as shown in Fig. 4.1a. The chain contains four unit cells, each with two zeros of Δ_j. Thus, there are eight domain walls hosting states and each emergent SSH chain is formed by eight states, as depicted in the lower part of the plot.

Figure 4.1b shows the positive eigenenergies of this finite chain in ascending order with μ enumerating the states. Due to chiral symmetry, the negative eigenenergies are obtained from $E_\mu \to -E_\mu$. Four groups of eight states each can be seen, which originate from the emergent SSH chains formed by the domain-wall states of Eq. (4.8) with $n = 0, 1, 2, 3$. The red diamonds indicate the in-gap end states of these chains, while the black dots correspond to the weakly dispersing bulk states mentioned above. The remaining states at higher energies are plotted in the inset and form a continuum. The probability density of one end state of every emergent SSH chain is plotted to the right of the main panel, with a pink arrow indicating the correspondence. The end states are localized not at the ends of the entire chain, but of the emergent SSH chains, i.e, at the first and last zeros of Δ_j.

Equivalent plots for the (t, n) configuration and a twice as long chain are shown in Fig. 4.2. In this configuration, the emergent SSH chains terminate in strong bonds and are thus in the topologically trivial phase. On the other hand, the microscopic SSH chain is in the topologically nontrivial phase and hence is expected to support end states. Interestingly, Fig. 4.2b shows the presence of end states in every gap of the spectrum, i.e., in the gaps of the emergent SSH chains and in the gaps between emergent SSH chains with neighboring n, hinting towards a topologically nontrivial index associated to every gap. These end states appear close in energy to the bulk sates (see Fig. 4.2c, for closeups of the $n = 0$ and $n = 1$ emergent SSH chains in panel (b)). Near zero energy, the end states have a sharply localized amplitude at the end of the chain as well as less localized amplitude at the closest zeros of Δ_j (see the two lower probability density panels).

The corresponding plots for the (t, t) configuration are shown in Fig. 4.3. In this case, both the microscopic and the emergent SSH chains are in the topological phase. This configuration shows end states in the gaps between emergent SSH chains with neighboring n but not within the bulk gaps of each emergent SSH chain. For example, there are no end states at zero energy since the end states of the microscopic SSH chain and those of the $n = 0$ emergent SSH chain hybridize (see lower right panel in Fig. 4.3b), shifting in energy outside the $n = 0$ emergent SSH band gap. More generally, this configuration can be thought of as a 'superposition' of the previous two: (t, t) exhibits end states in the gaps for which only one of the configurations (n, t) and (t, n) exhibits end states.

In the following Section, we show how these observations can be understood and predicted based on the bulk spectrum through the study of the Zak phase of the modulated SSH chain.

4.2.3 ZAK PHASE

The topological character of the bands of the modulated SSH model with inversion-symmetric unit cells can be captured through the Zak phase [Zak89; RBB17], which was introduced in Chapter 2.3. For inversion symmetric unit cells, the Zak phase can only take the values 0 and π (mod 2π). A phase of π indicates a topologically nontrivial band. We define a $\mathbb{Z}_2$ index based on the Zak phase in each spectral gap. For n-th gap, one has

$$\mathbb{Z}_{2,n} = \frac{1}{\pi} \sum_{i}^{i_n} \gamma_i \mod 2, \tag{4.12}$$

where the sum runs over the i_n bands below the n-th gap and γ_i is the Zak phase of the i-th band. As discussed in Chapter 2.3, this $\mathbb{Z}_2$ index based on the Zak phase indicates the parity of an integer topological index $\mathbb{Z}$. We find the $\mathbb{Z}_2$ index sufficient to correctly predict the presence or absence of edge states for a given spectral gap. We calculate the Zak phase numerically as [Res94; Res00]:

$$\gamma_i = i \log \prod_{j=1}^{N} \left\langle u_{i,k_j} \middle| u_{i,k_{j+1}} \right\rangle, \tag{4.13}$$

with u_{i,k_j} the eigenstate of band i for momentum k_j, and k_j a cyclic discretization of the Brillouin zone with $k_{N+1} = k_1$.

Figures 4.4a, b, and c, show the spectra for an infinite modulated SSH chain in the (n, t), (t, n), and (t, t) configurations, respectively. We plot the positive part of the spectrum plus the first negative-energy band. The spectra of the different configurations are related to one another by a shift of the unit cell or a change of sign in the dimerization. A shift of the unit cell leads to identical spectra, while, due to the offset α, a change of sign in the dimerization leads to different hopping strengths and hence to a different spectrum. These differences (already imperceptible in Fig. 4.4) become smaller for smaller ξ. Bands carrying zero Zak phase are plotted in black, while bands carrying π Zak phase are plotted in blue. The light-red coloring indicates the gaps with $\mathbb{Z}_2 = 1$. Comparing the spectra of Fig. 4.4a and Fig. 4.4b one sees that the bands are divided into two disjoint sets with different Zak phases: a high-energy set of bands composed of the highest and lowest energy bands (black bands in Fig. 4.4a), and a low-energy set of bands encompassing the remaining bands (blue bands in Fig. 4.4a) and containing the emergent-SSH bands. The number of bands in each set depends on the numerical values of α and β. A higher (lower) maximal value of the gap leads to more (less) bands in the low-energy set. One important feature is that the number of negative- (and positive-) energy bands in the high-energy set is always odd. This is necessary for the topological/trivial character of the high-energy set of bands to have an impact on the number of end states at energies closer to zero. It is also worth noticing that bands at energies well above the maximal value of the gap, for which one does not expect domain-wall states, still belong to the low-energy set of bands, exhibiting the same Zak phase as the emergent-SSH bands.

The spectra in Fig. 4.4 correspond to a modulated SSH chain with $\xi = p/2q$, with $p = 1$ and $q = 20$, that is, 40 sites per unit cell (40 bands). In this case, where $q = n_{\text{even}}$, the Zak phases of the high- and low-energy set of bands are set by the microscopic- and emergent-SSH outer bonds, respectively. Thus, in the (n, t) configuration (Fig. 4.4a), the high-energy set of bands (seven highest and lowest energy bands) carry a zero Zak phase (plotted in black), while the low-energy set of bands carry π Zak phase (plotted in blue). As a consequence, the gap at zero energy has $\mathbb{Z}_2 = 1$. Adjacent gaps separated by a topologically nontrivial band have different $\mathbb{Z}_2$ indices. End states are expected to be present in gaps with $\mathbb{Z}_2 = 1$. The first two bands shown correspond to the $n = 0$ emergent SSH chain (multiplied by a factor of 10 for clarity.) The next two bands correspond to the $n = 1$ chain and so on. The Zak phase predicts the presence of end states within the bulk gaps of the emergent SSH chains. As $\mathbb{Z}_2 = 0$ for the gaps between bands of emergent SSH chains with neighboring n, there are no end states associated with these gaps. Beyond the energy $|\alpha| + |\beta|$ the gaps are exponentially small, and the end states predicted by the $\mathbb{Z}_2$ number, though in principle present, extend over great distances. The predictions of the Zak phase match completely with the end states found in Fig. 4.1b for a finite chain in this configuration.

In the (t, n) configuration (Fig. 4.4b), both outer bonds change with respect to panel (a). The stronger outer bond of the emergent SSH chains sets a zero Zak phase for the emergent-SSH set of bands. Conversely, the weaker outer bond of the microscopic SSH chain sets a π Zak phase for the high-energy set. Consequently, all the energy gaps of the low-energy set of bands have $\mathbb{Z}_2 = 1$, explaining the presence of the many end states exhibited by the corresponding finite chain in Fig. 4.2.

Finally, in the (t, t) configuration (Fig. 4.4c) both the microscopic and the emergent SSH chains are in the topological phase and, as a result, every band in the spectrum is topological. The gaps of the emergent SSH chains have a topological index $\mathbb{Z}_2 = 0$, while the gaps between bands of emergent SSH chains with neighboring n are nontrivial. Hence, the end states of the finite chain shown in Fig. 4.3 fall within the latter gaps, and no zero-energy end states are present.

The case $p = 1$, $q = n_{\text{even}}$ is particularly transparent as each set of bands is topological (trivial) if the corresponding outer bond is weak (strong). Figure 4.5 shows an equivalent plot for the case $p = 1$, $q = n_{\text{odd}} = 21$, in which the high-energy set of bands exhibits the opposite behavior *if* the low-energy set is nontrivial. Thus, the topological character of the high-energy set of bands is dependent on both the microscopic and the emergent outer bonds. Compared to the previous case, the low-energy set of bands has two additional bands (one more each at positive and negative energies). This enforces this change of behavior needed for the end states to be present in the same gaps as in the previous case (compare the light-red coloring of Figs. 4.4 and 4.5).

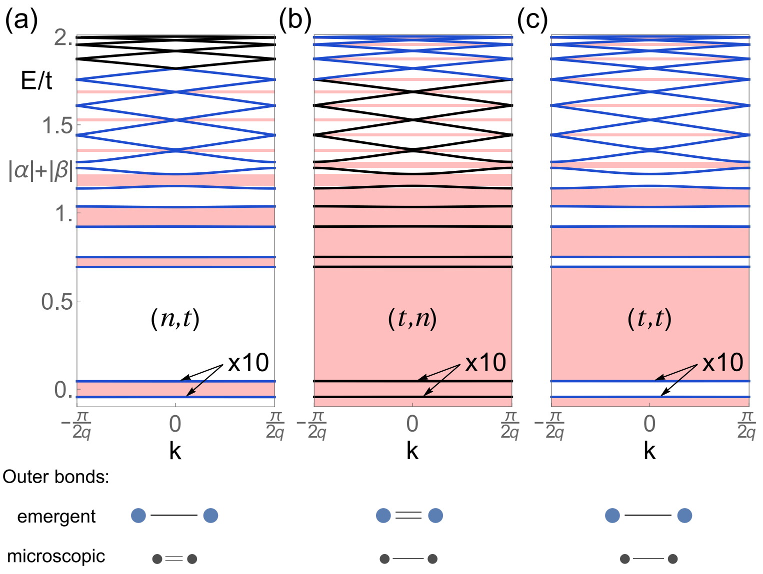

FIGURE 4.4: First negative and positive energy bands of an infinite chain for the configurations: (a) (n, t), (b) (t, n), (c) (t, n). Blue (black) bands carry a Zak phase of π (zero). The colored regions between the bands indicate gaps with topologically nontrivial $\mathbb{Z}_2$ number. The first two bands shown are multiplied by a factor of 10 for clarity. The lower part of each plot shows the outer bonds of a finite chain build with the corresponding unit cell. Parameters: $4|\alpha| = |\beta| = t$, $p = 1$, $q = 20$.

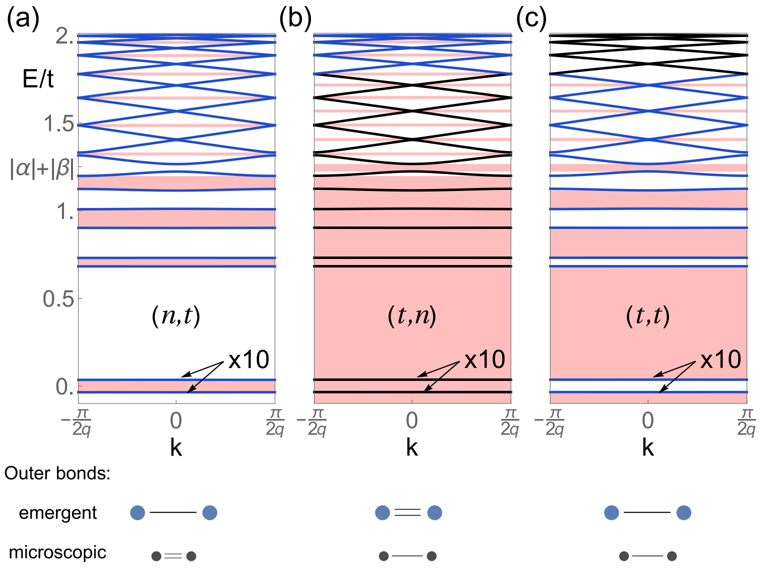

FIGURE 4.5: Equivalent to Fig. 4.4 with $q = 21$. In this case the low-energy set of bands has two more bands (one at positive and one at negative energies) leading to a change in behavior for the Zak phase of the high-energy set of bands (see main text).

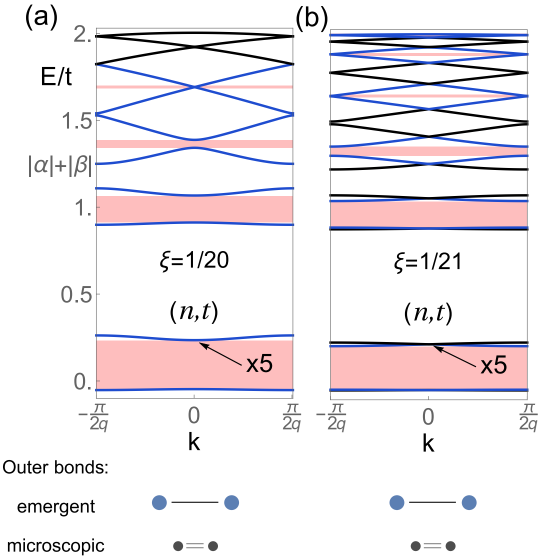

FIGURE 4.6: Spectra of the (n, t) configuration for (a) $p = 1$, $q = 10$ and (b) $p = 2$, $q = 21$. Wavevectors ξ with neighboring denominators n_1 and $n_1 + 1$ differ in the number of bands by $n_1 + 2$. Bands in (a) appear as pairs of bands in (b) which keep the overall topological character of the original band. As a consequence, gaps in (a) and their equivalents in (b) have the same topological index $\mathbb{Z}_2$ (compare red coloring).

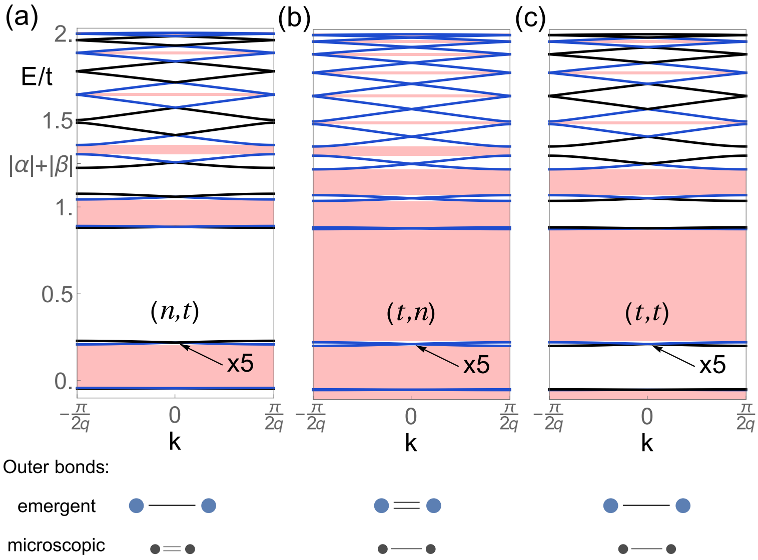

FIGURE 4.7: Equivalent to Fig. 4.4 with $p = 2$, $q = 21$. In spite of the band folding and different assignments of the Zak phases, the $\mathbb{Z}_2$ index remains the same for the equivalent gaps to those in Figs. 4.4 and 4.5 (compare red coloring).

Finally, we consider cases with $p > 1$. In the AAH model, a wavevector $\xi' = p'/q'$ close in value to a fraction $1/n_b$ leads to an spectrum divided into n_b groups of bands with p' bands per group. This is also true for the modulated SSH model. The two models exhibit different total numbers of bands. In the AAH model an irreducible wavevector $\xi' = p'/q'$ leads to q' bands while in the modulated SSH model $\xi = p'/q'$ leads to q' bands for even q' and $2q'$ bands for odd q'. We illustrate this in Fig. 4.6 which compares two spectra in the (n, t) configuration for (a) $p = 1$, $q = 10$ and (b) $p = 2$, $q = 21$. Roughly, single bands in panel (a) appear in groups of $p = 2$ bands in panel (b) albeit with a slightly lower energy. The overall topological character of each pair of bands matches with the topological character of the single bands in panel (a). More generally, a single band with trivial (nontrivial) Zak phase splits into p bands with an even (odd) number of trivial (topological) bands. Due to this behavior the gaps in (a) and the equivalent ones in (b) have the same $\mathbb{Z}_2$ index (compare red coloring). This is also true for the other two configurations (see Fig. 4.7). Notably, the emergent SSH bands in the (t, n) configuration split into two bands with nontrivial Zak phase, preventing the appearance of end states in the small gaps separating them. For other cases, the gaps within a group of p bands can exhibit end states and the specific assignment of Zak phases in the group of bands depends on the numerical values of α and β.

In general, despite different possible behaviors of the bands in terms of their Zak phases for the different ξ, the phenomenology is common to all cases: the presence or absence of end states in the gaps of the spectra depends only on the configuration (m, e), that is, it is uniquely determined by the weak or strong character of the outermost bonds of the microscopic and emergent SSH chains. This fact can also be appreciated in the butterfly spectrum of the model presented below.

4.3 BUTTERFLY SPECTRUM

This Section introduces the butterfly spectrum of the modulated SSH model (4.1) similar to the celebrated Hofstadter butterfly. The bands formed by the topological domain-wall states and the gaps of the emergent SSH chains are visible in this kind of plot.

To generate the butterfly spectrum we plot the energy bands of infinite modulated SSH chains with different values of the wavevector $\xi = p/2q$, with p/q coprime integers, in the (n, t), (t, n), and (t, t) configurations. The spectrum has a unit periodicity in the wavevector ξ. We choose to plot the range $\xi \in (-\frac{1}{2}, \frac{1}{2})$ to keep the resemblance with the Hofstadter butterfly. Figure 4.8 shows the butterfly spectrum for $|\alpha| = 0.5t$ and $|\beta| = 1.5t$, with the energy bands shown in black. Gaps with a topological index $\mathbb{Z}_2 = 1$ for the (n, t) and (t, t) configurations are colored in red and blue, respectively. Every colored gap also corresponds to a topologically nontrivial gap in the (t, n) configuration. One can check that this is in accordance with the spectra in Figs. 4.4, 4.5, 4.6, and 4.7.

Some features of the butterfly spectrum can be readily explained. For values of ξ close to $\pm\frac{1}{2}$ the spectrum is gapped at zero energy. For these wavevectors the system behaves as a conventional SSH chain with gap $2|\alpha|$ and a bandwidth modulated by $\beta \cos\big(2\pi|\xi - \frac{1}{2}|j\big)$. The regions of maximal bandwidth host harmonic-oscillator-like states whose energies depend linearly on ξ, explaining the "Landau level" fan structures at high positive and negative energies. This

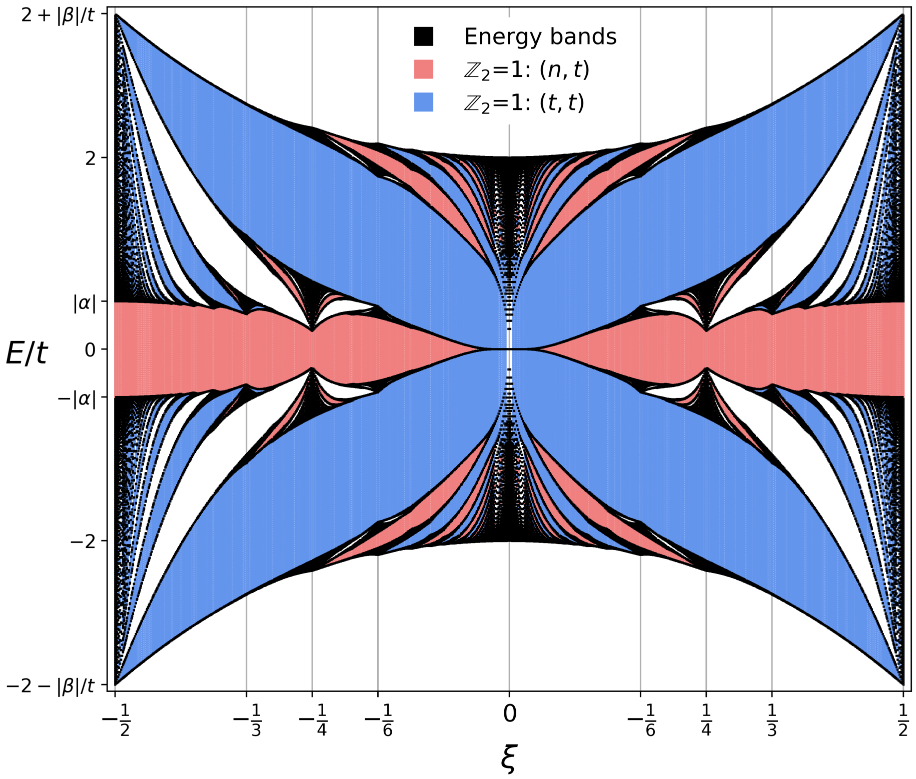

FIGURE 4.8: Butterfly spectrum of the modulated SSH model. The energy bands are plotted in black. Gaps with a $\mathbb{Z}_2 = 1$ are colored: red for the (n, t) and blue for the (t, t) configurations. For the (t, n) case, both blue and red gaps are topological. The non-zero α opens a gap at zero energies for most values of ξ. The bands around $\xi = 0$ are formed by the domain-wall states associated with topological domain walls.

feature is also present in the original Hofstadter butterfly. Having the same origin, the bands of these harmonic-oscillator-like states exhibit all the same topological or trivial character, explaining why even-numbered gaps in this region (counting from the top or bottom) are trivial for all configurations (white gaps in Fig. 4.8).

The low energy bands around $\xi = 0$ correspond to the emergent SSH chains formed by topological domain wall states (the $n = 0$ band is particularly recognizable). As $|\xi|$ increases away from zero, the gaps of the emergent SSH chains grow and become resolved. Self-similar structures can be found at other ξ values albeit gapped at zero energy due to α being nonzero.

A remarkable difference with respect to the Hofstadter butterfly is found at the band edges for values of ξ close to zero. For these values, the Hofstadter butterfly exhibits another Landau level fan due to a slow modulation of the bandwidth. In the modulated SSH model, the bandwidth in this region has a constant value of $4t$ (as long as $|\alpha| + |\beta| \leq 2t$), so that this Landau level fan structure is absent. This fact, together with the low energy gap opened by α, leads to a less pronounced self-similarity in the modulated SSH butterfly than in the Hofstadter butterfly.

To illustrate how a nonzero value of α leads to the formation of the emergent SSH bands, Fig. 4.9 shows a closeup of the low-energy, small-$|\xi|$ region of two butterfly spectra with parameters: (a) $\alpha = 0$, $\beta = 2t$ and (b) $|\alpha| = 0.5t$, $|\beta| = 1.5t$. The bands in this region are formed by the domain-wall states of the modulated SSH chain. The band of $n = 0$ states is clearly visible in both plots. The blue

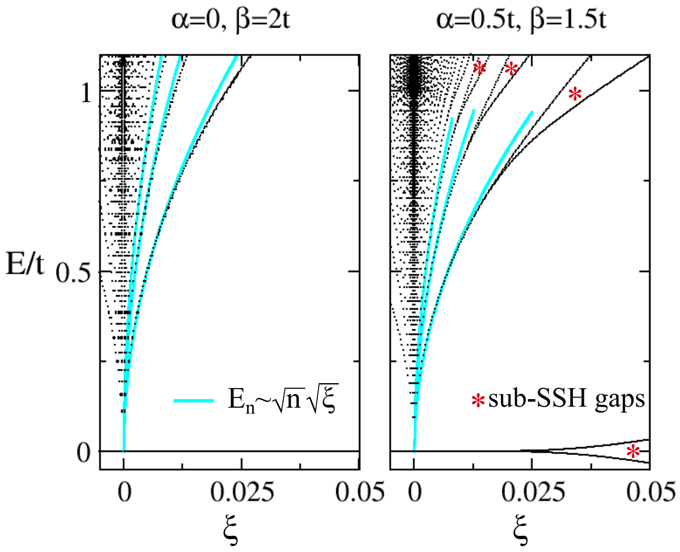

FIGURE 4.9: Close-ups of the small $\xi = p/q$, low energy regions of butterfly spectra. The blue lines follow equation (4.8) for $n = 1, 2, 3$ with the corresponding parameters. The zero energy $n = 0$ band is visible in both plots. (a) $\alpha = 0$, $\beta = 2t$. The bottom plot depicts the bound states at the topological domain walls. (b) $\alpha = 0.5t$, $\beta = 1.5t$. The non-zero α causes the domain-wall states to form emergent SSH chains (depicted in the bottom plot). The gap of the $n = 0, 1, 2, 3$ chains are marked with a red asterisk in the plot.

lines correspond to Eq. (4.8) for $n = 1, 2, 3$ with the corresponding values of α and β. The bands follow this line more accurately the smaller ξ is. As ξ grows, the domain-wall states come closer together and the approximation of an isolated zero of Δ_j of Hamiltonian (4.7) loses its validity. For Fig. 4.9a, with $\alpha = 0$, the topologically distinct regions of the chain have the same length and the domain-wall states have the same decay length in both directions. Thus, they do not dimerize and their bands remain ungapped. For Fig. 4.9b, with $\alpha \neq 0$, the domain-wall states form emergent SSH chains. As ξ grows, the domain-wall states come closer together, increasing their coupling and making the gaps of the emergent SSH chains visible in the butterfly plot. These gaps are marked by a red asterisk in Fig. 4.9b. Due to the greater spatial extent of states with higher n, these gaps become resolved for smaller ξ the higher n is.

4.4 CONCLUSION

We have introduced a modulated SSH model, in which the gap has a periodic modulation and can change sign, creating topological domain walls along the chain. The arising domain-wall states hybridize and form emergent SSH chains that can exhibit end states of their own. The model supports various end state configurations that can be explained through the Zak phase of its bands. We presented the topological character of each band gap in a compact form in a butterfly-type spectrum. This model provides a simple tight-binding framework to study the physics observed in the experiments of Refs. [Riz+18; Gr18] and serves as a toy model to explore possible end states arising in systems engineered from topological domain-wall states.

5 | YSR STATES IN THE CHARGE-DENSITY MODULATED SUPERCONDUCTOR $\mathrm{NbSe_2}$

5.1 INTRODUCTION

Reproduced in part with permission from E. Liebhaber et al. “Yu-Shiba-Rusinov states in the charge-density modulated superconductor NbSe2”. *Nano Lett.* (2019). DOI: `10.1021/acs.nanolett.9b03988`. Copyright 2019 American Chemical Society. [1] `https://pubs.acs.org/articlesonrequest/AOR-aAAqiEtJpSYEUqwaYScR`

As mentioned in Chapter 3, NbSe$_2$ has recently attracted atention as a substrate for the engineering of topological superconducting phases. The significant spatial extent of YSR states in 2D superconductors was first experimentally demonstrated in Ref. [Mén+15] with iron impurities embedded in 2H-NbSe$_2$. This work led to theoretical studies about topological state engineering in NbSe$_2$ [SM19; GO19] as well as an expermiental observation of hybridization of two YSR states in the material [Kez+18a].

The work presented in this Chapter provides another pertinent piece of knowledge for engineering of topological superconducting phases using magnetic adatoms on NbSe$_2$. Specifically, we studied experimentally and theoretically the interplay between YSR states and the charge density wave (CDW) present in NbSe$_2$. Indeed, a charge density modulation coexists with superconductivity in various transition metal dichalcogenides such as monolayer NbSe$_2$, NbSe$_3$, $2H$-NbSe$_2$, $2H$-TaSe$_2$, $2H$-TaS$_2$ and $1T$-TaS$_2$ [GVA02; Rit+13; Xi+15]. Our experiment reveals the effect of the charge density wave on the YSR state energy and symmetry of the wave function. We explain these effects within a simple theoretical model that captures the qualitative effects of this interplay.

Our findings show that the CDW environment felt by the adatom determines the symmetry of the YSR wave function. Depending on the position of the adatom relative to the CDW, the YSR wave function can exhibit behaviors ranging from three-fold symmetry to no symmetry at all. We also explain how the CDW affects the YSR energies through its effect on the local density of states and the local scattering potential. Our simple theoretical model is able to capture the experimentally observed behaviors, hinting that the underlying mechanisms are general and apply to range of materials.

---

[1] This Chapter is based on the colaboration published as Ref. [Lie+19]. The author of this thesis was only involved in the theoretical contributions to the collaboration. All the credit for the experimental results go to the experimental collaborators.

We begin the Chapter introducing $\mathrm{NbSe_2}$ in its monolayer and bulk forms, as well as its charge-density-wave order. We continue by presenting our experimental findings in Section 5.3. Finally, Section 5.4 contains the theoretical model developed and Section 5.5 our numerical results.

5.2 $\mathrm{NbSe_2}$

Many properties of $\mathrm{NbSe_2}$ have been studied in the literature. There is evidence for anisotropic as well as multiband superconductivity [HRW90; Yok+01; Boa+03; RV04; Fle+07; Gui+08a; Gui+08b; Noa+10; Noa+15], and the spin physics is highly nontrivial due to strong spin-orbit coupling, most prominently in monolayers of $\mathrm{NbSe_2}$ [Xi+16]. In this Section, we briefly introduce the material focusing on the relevant aspects for this thesis. Though our work was based on an experiment using $2H$-$\mathrm{NbSe_2}$, it is convenient to first understand monolayer $\mathrm{NbSe_2}$, which is simpler and can be regarded as the building block of $2H$-$\mathrm{NbSe_2}$.

5.2.1 **MONOLAYER** $\mathrm{NbSe_2}$

Monolayer $\mathrm{NbSe_2}$ consists of three atomic layers: one Nb layer sandwiched by two Se layers. Looked from the out of plane direction, this trilayer projects into a honeycomb lattice, with the Nb atoms occupying, say, the A sublattice, and the Se atoms (spatially on top of each other) occupying the B sublattice. The band structure can be understood by rough analogy with graphene with three important modifications:

- The sublattice asymmetry breaks the inversion symmetry opening a gap at the K points.
- The stoichiometry shows that the Fermi level lies within the valence band, leading to Fermi pockets around the K points. Also, there is an additional Fermi pocket around the Γ points [Nak+18].
- There is strong spin-orbit coupling. This leads to what is know as Ising superconductivity: in a $\mathrm{NbSe_2}$ monolayer crystal fields are in-plane due to its plane mirror symmetry; as electron momenta are also restricted to the plane, spin-orbit interactions polarize the spins in the out-of-plane direction, with opposite signs at the two K points. This causes the Fermi pockets to split into spin-polarized Fermi surfaces. This splitting is more prominent for the K-point Fermi pockets. The spin polarization allows for high in-plane critical magnetic fields [Xi+16; Xin+17].

Monolayer $\mathrm{NbSe_2}$, as well as bulk $\mathrm{NbSe_2}$, exhibits a charge density wave phase that coexists with superconductivity below its critical temperature. In comparison with the better studied bulk $\mathrm{NbSe_2}$, the CDW phase is enhanced, occurring at higher temperatures. On the other hand, the superconducting gap is smaller than in the bulk crystal [Xi+15; Uge+16; Nak+18].

5.2.2 $2H$-$\mathrm{NbSe_2}$

$2H$-$\mathrm{NbSe_2}$ is the most commonly studied form of $\mathrm{NbSe_2}$. As anticipated above, charge-density-wave order ($T_{\mathrm{CDW}} \approx 33\mathrm{K}$) coexists with superconductivity ($T_{\mathrm{c}} \approx 7\mathrm{K}$) at low temperatures [Ros+01; JMH06a; Kis+07; JM08; Web+11; Rah+12; MK13; Sou+13; Dai+14; Arg+14; Arg+15; FW15]. The superconductivity exhibits an anisotropic gap as well as multiband character [HRW90; Yok+01;

Boa+03; RV04; Fle+07; Gui+08a; Gui+08b; Noa+10; Noa+15]. The precise interplay between CDW ordering and superconductivity remains only partially understood at present [Sud+05; Kis+07; Bor+09; Cho+18a].

$2H$-NbSe$_2$ is a layered material where the basic unit are two monolayers of NbSe$_2$ rotated by 180° with respect to one another (see Fig. 5.1b). The interlayer coupling is much weaker than the intralayer couplings and the literature often refers to $2H$-NbSe$_2$ as a quasi-2D material. Due to this, YSR states in $2H$-NbSe$_2$ fall off laterally like in a 2D superconductor, instead of the faster decay one would expect for a 3D superconductor. This enhances the coupling between the YSR states of neighboring magnetic impurities [Kez+18b], potentially increasing the energy scale and thus the stability of possible topological phases. $2H$-NbSe$_2$ is also a relatively robust material which may enable one to build nontrivial adatom structures by manipulation using a scanning tunneling microscope tip.

The band structure of $2H$-NbSe$_2$ can be understood starting from the monolayer NbSe$_2$ bands. Indeed, if one neglects the weak interlayer coupling, the two trilayers of the unit cell present the same band structure profile, differing only in the spin assignments. Thus, the bulk crystal also exhibits Fermi pockets around the Γ, K and K' points, but its bands are spin degenerate, consistent with the fact that it has an inversion center located between the two NbSe$_2$ trilayers. These bands are not isotropic but present a six-fold symmetry. Moreover, these bands are predominantly derived from the Nb d-orbitals and are weakly dispersing in the out-of-plane direction even when interlayer coupling is considered. This is not the case for an Se-derived band arising around the Γ point, which shows a substantial bandwidth along the out-of-plane direction [Mat73b; Mat73a; JMH06b; CMM09].

5.2.3 CHARGE DENSITY WAVE ORDER IN $2H$-NbSe$_2$

The CDW order can be readily studied via STM imaging. Indeed, clean surface imaging reveals the modulation of the local DOS induced by the CDW superimposed on the atomic corrugation as shown in Fig. 5.1a. The CDW has a lattice constant $a_{\text{CDW}} \gtrsim 3a$, making it incommensurate with the underlying atomic lattice. Here a is the lattice constant of the triangular lattice of Nb atoms. Thus, the phase of the CDW relative to the atomic lattice varies smoothly across the surface [GOY19; Gus+19]. The close-ups show in Fig. 5.1a show two extremal cases for which the maxima coincide either with a Se atom (chalcogen-centered, CC, red circle) or a hollow site (hollow-centered, HC, green circle). Areas with Nb-centered CDW maxima (metal-centered, MC) do not appear in the STM images, as they energetically unfavourable [GOY19; Gus+19].

i) THEORETICAL DESCRIPTION OF THE CHARGE DENSITY WAVE

In the following, we present a phenomenological mean-field description of charge density waves in solids. We start with a generic Fröhlich-type Hamiltonian describing electrons coupled to phonons [Gru94],

$$\mathcal{H} = \sum_{\mathbf{k}} \epsilon_{\mathbf{k}} c^\dagger_{\mathbf{k}} c_{\mathbf{k}} + \sum_{\mathbf{q}} \omega_{\mathbf{q}} b^\dagger_{\mathbf{q}} b_{\mathbf{q}} + \sum_{\mathbf{k},\mathbf{q}} g_{\mathbf{q}} (b_{\mathbf{q}} + b^\dagger_{-\mathbf{q}}) c^\dagger_{\mathbf{k}+\mathbf{q}} c_{\mathbf{k}}. \tag{5.1}$$

Here, $c_{\mathbf{k}}$ annihilates electrons with momentum $\mathbf{k}$ and energy $\epsilon_{\mathbf{k}}$, $b_{\mathbf{q}}$ annihilates a phonon with wave vector $\mathbf{q}$ and frequency $\omega_{\mathbf{q}}$, and $g_{\mathbf{q}}$ denotes the strength of the electron-phonon coupling. Within mean-field theory, we assume that certain

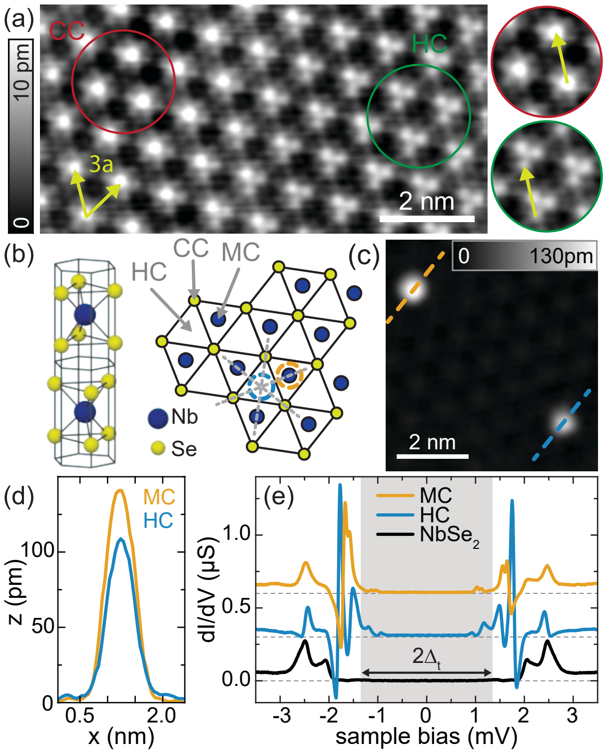

FIGURE 5.1: (a) Atomic-resolution STM images showing the incommensurate CDW modulation with close-ups of the two different regions. (b) Unit cell and top view of $2H$-NbSe$_2$, with different lattice sites labeled as HC, CC and MC. Grey dashed lines indicate mirror axes. (c) Topography of HC and MC adatoms. (d) Line profiles across the atoms shown in (c). (e) Constant-height $\mathrm{d}I/\mathrm{d}V$ spectra taken on the substrate (black) and on the atoms shown in (c) . $2\Delta_\mathrm{t}$ is indicated by the shaded area.

phonon modes (denoted by $\mathbf{Q}$) go soft due to their coupling to the electronic system and develop a finite expectation value. Restricting to the lowest Fourier components and neglecting phonon dynamics beyond the static charge-density wave (CDW) distortions, we find the mean-field Hamiltonian

$$\mathcal{H} = \sum_{\mathbf{k}} \epsilon_{\mathbf{k}} c^\dagger_{\mathbf{k}} c_{\mathbf{k}} + \sum_{\mathbf{k}} \sum_{\mathbf{Q}} g_{\mathbf{Q}} \langle b_{\mathbf{Q}} + b^\dagger_{-\mathbf{Q}} \rangle c^\dagger_{\mathbf{k}+\mathbf{Q}} c_{\mathbf{k}} \tag{5.2}$$

for the electronic degrees of freedom. Within this approach, the CDW acts on the electrons as a periodic potential $V(\mathbf{r})$. Indeed, the electron-phonon interaction term can also be expressed in real space as

$$\mathcal{H}_{\mathrm{el-ph}} = \int \mathrm{d}\mathbf{r} V(\mathbf{r}) \psi^\dagger(\mathbf{r}) \psi(\mathbf{r}), \tag{5.3}$$

where the mean-field CDW potential takes the form

$$V(\mathbf{r}) = \sum_{\mathbf{Q}} e^{-i\mathbf{Q}\cdot\mathbf{r}} g_{\mathbf{Q}} \langle b_{\mathbf{Q}} + b^\dagger_{-\mathbf{Q}} \rangle. \tag{5.4}$$

To find the vectors $\mathbf{Q}$ of the CDW in $2H$-NbSe$_2$, we consider a triangular lattice of Nb atoms with lattice vectors

$$\mathbf{a}_1 = a(1,0), \tag{5.5}$$

$$\mathbf{a}_2 = a(1/2, \sqrt{3}/2) \tag{5.6}$$

and bond length $a = 3.445\,\text{Å}$. The corresponding reciprocal lattice vectors $\mathbf{b}_i$ satisfying $\mathbf{a}_i \cdot \mathbf{b}_j = 2\pi\delta_{ij}$ are

$$\mathbf{b}_1 = \frac{4\pi}{\sqrt{3}a}(\sqrt{3}/2, -1/2), \tag{5.7}$$

$$\mathbf{b}_2 = \frac{4\pi}{\sqrt{3}a}(0,1). \tag{5.8}$$

The unit cell of the CDW has a linear dimension which is approximately three times larger than the unit cell of the atomic lattice, $\mathbf{a}_i^{\text{CDW}} \approx 3\mathbf{a}_i$ (for $i = 1, 2$). Correspondingly, the reciprocal lattice vectors of the CDW are approximately a factor of three smaller, $\mathbf{b}_i^{\text{CDW}} \approx \mathbf{b}_i/3$. Then, the first harmonics of the CDW have wave vectors

$$\begin{aligned}
\mathbf{Q}_1 &= q(1-\delta)(\sqrt{3}/2, -1/2), \\
\mathbf{Q}_2 &= q(1-\delta)(0,1), \\
\mathbf{Q}_3 &= q(1-\delta)(-\sqrt{3}/2, -1/2) = -(\mathbf{Q}_1 + \mathbf{Q}_2),
\end{aligned} \tag{5.9}$$

where $q = \frac{4\pi}{3\sqrt{3}a}$, and $\delta \ll 1$ accounts for the fact that the CDW is not exactly commensurate with the lattice. The CDW potential $V(\mathbf{r})$ is constructed from these main Fourier components,

$$V(\mathbf{r}) = V_0 \sum_{i=1,2,3} \cos(\mathbf{Q}_i \cdot \mathbf{r} + \phi_i), \tag{5.10}$$

where V_0 denotes the amplitude of the CDW potential. As will be shown below, the experiment revealed a CDW with an absolute maximum, an absolute minimum and a local minimum or saddle point. Except for $\phi_1 = \phi_2 = \phi_3$ and similar fine-tuned cases, typical choices of the phases ϕ_i yield CDW potentials with the desired symmetry and shape. For definiteness, we choose $\phi_1 = \phi_2 = 0$ and $\phi_3 = \pi/3$. We will include this electrostatic potential in a tight-binding model of $2H$-NbSe$_2$ to study its effects on the YSR states.

5.3 YSR STATES IN $2H$-NbSe$_2$

To realize topological superconductivity through a magnetic adatom chain on a superconductor one needs YSR states of neighboring adatoms to hybridize. This hybridization is particularly strong when the YSR energies of the isolated adatoms are identical and their wave functions extend sufficiently far along their connecting line [Rub+18; Cho+18b; Kez+18b; Kam+18; Kim+18]. Using NbSe$_2$ as a superconducting substrate, this is not trivial to achieve due to the CDW ordering. Indeed, as the CDW and the underlying atomic lattice are incommensurate, adatoms with equivalent atomic adsorption sites, will in general be positioned differently with respect to the CDW. In our experiment, one observes that both the energy and the wave function of YSR states depend sensitively on the adatom position relative to the CDW. This dependence on the

CDW needs to be taken into account when designing adatom structures to realize topological superconducting phases. This Section contains the main experimental results that motivated our theoretical work. In Section 5.4, we provide model calculations to understand these effects qualitatively.

5.3.1 ADATOMS IN $2H$-$\mathrm{NbSe_2}$

To isolate the effect of the CDW on the YSR states, the experiment focused on iron (Fe) adatoms on clean $2H$-$\mathrm{NbSe_2}$ surfaces instead of buried impurities, as used in previous experiments [Mén+15; Sen+19]. This provides full control over the adsorption site and allows one to compare adatoms which differ only in their locations relative to the CDW. Note that numerous previous studies [Yaz+97; Ji+08; Rub+15b; Rub+16; Cho+17; Cor+17; Kam+18] on other substrates show that, in the absence of CDW ordering, YSR spectra and wave functions are fully reproducible for a particular adsorption configuration of the adatom on the substrate.

A Fe adatom can stably adsorb into two inequivalent positions with respect to the atomic lattice. These two positions exhibit different apparent heights (Fig. 5.1c,d). By atomic-resolution imaging, one can assign adatoms with small and large apparent height to adsorption in the two inequivalent hollow sites of the terminating Se layer, identified as hollow-centered (HC) and metal-centered (MC) sites, respectively (Fig. 5.1b). Differential conductance ($\mathrm{d}I/\mathrm{d}V$) spectra taken above the centers of HC and MC adatoms (blue and orange in Fig. 5.1e) show several YSR states inside the superconducting gap as well as in the energy range of the substrate's coherence peaks as observed previously for buried impurities [Sen+19]. The energy and intensity of the YSR states differ between the two species. Presumably, the splitting of the adatom d-levels is sensitive to the different local environments of the adsorption sites, which in turn affects the potential- and exchange-scattering strengths [Rub+16].

5.3.2 EFFECTS OF THE CDW ON THE YSR STATES

To study the influence of the CDW, the experiment focused on Fe atoms sitting in the same atomic adsorption site (HC). Six different atoms (labeled by I-VI) are shown in Fig. 5.2a. The adatoms differ in their position with respect to the CDW as is shown more clearly in Fig. 5.2d. The corresponding $\mathrm{d}I/\mathrm{d}V$ spectra (Fig. 5.2b) reveal that the energy and intensity of their YSR states differ strongly even though their atomic adsorption sites are identical with respect to the unperturbed lattice.

YSR states in the energy range of the superconducting coherence peaks are difficult to disentangle from the background. To avoid this complication, the experiment focused on deep-lying YSR states, specifically the two lowest YSR pairs labeled as $\pm\alpha$ and $\pm\beta$ in the close-up view of Fig. 5.2c.

i) EFFECTS ON THE WAVE FUNCTIONS

The wave function shape of an YSR state can be accessed by recording $\mathrm{d}I/\mathrm{d}V$ maps at its corresponding bias voltage. Such maps for the $+\alpha$ and $+\beta$ YSR states are shown in Fig. 5.3a for adatoms I-VI. The main panels show the extended patterns while the insets focus on the immediate vicinity of the adatom. All extended maps show patterns with oscillating intensity, which is in accordance with the expression of Eq. (3.9). The overall symmetries of the patterns clearly differ between adatoms I-VI.

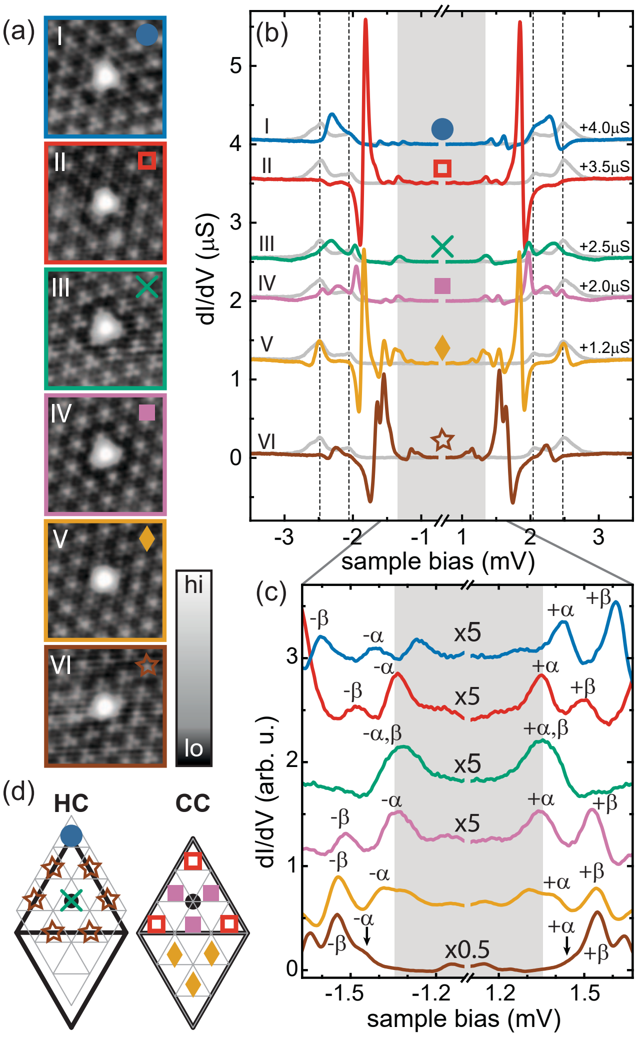

FIGURE 5.2: (a) STM maps (5×5 nm^2) of several HC Fe atoms labeled by I-VI. A non-linear color code is used to resolve the atomic background. (b) Spectra taken at the center of atoms I-VI (color) and on the substrate (grey). Spectra offset for clarity. (c) Close-ups of the spectra in (b). YSR resonances are labeled by $\pm\alpha, \pm\beta$. (d) Superimposed atomic (grey) and CDW lattices (black) for two CDW structures (HC and CC). The Se atoms are located at vertices of the atomic grids, so that the HC (MC) adsorption sites correspond to triangles pointing up (down). In the CDW lattice, vertices (dots) are maxima (minima) of the CDW. Colored symbols indicate the positions of atoms I-VI.

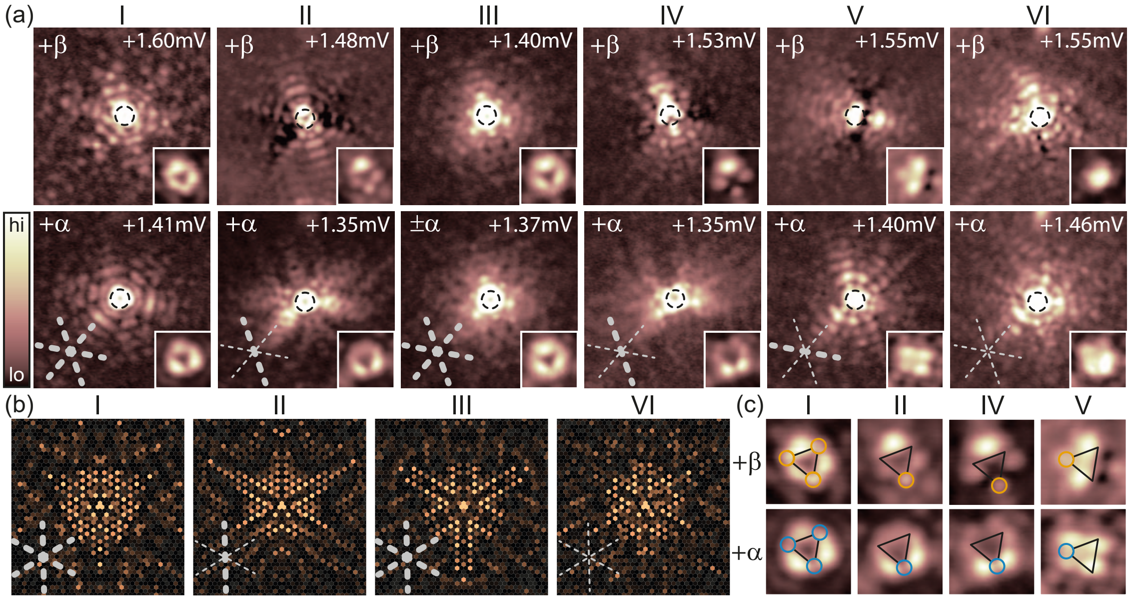

FIGURE 5.3: (a) STM maps ($9.5 \times 9.5\ \mathrm{nm}^2$) of the YSR ($\alpha, \beta$) states of HC atoms (I-VI). Black dashed circles (diameter $1\ \mathrm{nm}$) outline the adatoms' position. The insets show a $2 \times 2\ \mathrm{nm}^2$ close-up view around the center of the adatoms. (b) Numerical results for YSR states within a phenomenological description of the CDW (field of view: $40a \times 40a$ around adatom). Thick (thin) grey lines in the maps indicate presence (absence) of mirror axes. (c) Close-up view around the center of the adatoms I, II, IV, and V with superimposed triangles illustrating the presence (orange circles) and absence (blue circles) of intensity at their vertices. For adatom III, states α and β overlap. Adatom VI exhibits no symmetry.

The symmetry of the patterns associated with YSR states is expected to originate from the anisotropy of the Fermi surface through electron focusing [SBS97; FB97] and the local crystal field felt by the adatom [Rub+16]. The sixfold symmetry of the Fermi surface together with the threefold-symmetric atomic adsorption site should therefore lead to D_3 symmetry (threefold rotation as well as three mirror axes, indicated by dashed lines in Fig. 5.1b). Indeed, this D_3 symmetry is observed for both YSR states α and β of adatoms I and III, which reside at a maximum and a minimum of the CDW, respectively (Figs. 5.2d, 5.3a). However, this symmetry is lost in both, the long-range and the immediate vicinity of the adatoms for the other atoms shown in Fig. 5.3a. For adatoms II, IV, and V, the symmetry is reduced to D_1 symmetry (single mirror axis) while no symmetry axis can be discerned for adatom VI.

The symmetry reductions of the YSR wave functions coincide with the reductions of the local symmetry of the adsorption sites by the CDW (Fig. 5.2d). Adatom I (III) is positioned at a maximum (minimum) of the CDW. In this case, the CDW respects the atomic D_3 symmetry (HC structure of the CDW). Atoms II, IV, and V are located on one of the three equivalent symmetry axes connecting the high-symmetry positions, but unlike adatoms I and III do not fall on an extremum (CDW in the CC domain). Thus, the CDW breaks the atomic D_3 symmetry, leaving only D_1 symmetry consistent with the observed YSR wave functions. Finally, the position of adatom VI is totally asymmetric with respect to the CDW, which is reflected in the absence of any symmetry in the corresponding $\mathrm{d}I/\mathrm{d}V$ maps.

In Section 5.4, we show how the microscopic physics behind these symmetry

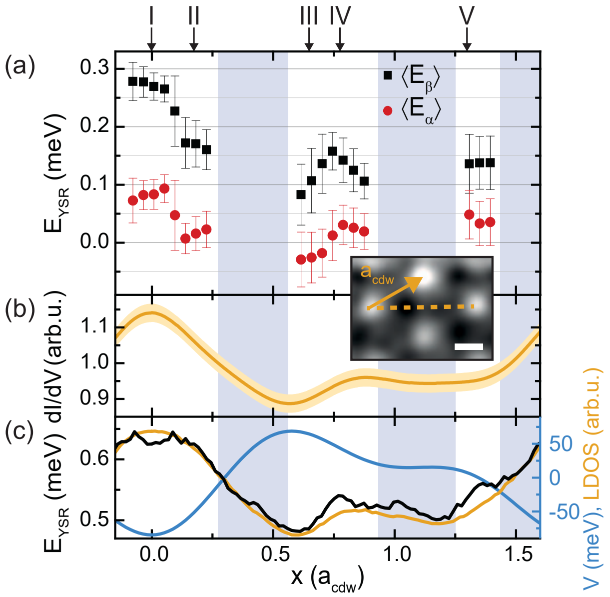

FIGURE 5.4: (a) Energy of the α-,β-YSR states as a function of their position relative to the CDW. Displayed points are obtained from averaging the energies of various atoms within intervals of $x \pm 0.05\,\mathrm{a_{cdw}}$. (b) Linecut along the orange-dashed line through a FFT-filtered constant-height $\mathrm{d}I/\mathrm{d}V$ map taken above T_c shown in the inset representing the variation of the local DOS. (c) CDW potential (blue), local DOS (orange) and YSR energies (black) obtained from the theoretical model for $JS = 360meV, i.e.$ in the strong-coupling regime.

reductions can be understood theoretically within a phenomenological mean-field description of the CDW combined with a tight-binding model of the $2H$-NbSe$_2$ band structure. Corresponding numerical results are shown in Fig. 5.3b for a subset of the adsorption sites investigated experimentally. Our numerical calculations show the same symmetry patterns for the equivalent adatom positions.

ii) EFFECTS ON THE ENERGIES

Analyzing the short-range patterns of the YSR states it is possible to track which YSR signature corresponded to α or β as a function of the position relative to the CDW. The key point here is that the β YSR state exhibits intensity (conductance) at the vertices of the triangles overlaid on its short range patterns (see Fig. 5.3c). On the contrary, the α YSR state exhibits pronounced nodes.

Using this distinction, the energies of both YSR states were tracked as a function of position relative to the CDW. Due to the small incommensurability of the CDW and substrate one can obtain data for numerous positions along its symmetry axis, like for positions I to V and also other in between. Approximately 90 adatoms adsorbed close to one of the three equivalent CDW symmetry axes were studied, combining data from several samples and Pb tips.

Figure 5.4a plots the average of the energies of both the α and β states as a function of adatom position along a high-symmetry axis of the CDW. Here, it was assumed that the energy dependences of both resonances follow the same trend which implies that the energy of the α resonance changes sign and crosses the quantum phase transition [Cho+17; FSP11; Far+18; Mal+18] as a function of adatom position. It is not possible to obtain data in the shaded regions in Fig.

5.4a. These regions correspond to the energetically unfavorable configuration of the CDW having a maxima above a Nb atom (MC).

The energies of the α and β YSR states are correlated with the local density of states. Fig. 5.4b shows the local density of states at the Fermi level induced by the CDW. The data is obtained through a constant-height $\mathrm{d}I/\mathrm{d}V$ map at zero bias above T_c along the symmetry axes (dashed line) shown in the inset. After removing the atomic corrugation with a FFT filter, the remaining signal is the local density of states induced by the CDW. The correlation of the energies with the local density of states can be understood from the expression of the energy of a YSR state for a simple model of Eq. (3.7). If the exchange coupling JS is larger than the scattering potential K, the YSR state energy can cross zero energy and enter the screened spin state. In this situation, an increase in the local density of states leads to an increase in the energy of the YSR state in absolute terms. Thus, experimentally one finds that the iron adatoms are in the screened spin state.

A qualitatively similar dependence of the energy of the YSR states is found in the model calculations presented below. For better comparison with the experimental data, Fig. 5.4c shows numerical data of the CDW potential, local density of states, and YSR energy along the equivalent symmetry axis. Our model reproduces a similar local density of states behavior induced by the CDW and a YSR state energy correlated with it. In the next Sections, we introduce our theoretical modeling and numerical results that explain the experimental data of this Section.

5.4 TIGHT-BINDING MODEL

In this Section, we introduce the theoretical model of $\mathrm{NbSe_2}$ and the magnetic adatom on its surface. In spite of the simplicity of the model and its shortcomings the numerical results of the model explain the experimental findings satisfactorily.

Our theoretical model foregoes a realistic description of the Fe d-orbital physics. We model the adatom as a classical impurity with isotropic potential and exchange couplings to the substrate. The wave functions (and the number) of the YSR states are quite sensitive to details of the band structure and the neglected d-orbital physics, so that one expects agreement only for qualitative aspects of symmetry. As explained in Section 5.2.3.i, due to the electron-phonon interaction, the CDW acts on the electrons as a weakly incommensurate, static periodic potential. In our model, this potential reduces the symmetry of the YSR wave functions in a manner consistent with the experimental results.

5.4.1 MODEL FOR THE BAND STRUCTURE

To illustrate the effect of the CDW on the YSR state wave function, we perform model calculations within an effective tight-binding description. Specifically, we implement a model for the $\mathrm{NbSe_2}$ band structure first introduced in Ref. [SKD85] and later used in Refs. [Ros+05; Ino+08; Ino+09; Rah+12; Mén+15]. The model uses that the relevant states near the Fermi energy have mostly Nb character and therefore focuses on one atomic d-orbital per niobium atom. (The model neglects an additional band centered at the Γ point which predominantly derives from Se orbitals and has strongly three-dimensional character [Baw+16].) Reducing the band-structure problem to the triangular Nb lattice

	t_0	t_1	t_2	t_3	t_4	t_5
band 1	10.9	86.8	139.9	29.6	3.5	3.3
band 2	203.0	46.0	257.5	4.4	-15.0	6.0

TABLE 5.1: Values of the fitting parameters t_n in Eq. (5.11) in meV.

makes it necessary to include hopping up to fifth nearest neighbors to reproduce the NbSe$_2$ band structure. The resulting band structure

$$\begin{aligned} E(\mathbf{k}) = t_0 + & t_1(2\cos\xi\cos\eta + \cos 2\xi) \\ & + t_2(2\cos 3\xi\cos\eta + \cos 2\eta) \\ & + t_3(2\cos 2\xi\cos 2\eta + \cos 4\xi) \\ & + t_4(\cos\xi\cos 3\eta + \cos 5\xi\cos\eta + \cos 4\xi\cos 2\eta) \\ & + t_5(2\cos 3\xi\cos 3\eta + \cos 6\xi) \end{aligned} \tag{5.11}$$

is sixfold symmetric about the Γ point. Here, we defined $\xi = k_x/2$ and $\eta = \sqrt{3}k_y/2$. The hopping strengths t_n are used as fitting parameters to reproduce the NbSe$_2$ band structure. The values of the parameters t_n are given in Table 5.1 [Rah+12] for the two bands. The parameters for band 1 reproduce the inner cylindrical bands of NbSe$_2$, while the parameters for band 2 reproduce the outer bands. Figure 5.5a shows the Fermi surfaces of the two bands, with the Brillouin zone outlined in gray.

While this model accounts for the symmetries of the band structure and the approximate shapes of the Fermi surfaces, it is limited in other ways. It neglects interlayer couplings, effectively resulting in a purely two-dimensional model. $2H$-NbSe$_2$ is a quasi-two-dimensional material whose interlayer couplings are expected to be weak compared to the intralayer ones. Together with the fact that the adatom predominantly couples to the outermost trilayer, it should suffice to consider only a single NbSe$_2$ monolayer. The model also neglects the significant spin-orbit interactions in monolayer NbSe$_2$ [Xi+16]. This precludes a one-to-one identification of the two sets of bands in Fig. 5.5a with specific spin directions. Following Ref. [Mén+15], we model the system either by band 1 or band 2, taking these bands as spin degenerate.

Superconductivity is included by incorporating the tight-binding Hamiltonian into a Bogoliubov-de Gennes Hamiltonian with conventional (isotropic) s-wave pairing. We choose the pairing strength to be $\Delta = 1\,\text{meV}$. In experiment, one finds multiple coherence peaks for $2H$-NbSe$_2$. Since we focus on YSR states far from the gap edge, we choose a representative value for Δ which falls into the range of the peak distribution ($0.7 - 1.4\,\text{meV}$) found in experiment.

The multiple coherence peaks originate from multiband or anisotropic superconductivity, or both. Our modeling does not account for these effects. In principle, an anisotropic gap function affects the wave function patterns of the YSR states. However, the (observable) spatial extent of YSR states is smaller than the coherence length through which effects of the pairing function would enter. We thus expect that the effect of an anisotropic pairing function on the YSR wave functions is weak and therefore account for superconductivity via an isotropic pairing function.

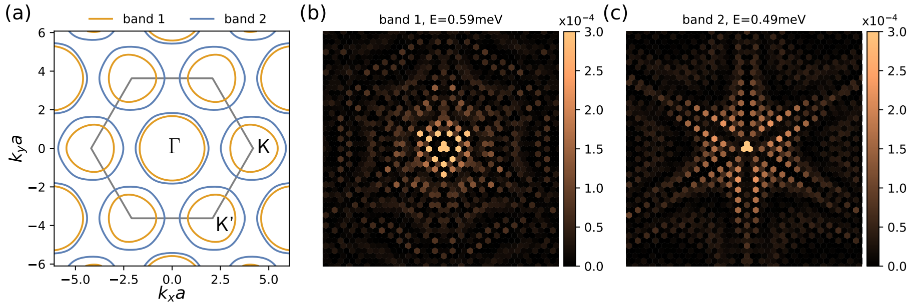

FIGURE 5.5: (a) Fermi surfaces of bands 1 and 2 (see Eq. (5.11) and Table 5.1). (b), (c): Electronic probability density $|u(\mathbf{r})|^2$ of the YSR state in the absence of the CDW for $JS = 120\,\text{meV}$, $K = 0$ and a lattice of size 504×504 with periodic boundary conditions for band 1 (b) and band 2 (c). The region shown includes 40×40 lattice spacings.

5.4.2 COUPLING TO THE MAGNETIC IMPURITY

We model a magnetic impurity as a classical spin S which interacts with the substrate electrons through the exchange interaction $JS\sigma_z$ and accompanying potential scattering K. In our experiment, we focus on magnetic impurities located above the center of a Nb triangle (hollow-centered, see Fig. 5.1b). The impurity induces not only separate exchange and potential couplings to its three neighbors, but also nonlocal exchange couplings which scatter electrons between the three sites via the impurity. It is essential to retain the latter to ensure that the impurity induces only one pair of YSR resonances. If we assume identical hopping amplitudes between the three sites and the impurity and assume that the impurity spin is aligned along the z-direction, we obtain the exchange coupling

$$\mathcal{H}_{\text{exch}} = -\frac{JS}{3}\sum_{i,j}\sum_{s,s'} c^\dagger_{is}\sigma^z_{ss'}c_{js'} \tag{5.12}$$

and potential scattering terms

$$\mathcal{H}_{\text{pot}} = \frac{K}{3}\sum_{i,j}\sum_{s} c^\dagger_{is}c_{js}. \tag{5.13}$$

Here, the sums over i and j run over the three nearest-neighbor Nb sites of the impurity, σ^z denotes a Pauli matrix, and c_{is} annihilates an electron on site i with spin s.

Figures 5.5b and c show the probability densities of the YSR states for (a spin-degenerate version of) bands 1 and 2, respectively, for a specific choice of impurity parameters. The spatial distribution of the probability density is threefold symmetric in both cases. Due to the more isotropic character of band 1, the corresponding YSR state is also more spatially isotropic than its band 2 counterpart, which exhibits a more pronounced anisotropy. In a more realistic modeling including the effects of spin-orbit coupling on the band structure (but within the approximation that the impurity is coupled only to a single trilayer), the YSR states would be simultaneously coupled to spin-textured, but polarized versions of both bands. While this implies that our results for the YSR wave functions are only qualitative, the symmetry of the YSR wave functions should not be affected by this approximation. Similarly, we expect that the qualitative variation of the YSR energies with the location of the adsorption site relative to the CDW would also be unaffected.

In the experiment one observes several YSR states for a single impurity. As our model neglects the complicated d-orbital physics and models the impurity as a classical spin, we obtain a single pair of YSR states per magnetic impurity. This would also be the case when considering a magnetic impurity coupled simultaneously to two bands. Indeed, if we write the matrix of exchange couplings J_{ij} between two bands i and j, it rather robustly satisfies the relation $J_{ii}J_{jj} = J_{ij}J_{ji}$. With this relation, a classical magnetic impurity generates only a single pair of YSR states. For instance, this was shown explicitly for a generic model motivated by the multiband superconductor $\mathrm{MgB_2}$ [Moc+08] and for a quantum dot coupled to multiple superconducting leads [Kir+15]. This conclusion would remain valid even when spin-orbit splitting of the bands was taken into account. This can be seen by expressing the Hamiltonian in terms of creation and annihilation operators for Kramers pairs of electron states rather than conventional spin states.

5.4.3 COUPLING TO THE CHARGE-DENSITY WAVE

As explained above, the effect of the CDW on the electrons of the substrate can be described through a periodic potential. Within the tight-binding model, we include the CDW as a modulation of the on-site potential,

$$\mathcal{H}_{\mathrm{cdw}} = \sum_{\mathbf{r},\sigma} c^{\dagger}_{\mathbf{r}\sigma} V(\mathbf{r}) c_{\mathbf{r}\sigma}, \tag{5.14}$$

where the sum runs over the lattice sites of the triangular Nb lattice. The CDW potential $V(\mathbf{r})$ is constructed from the main Fourier components of the CDW as shown in Eqs. (5.9) and (5.10).

Due to the small deviations from commensurability, the CDW shifts slowly as a function of position relative to the underlying atomic lattice. On the scale of the YSR states, these shifts can be considered constant so that the CDW potential can be written as

$$V(\mathbf{r}) = V_0 \left[2\cos\left(\sqrt{3}\frac{q}{2}(x-x_0)\right)\cos\left(\frac{q}{2}(y-y_0)\right) + \cos\left(q(y-y_0)+\phi_3\right)\right], \tag{5.15}$$

where $q = 4\pi/3\sqrt{3}$. The offsets x_0 and y_0 originate from the deviation δ from commensurability, and describe the local shift of the CDW relative to the atomic lattice. In the experiment, the measured maxima of the CDW correspond to regions where the lattice deformation compresses the ions, creating an attractive potential for the electrons. For this reason, we choose the potential $V(\mathbf{r})$ to have minima where the measured tunneling density of states has maxima, i.e., position I of the adatom corresponds to a minimum of $V(\mathbf{r})$ and position III corresponds to a maximum. In principle, the CDW may also modulate the hopping parameters of the tight-binding model, but the effective long-range hopping processes of the model make this cumbersome to include.

5.5 NUMERICAL RESULTS

Within the model presented in the previous Section, we study how the wave function and the energy of YSR states depend on the adatom position relative to the CDW. As discussed above, the model cannot reproduce the experimental results quantitatively as it neglects various relevant effects. Nevertheless, the model is expected to capture the symmetries of the YSR wave functions and

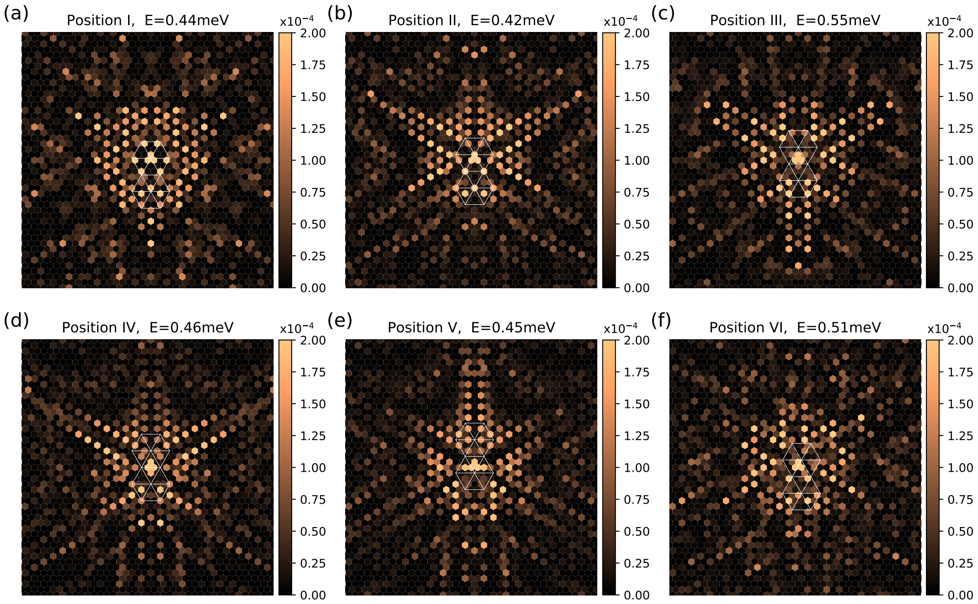

FIGURE 5.6: Electronic probability density $|u(\mathbf{r})|^2$ of the YSR state in the presence of the CDW potential for band 2 and for adatoms located at positions equivalent to those studied experimentally (see Fig. 5.2). For all plots, the parameters are $JS = 120\,\mathrm{meV}$, $K = 0$, $V_0 = -30\,\mathrm{meV}$, $\phi = \pi/3$ and a lattice of size 504×504 with periodic boundary conditions. The region shown includes 40×40 lattice spacings. The white lines outline the CDW, with crossing lines indicating a maximum of the CDW.

to provide insights into the qualitative dependence of the YSR energy on the adsorption site relative to the CDW.

5.5.1 EFFECT OF THE CDW ON THE YSR WAVE FUNCTIONS

Figure 5.6 shows the probability density of the YSR wave function for the six different positions of the adatom relative to the CDW studied in the experiment. The results are obtained for the parameters of band 2. The adatoms in positions I and III are at the maximum and the minimum of the CDW, respectively, i.e., at points with a threefold symmetric environment. Consequently, the corresponding density plots (Fig. 5.6a and c) exhibit threefold symmetry. Positions II, IV, and V exhibit reflection symmetry about an axis that passes through the adatom. For the corresponding plots shown in Fig. 5.6b, d, and e, this axis is aligned along the vertical direction. Finally, position VI has no symmetries with respect to the CDW and consequently, the state shown in Fig. 5.6f also exhibits no symmetries. Interestingly, the YSR state seems to retain the original threefold symmetry (without CDW) to some degree (compare with Fig. 5.5c).

Figure 5.7 shows equivalent plots for band 1. Due to the more isotropic character of band 1, the threefold symmetry is less pronounced in these plots. Remarkably, position VI (Fig. 5.7f) does not preserve any of the original threefold symmetry in the vicinity of the adatom. More generally, a comparison between Figs. 5.6 and 5.7 shows that the detailed YSR wave functions depend quite sensitively on the band structure parameters.

It is worth noting that the effects of the CDW on the symmetry of the YSR wave functions is reproduced within our model (compare with Fig. 5.3) in spite

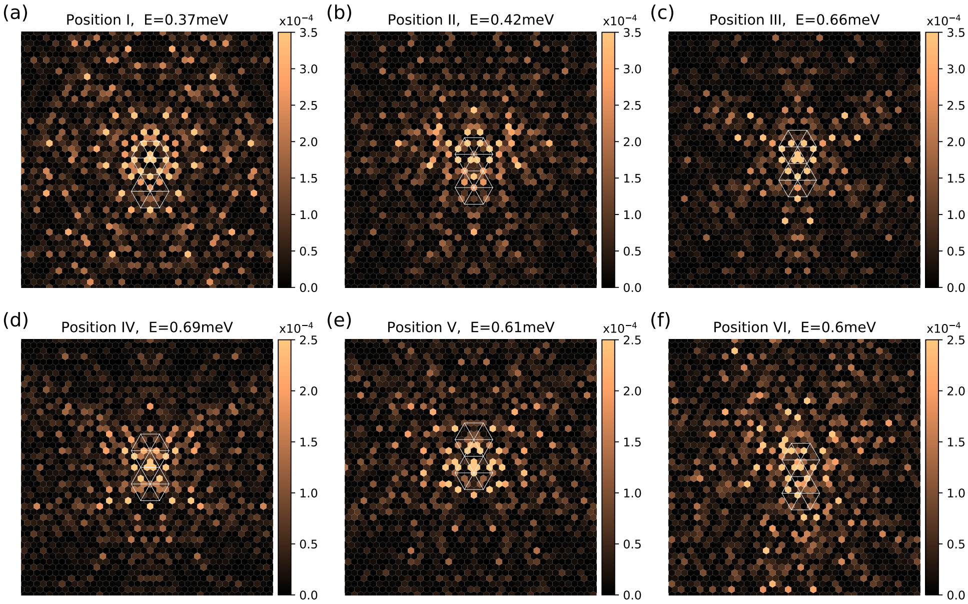

FIGURE 5.7: Analogous plots to those in Fig. 5.6 for band 1. Parameters: $JS = 120\,\mathrm{meV}$, $K = 0$, $V_0 = -30\,\mathrm{meV}$, $\phi = \pi/3$ and a lattice of size 504×504 with periodic boundary conditions. The region shown includes 40×40 lattice spacings.

of neglecting various relevant effects present in the experimental setting. This indicates that the Fermi surface and the CDW suffice to explain these phenomena and that our results can be extended to other materials in which the superconductivity coexists with a charge density wave.

5.5.2 EFFECT ON THE YSR ENERGIES

Finally, we discuss the correlation of the energy of the YSR state with the modulation of the local density of states induced by the CDW, explaining the experimental data shown in Fig. 5.4. As explained in Chapter 3, a simple model of a classical magnetic impurity leads to a YSR pair of states with energy given by:

$$E_{\text{YSR}} = \pm\Delta \frac{1-\gamma^2+\kappa^2}{\sqrt{4\gamma^2+(1-\gamma^2+\kappa^2)^2}}, \tag{5.16}$$

where $\gamma = \pi\nu_0 JS$ and $\kappa = \pi\nu_0 K$. The experiment finds that one of the YSR resonances crosses zero energy as a function of its position relative to the CDW. Note that Eq. (5.16) can only be zero if $\gamma > \kappa$. It is instructive to consider Eq. (5.16) in the limiting case of $\kappa = 0$:

$$E_{\text{YSR}} = \pm\Delta \frac{1-\gamma^2}{1+\gamma^2}. \tag{5.17}$$

From this expression the effect of a change in the density of states ν_0 on the energy becomes more transparent. The direction of the energy shift of the positive energy state depends on which side of the quantum phase transition the system is in, i.e., on whether the impurity is weakly or strongly coupled. For a weakly (strongly) coupled impurity, an increase in the density of states, i.e., an increase in γ, leads to a decrease (increase) in the energy of the positive YSR

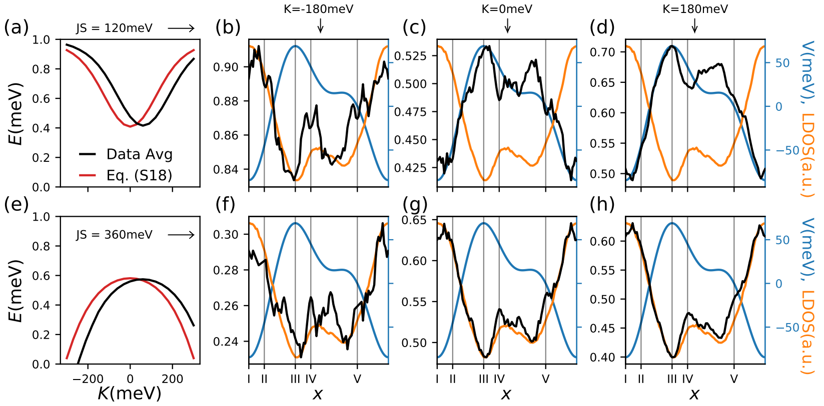

FIGURE 5.8: Tight-binding calculations for the energy of the YSR state as a function of the position of the adatom relative to the CDW, for various potential scattering strengths K. Panels (a) and (e) show the energy of the YSR state E vs. K for the weakly and strongly coupled regimes, respectively [as obtained by averaging over different positions of the adatom relative to the CDW (black) and as given by Eq. (5.16) for an appropriately chosen ν_0 (red)]. Panels (b)-(d) show E vs. adatom position in the weakly coupled regime for three different K. The plots show the local density of states (LDOS, orange) to anticorrelate with the CDW potential V (blue). Panels (c) and (d) show the energy to correlate with the CDW potential V (anticorrelate with the LDOS). For $K = -180\,\text{meV}$ shown in panel (b) the correlation inverts due to the shift of K to $K + V(\mathbf{r}_0)$ (see main text). Panels (f)-(h) show equivalent plots for the strongly coupled regime, where the K-shift effect is less relevant. The energy E is correlated with the LDOS as expected from Eq. (3.7). For all plots, the parameters are $V_0 = -30\,\text{meV}$, $\phi = \pi/3$, and a lattice size of 750×750.

state. Based on this picture, the experiment suggests that the impurity is in the strongly coupled regime.

This interpretation is consistent with our theoretical results. However, we find that in general the CDW affects the energy of the YSR state through two mechanisms. In addition to the density-of-states effect, the CDW potential has a second effect which can be rationalized as the CDW affecting the strength of potential scattering from the impurity and thereby shifting the YSR energy. Roughly, the CDW potential V seems to shift K to $K + V(\mathbf{r}_0)$, where $\mathbf{r}_0$ denotes the adsorption site of the impurity.

To illustrate these two effects of the CDW potential, we calculate the YRS energy for different adatom positions and various values of K. Figure 5.8 shows numerical results of the YSR energy dependence on the position relative to the CDW. First we would like to point out that panels (b) to (d) and (f) to (h) show the same CDW potential (blue line) as given by Eq. (5.10) along the path equivalent to the dashed line in the inset of Fig. 5.4b. These panels also show the local density of states (LDOS, orange line) as obtained from a band structure calculation including the CDW. Minima (maxima) of the CDW potential correspond to maxima (minima) in the LDOS, i.e., they are anticorrelated. The value of the LDOS varies by 7% between its minimum and maximum (not visible in the plots for the sake of presentation).

Consider first the results for weak coupling (first row of panels in Fig. 5.8). Fig. 5.8a shows the dependence of the energy of the YSR state on K in the weak-coupling regime. The black curve averages data for the energy of the YSR state over the six different adatom positions. The red curve corresponds to Eq. (5.16) with the same values for JS and K and an appropriately chosen density of states ν_0. Both curves exhibit similar 'parabolic' behaviors, with the black curved shifted to a positive K value. Fig. 5.8c shows the dependence of the YSR energy (black) on the position relative to the CDW for $K = 0$. At this K, the K-shift effect is weak, as this case corresponds to being close to the bottom of the parabola of panel (a). The behavior of the energy can be understood from Eq. (5.17). Indeed, panel (c) shows that an increase in the LDOS leads to a decrease in the YSR energy, i.e., they are anticorrelated. Fig. 5.8d shows a similar plot for $K = 180$meV. In this case, the K-shift effect is in the positive slope region of the parabola in panel (a). Thus, a shift of K to $K + V(\mathbf{r}_0)$ increases (decreases) the energy for positive (negative) $V(\mathbf{r}_0)$. For this reason, both effects contribute in the same direction to the YSR energy change and one finds the YSR energy correlated with the CDW potential and anticorrelated with the LDOS.

There is a change of behavior for $K = -180$meV, case shown in panel (b). For this K, the K-shift effect is in the negative slope region of the parabola in panel (a) and it overcomes the LDOS effect on the energy. This leads to a YSR energy anticorrelated with the CDW potential and correlated with the LDOS, as opposed to the cases of panels (c) and (d).

For the strongly coupled regime (second row of panels in Fig. 5.8), we find that the YSR energy and the CDW potential are anticorrelated – and thus correlated with the LDOS – for all values of K, see Fig. 5.8f,g and h. These correlations between the density of states and the YSR energy are consistent with experiment. To start with, the anticorrelations at $K = 0$ are consistent with the expected density-of-states effect according to Eq. (5.17). For strong coupling, the dependence of the YSR energy on K is generally weaker compared to the weak coupling case, see Fig. 5.8e. For this reason, the shift of K by the CDW potential no longer overcomes the density-of-states effect.

Our theoretical analysis indicates that the adatoms in the experiment are in the strongly coupled regime. It is in this regime where the YSR energies are correlated with the changes in the local density of states induced by the CDW. Such a correlation is also possible in the weakly coupled regime, albeit for a strong scattering potential for which it is not possible to find YSR energies in the vicinity of zero. Our experiment and theoretical analysis provide a novel method to identify on which side of the quantum phase transition a magnetic impurity finds itself. This method requires knowledge about the band structure of the material and a charge density wave modulation that changes the local density of states at the impurity. Thus, our method might be applied to adatoms and materials other than iron and NbSe$_2$.

5.6 CONCLUSION

This Chapter, based on Ref. [Lie+19], presents the experimental findings of the effects of a charge density wave on the wave functions and energies of Yu-Shiba-Rusinov states are explained within a simple theoretical model. We show that, despite the complexity and different effects present in the experiment (d-orbital physics, anisotropic superconductivity, spin-orbit interaction, etc), its results are qualitatively reproduced in a model that accounts for the symmetry of the bands of $2H$-NbSe$_2$ at the Fermi energy and that includes the charge density wave as an electrostatic potential.

The charge density wave modulation affects the symmetry of the YSR wave functions depending on the position of the adatom relative to it. Thus, a YSR wave function in $2H$-NbSe$_2$ can exhibit three-fold symmetry, mirror symmetry along one axis, or no symmetry at all. Similarly, the energy of the YSR states is also affected by the CDW modulation. We find that this occurs through two mechanisms. First, the CDW changes the local density of states, which influences both the exchange and potential scattering coupling of the magnetic adatom. And second, the CDW potential shifts the potential scattering. Thanks to our study it is possible to identify that the iron adatoms on $2H$-$\mathrm{NbSe_2}$ are in the strongly coupled regime (screened spin state). We would like to note that this is a novel method to determine on which side of the quantum phase transition (unscreened or screened spin) a magnetic adatom is. This method could be applied to other substrates where superconductivity coexists with a charge-density-modulated phase.

Our findings are of relevance in the context of the engineering of topological phases. $\mathrm{NbSe_2}$ has attracted attention as a stable and reliable substrate on which to build chains of magnetic adatoms. For the adatoms of such a chain to couple as desired, one needs to take into account our findings. Namely, the adatoms have to be positioned such that the YSR wave functions overlap and that the energies of the isolated YSR states are similar. It is thus necessary to place the adatoms of the chain within the CDW accordingly.

6 | PHOTON-ASSISTED RESONANT ANDREEV REFLECTIONS: BEYOND SIMPLE TIEN-GORDON THEORY

6.1 INTRODUCTION

Tunneling across superconducting junctions can take place through a variety of processes involving single-electron transfer, two-electron (Cooper pair) transfer, or even higher numbers of electrons in multiple Andreev reflections. In the presence of radiation, the widely successful Tien-Gordon theory has been implemented in many contexts to identify the tunneling processes across superconducting junctions. A recent experiment [Pet+20] showed that, while it correctly predicts the conductance across a junction composed of bare superconductors, it breaks down for resonant tunneling via subgap states at sufficiently high junction conductances. In this Chapter[1], we present the results of this experiment and give a phenomenological explanation, leaving the more systematic analysis for Chapter 7, where we also make the connection to topological state engineering.

At subgap temperatures and voltages, charge transfer between conventional superconductors typically occurs by multi-electron processes. The transfer of Cooper pairs is responsible for Josephson currents flowing between superconductors [Jos62] and leaves the superconductors in their ground state. Cooper pairs can also be extracted from, injected into, or transferred between superconductors with the simultaneous generation of quasiparticles [SW63; And64]. In these processes – termed multiple Andreev reflections – electrons impinging on one of the superconducting electrodes are reflected as holes, while a Cooper pair is transmitted into the superconductor. As a result, one or several Cooper pairs are transferred between the superconductors while generating a pair of quasiparticles [SW63].

At subgap voltages, single-electron transmission is possible only due to thermally excited quasiparticles. In tunnel junctions, these processes can compete with two-electron tunneling since the latter are of higher order in the tunneling amplitude and hence exponentially suppressed. As explained in Section 3.3, the interplay of single-electron and two-electron tunneling can be elucidated in scanning-tunneling-spectroscopy experiments where the junction resistance

---

[1] This Chapter is based on Ref. [Pet+20]. The author of this thesis collaborated in the analysis of the experimental data, the development of the theoretical framework, and provided numerical simulations. All the credit for the experimental results go to the experimental collaborators.

is readily changed by orders of magnitude, thereby tuning the relative importance of these two tunneling processes. The experiment [Rub+15b] studied this interplay for tunneling resonantly enhanced by a YSR state and found that the two-particle current dominates at high junction conductances. These resonant Andreev reflections transfer a Cooper pair between the superconductors while generating a pair of quasiparticles. The nature of these processes was further studied in Ref. [Pet+20] which aimed at distinguishing single-electron and two-electron tunneling through YSR states by means of photon-assisted tunneling in the presence of high-frequency (HF) radiation.

We begin the Chapter by introducing Tien-Gordon theory. Then, we present the experimental results on photon-assisted tunneling from a superconducting STM tip into a pristine superconducting substrate. For such a junction, Tien-Gordon theory correctly identifies single-electron tunneling both above and within the superconducting gap, as well as Cooper-pair tunneling and Andreev reflections at subgap voltages. We continue with the corresponding results for photon-assisted processes between superconductors through a YSR state. Here, the tunability of the junction conductance allows one to explore the regime where resonant Andreev reflections dominate the current. In this high-conductance regime, Tien-Gordons theory breaks down and fails to predict the shape of sidebands as well as the amount of charge transferred in the underlying tunneling process.

6.2 TIEN-GORDON THEORY

Photon-assisted tunneling constitutes a powerful method to probe the nature of charge transfer. The absorption and emission of photons leads to the appearance of sidebands in the conductance both in the absence [DM62; Roy+15] and in the presence [Kou+94; Bli+95; NT99; MEK07; GBS15; Zan+19] of Coulomb blockade. Frequently, the spacing of the sidebands in bias voltage as well as their modulation as a function of the amplitude of the HF radiation directly reveal the amount of charge that is transferred in an elementary tunneling event [PA04]. The theory of such processes goes back to the classic work of Tien and Gordon [TG63], and their early results on single-electron transfer between superconductors has been extended in multiple directions. In many situations, one finds Tien-Gordon-like relations

$$G(V) = \sum_n J_n^2 \left(\frac{keV_{\mathrm{HF}}}{\hbar\Omega} \right) G^{(0)}(V + n\hbar\Omega/ke), \tag{6.1}$$

which express the junction conductance $G(V) = \mathrm{d}I/\mathrm{d}V$ in the presence of HF radiation in terms of the junction conductance $G^{(0)}(V)$ without HF radiation. Here, k denotes the number of electrons transferred in an elementary tunneling event [FBS91], Ω is the frequency of the HF radiation, and V_{HF} its amplitude. The conductance is a sum over sidebands spaced in bias voltage by $\hbar\Omega/ke$, whose strength is controlled by the Bessel functions J_n. The oscillations of the Bessel functions as a function of their argument imply a characteristic modulation of the sideband intensity as a function of V_{HF}.

Relations like (6.1) have been shown to describe not only photon-assisted sidebands of the coherence peaks [TG63], but also incoherent Josephson tunneling near zero bias [FBS91] or multiple Andreev reflections [ZK96]. In the context of scanning-tunneling-microscopy (STM) experiments, these Tien-Gordon expressions are found to describe the sidebands of the coherence peaks [Pet+20;

Kot+20], the Josephson peak [Roy+15; Pet+20; Kot+20], as well as multiple Andreev peaks [Pet+20; Kot+20]. These relations can be understood from the tunneling Hamiltonian H_T. Measuring the energies in both electrodes from their respective chemical potentials (explained in the next Chapter, Section 7.3), the tunneling is found to carry a time-dependent phase factor

$$e^{-i\phi(\tau)} = e^{-i(\frac{eV}{\hbar}\tau + \frac{eV_{\mathrm{HF}}}{\hbar\Omega}\sin\Omega\tau)}, \tag{6.2}$$

which accounts for the change in energy of the tunneling electrons due to the voltage bias across the junction. The amplitude for transferring multiple electrons can be obtained from higher-order terms in the Born series for the T-matrix, $T = H_T + H_T G_0 H_T + \ldots$ While in general, the unperturbed Green function G_0 is nonlocal in time, it is effectively local on the scale of Ω^{-1} when the energy denominator of the virtual intermediate states is large compared to the energy transfer from the HF radiation. In this case, the factors of $e^{-i\phi(\tau)}$ from the different tunneling terms simply combine into a single factor $e^{-ik\phi(\tau)}$, and a Fermi golden rule calculation leads to Eq. (6.1). This argument applies to incoherent Cooper pair tunneling as well as multiple Andreev reflections for plain superconducting electrodes as long as $\hbar\Omega, eV_{\mathrm{HF}} \ll \Delta$.

This reasoning does not extend to resonant Andreev reflections via YSR states as the amplitude for tunneling is sharply peaked in energy due to the bound state. Indeed, the experiment performed in [Pet+20] shows that photon-assisted resonant Andreev reflections exhibit rich physics that is qualitatively different from the Tien-Gordon-like expression (6.1).

6.3 PHOTON-ASSISTED TUNNELING PROCESSES BETWEEN PRISTINE SUPERCONDUCTORS

The experiment implemented a high-frequency circuit into the STM setup with a cable terminating close to the STM-substrate junction acting as a HF antenna. The experiment used Pb, with a superconducting gap $\Delta_{\mathrm{Pb}} \approx 1.35$meV, for the coating of the STM tip and for the superconducting substrate, and a radiation frequency of $\Omega/2\pi$ =40GHz. In this Section, we review the different tunneling processes across a superconductor-superconductor junction and show the corresponding experimental results.

Single-electron tunneling between superconductors leaves behind an unpaired electron in the source and injects an unpaired electron into the drain. Each of these electrons requires a minimal excitation energy equal to the superconducting gap Δ (assumed equal for source and drain superconductors for simplicity). Thus, single-electron tunneling becomes possible at voltages $e|V| \geq 2\Delta$. The BCS singularity of the superconducting density of states leads to coherence peaks in the differential conductance at the threshold voltages $eV = \pm 2\Delta$. In the presence of an *ac* field with frequency Ω, the tunneling electrons not only gain energy eV due to the bias voltage, but can also emit or absorb photons. Then, the threshold condition for single-electron tunneling becomes $eV + n\hbar\Omega = \pm 2\Delta$, where the integer n is positive for photon absorption and negative for photon emission, and one obtains a set of coherence peaks displaced in voltage by multiples of the photon energy $\hbar\Omega/e$ [TG63; DM62]. The number of emitted or absorbed photons per tunneling event is bounded by the maximal energy eV_{HF} that the tunneling electrons can exchange with the *ac* field, where V_{HF} denotes the amplitude of the *ac* bias across the junction. This implies that

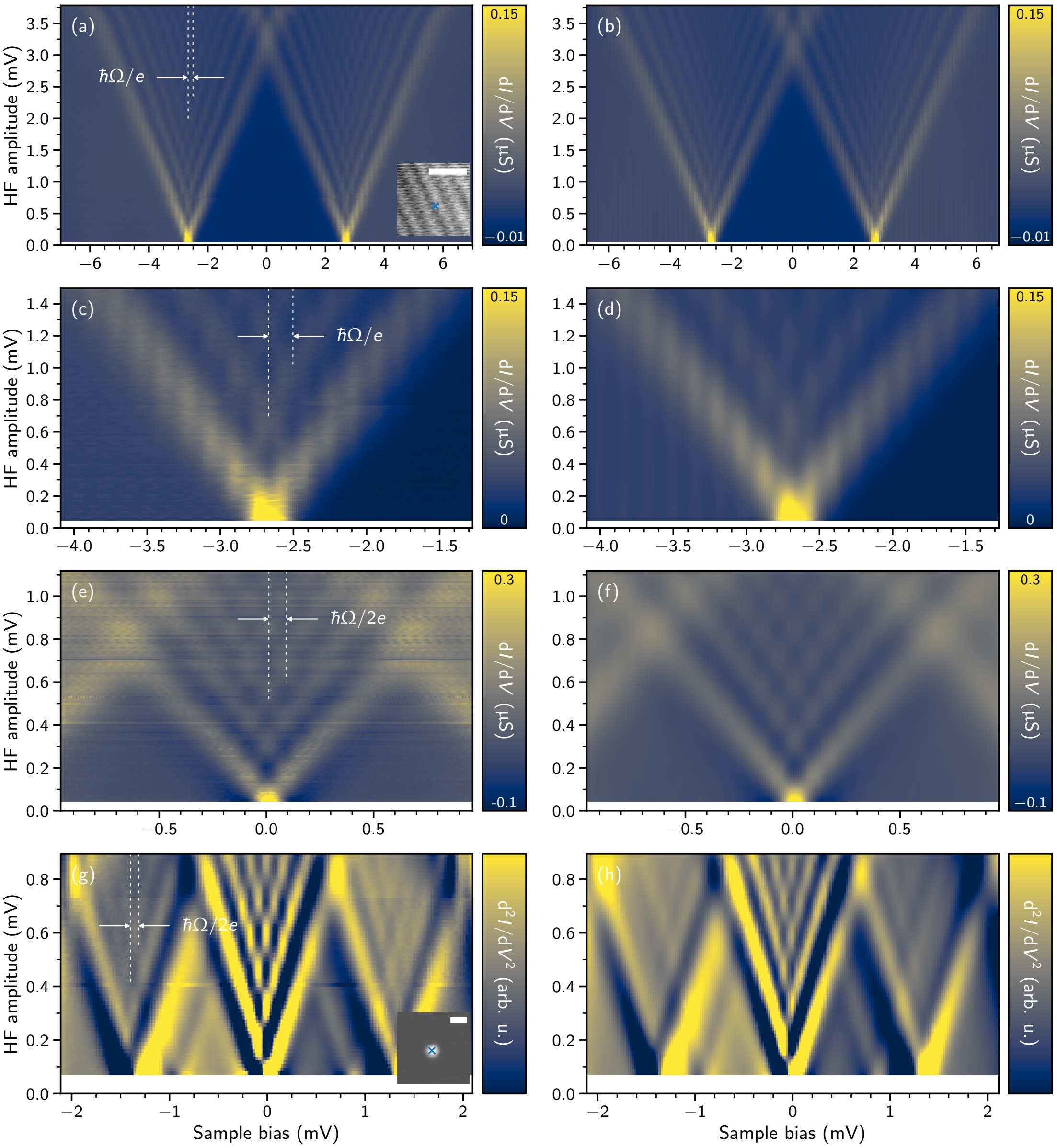

FIGURE 6.1: Experimental (left) and simulated (right) $\mathrm{d}I/\mathrm{d}V$ spectra in the presence of radiation. (a, b) V-shaped splitting of the BCS coherence peaks in a Pb–Pb junction. (c, d) Close-up view of the negative-bias V-shape at low radiation amplitudes. The sideband spacing in bias is equal to $\hbar\Omega/e$. (e, f) Splitting of the Josephson peak with sideband spacing of $\hbar\Omega/2e$, reflecting Cooper-pair tunneling. (g, h) $\mathrm{d}^2I/\mathrm{d}V^2$ spectra recorded on a Pb adatom showing the $m = 2$ multiple Andreev reflection sidebands at $eV = \pm\Delta$ split by $\hbar\Omega/2e$. Insets in (a) and (g) show STM images of the location where the spectra were recorded (indicated by a cross, scale bars equal $1\,\mathrm{nm}$). The simulations are based on the Tien-Gordon-like Eq. (6.1) with the corresponding V_{HF}, the experimental frequency $\Omega = 2\pi 40\,\mathrm{GHz}$, and $G^{(0)}(V)$ as the measured differential conductance in the absence of radiation, with $k = 1$ for the single-electron processes in (a) and (d) and $k = 2$ for the two-electron processes in (e) and (g).

coherence-peak sidebands are limited to $|n| \lesssim n_{\max} = eV_{\mathrm{HF}}/\hbar\Omega$ and thus observable in the voltage ranges $|eV \pm 2\Delta| \lesssim eV_{\mathrm{HF}}$. Indeed, the experiment shows sidebands that are clearly limited to these two voltage ranges, forming two V-shapes with vertices starting at $eV = \pm 2\Delta \sim \pm 2.7$meV (Fig. 6.1a). The radiation splits the sidebands in maxima separated by a measured $161(10)\mu$V, well in accordance with the predicted $\hbar\Omega/e = 165\mu$V for single-electron tunneling (see Fig. 6.1c for a close-up of the negative-energy low-HF-amplitude where the splitting is better appreciated). The Tien-Gordon approach, as embodied by Eq. (6.1), correctly reproduces these results (Figs. 6.1b and d) for the single-electron $k = 1$ case, using as input the measured conductance in the absence of radiation and the experimental parameters V_{HF} and Ω.

In the vicinity of zero bias, current flows between superconductors via Cooper pair tunneling. This leads to a zero-bias peak in the differential conductance, reflecting that Cooper pair tunneling does not excite either of the superconducting electrodes. The ac field splits this Josephson peak into sidebands. The Cooper pairs gain an energy $2eV$ due to the applied bias and $n\hbar\Omega$ due to the photon field. Thus, these sidebands occur at $eV = n\hbar\Omega/2$, exhibiting half the spacing in bias voltage compared to single-electron processes. The tunneling Cooper pairs change their energy at most by $2eV_{\mathrm{HF}}$ due to the ac field. Consequently, the Josephson peaks are limited to $|n| \lesssim n_{\max} = 2eV_{\mathrm{HF}}/\hbar\Omega$ and visible in the voltage range $|eV| \lesssim eV_{\mathrm{HF}}$ [NT99; NTD01; Roy+15; Pet+20; Kot+20]. The measurement of these sidebands is shown in Fig. 6.1e, for which a spacing of $82(5)\mu$V$\sim$ $\hbar\Omega/2e$ is found. This indicates that the charge transfer of the tunneling events corresponds to $k = 2$ electrons, as confirmed by the corresponding Tien-Gordon simulation in Fig. 6.1f.

Current can also flow at subgap voltages due to multiple Andreev reflections. Electrons with subgap energies impinging on the source or drain superconductor are reflected as holes, with a Cooper pair transferred into the superconductor (or vice versa). Then, the required excitation energy of 2Δ for the two generated quasiparticles can be acquired in the course of multiple traversals across the junction, and the threshold condition becomes $meV = 2\Delta$, where the (positive) integer m denotes the number of junction traversals and thus the number of electrons transmitted into the drain superconductor. In the presence of the ac field, photons can be emitted or absorbed in the tunneling process, and the threshold condition becomes $meV + n\hbar\Omega = 2\Delta$ [Cha+06]. The spacing of the photon sidebands in voltage is then given by $\hbar\Omega/me$ and directly reflects the number of transferred electrons per tunneling process. Specifically, the lowest multiple Andreev process with $m = 2$ has a threshold voltage of $eV = \Delta$ without ac field, transmits a Cooper pair into the drain, and has sidebands with the same voltage spacing of $\hbar\Omega/2e$ as for the Josephson peak [Cue+02; UW05; Pet+20; Kot+20]. The corresponding measurement in Fig. 6.1g, shows the second derivative of the current to enhance the contrast. Sidebands are observed at $eV = \pm\Delta$ with a splitting of $82(5)\mu$eV$\sim$ $\hbar\Omega/2$ corresponding again to an underlying two-electron process. The corresponding simulation using Eq. (6.1) reproduces the experimental results faithfully.

At nonzero temperatures, there are additional single-electron processes even at subgap voltages which originate from thermally excited quasiparticles. These processes (not measured in the experiment) lead to a peak in the differential conductance when the coherence peaks of the two superconductors align. This causes a zero-bias peak when source and drain have gaps of the same magnitude, and more generally a peak at $eV = \pm|\Delta_1 - \Delta_2|$, when the superconductors have different gaps [Ter+06; FSP11].

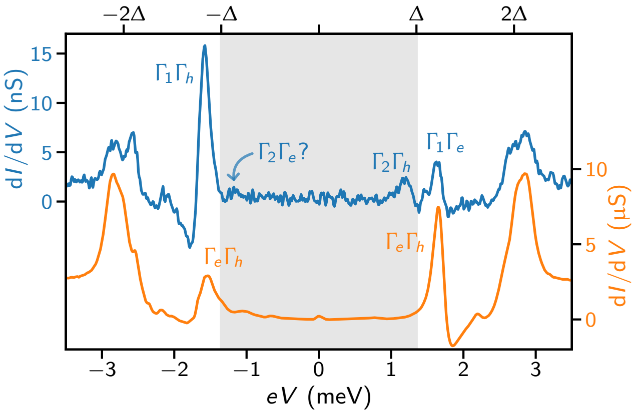

FIGURE 6.2: YSR spectra of an Mn adatom on top of superconducting Pb taken with a superconducting STM tip. At high junction resistances (blue line) the current is dominated by single-particle tunneling. The peaks of the lowest lying YSR state are identified with the corresponding rates involved. At low junction resistances (orange line) the current is dominated by resonant Andreev reflections. The tunneling rates dominate the broadening of the resonance leading to peaks of inverted height with respect to the high junction resistance case (see Section 3.3).

In conclusion, the experimental results for photon-assisted tunneling between pristine superconductors are well explained by Tien-Gordons theory, successfully predicting the sideband spacing as well as the modulation of the conductance as a function of the radiation amplitude. Next Section reveals that resonant Andreev processes via YSR states produce signatures that do not conform with Tien-Gordon theory.

6.4 PHOTON-ASSISTED TUNNELING PROCESSES VIA YSR STATES

The tunneling processes in a superconducting junction via a YSR state in the absence of radiation were explained in Section 3.3 in terms of the thermal excitation and relaxation rates Γ_1 and Γ_2, and the electron and hole tunneling rates Γ_e and Γ_h. We refer the reader to Section 3.3 as its content is of central importance for the present discussion. The experiment focused on the lowest-energy YSR resonance ($\epsilon_0 = 0.25$meV) found on a Mn adatom deposited on the Pb substrate. Figure 6.2 (shown in Chapter 3 and reproduced here for the sake of discussion) shows the conductance spectrum of the adatom in the absence of radiation for both low (blue) and high (orange) junction conductances. At low junction conductances single-electron processes dominate the current, $I \approx I_{\Gamma_1} + I_{\Gamma_2}$ (see Eqs. (3.19),(3.20)). These contributions lead to the four conductance peaks labeled in the blue line in Fig. 6.2 (note that the peak labeled as $\Gamma_2\Gamma_e$ is almost absent or barely distinguishable from the background noise). From this spectrum, the Tien-Gordon model predicts the formation of four different V-shapes of sidebands when measuring the differential conductance in the presence of radiation. The vertices of these V-shapes are expected to be located at the threshold voltages:

$$\begin{aligned} eV^{\text{th}}_{e\pm} &= \pm\Delta + \epsilon_0, \\ eV^{\text{th}}_{h\pm} &= \pm\Delta - \epsilon_0. \end{aligned} \tag{6.3}$$

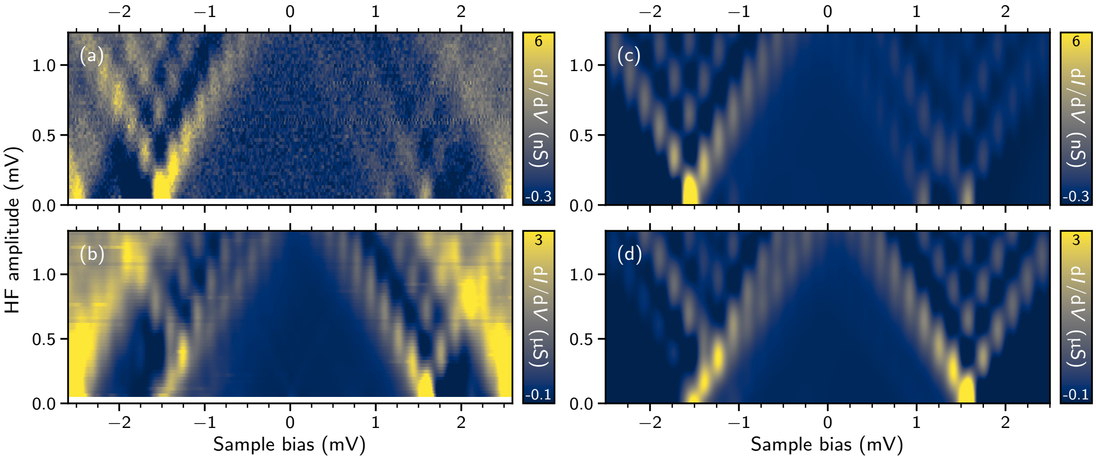

FIGURE 6.3: Differential conductance spectra of photon-assisted tunneling via a YSR state under HF irradiation. (a) At a low junction conductance, three V-shaped splittings stemming from the three YSR peaks in the absence of radiation (Fig. 6.2, blue) are visible. (b) At a high junction conductance, a V-shape is visible at positive bias while a Y-shape appears at negative bias, showing a double-peak structure along its low-bias arm. The sideband spacings correspond to $\hbar\Omega$, seemingly indicating single-electron tunneling. (c, d) Numerical simulations corresponding to the junction conductances in (a, b), based in the effective tunneling rates (6.4) and Eqs. (3.19)-(3.21). The parameters[2] are common to (c) and (d) except for the tunneling t across the junction.

This is indeed what the experiment measures, see Fig. 7.2a. Starting from the left, the first V-shape appears at the hole threshold $eV_{h_-}^{\mathrm{th}} = -\Delta - \epsilon_0$ and it is the most prominent one, as it derives from the highest peak in the blue spectrum in Fig. 6.2. The V-shape at the threshold $eV_{e_-}^{\mathrm{th}} = -\Delta + \epsilon_0$ is absent as it would stem from the barely visible peak labeled as $\Gamma_2\Gamma_e$ in Fig. 6.2. The other two V-shapes at positive voltages can also be appreciated, though faintly due to a small signal-to-noise ratio. Furthermore, the sideband spacing is found to be $\hbar\Omega$ as expected for single-electron tunneling. Thus, the Tien-Gordon approach does apply for the single-electron tunneling via a YSR state at low junction conductances. Before explaining this success, it is useful to understand why this approach fails to explain the measurement at high junction conductances, as is discussed in the following.

At high junction conductances, the current is dominated by resonant Andreev reflections similar to the $m = 2$ multiple Andreev reflections explained above. The high conductance spectrum in the absence of radiation exhibits two peaks at the threshold voltages $eV = \pm(\Delta + \epsilon_0)$ (Fig. 6.2, orange line). A naïve application of the Tien-Gordon-like Eq. (6.1), would lead to one V-shape stemming from each of these two threshold voltages with sidebands spaced by $\hbar\Omega/2$ corresponding to two-electron processes. Strikingly, the experiment revealed a very different behavior. Figure 6.3b shows the conductance measurement as a function of the radiation amplitude at high junction conductances. At the positive bias $eV = \Delta + \epsilon_0$, a V-shape is indeed visible although its sideband spacing as well as its modulation with the radiation amplitude both correspond to $\hbar\Omega$, seemingly indicating single-electron tunneling. More intriguingly still, a

---

[2] Parameters: $|u|^2/\nu_0 = 0.21\,\mathrm{meV}$, $|v|^2/\nu_0 = 0.83\,\mathrm{meV}$, $\Gamma_1 = 0.70\,\mu\mathrm{eV}$, $\Gamma_2 = 0.11\,\mu\mathrm{eV}$, $\nu_0 t^{\mathrm{low}} = 8.1 \times 10^{-4}$, $\nu_0 t^{\mathrm{high}} = 39 \times 8.1 \times 10^{-4}$. The BCS densities of states included a Dynes parameter [DNG78] $\Gamma_S = 20\,\mu\mathrm{eV}$ and the spectra where Gaussian-averaged with a width $\Gamma_{\mathrm{broadening}} = 60\,\mu\mathrm{eV}$.

Y-shape structure appears at negative voltages. Note that such a structure can not be reproduced by Eq. (6.1).

Chapter 7 introduces a full theory of photon-assisted resonant Andreev reflection via subgap states where we explain most aspects of the problem in considerable depth. Here, we content ourselves with a phenomenological explanation of the features observed in Fig. 6.3b. The Tien-Gordon approach fails to explain the photon-assisted resonant Andreev reflections due to two facts: the separate thresholds of the electron and hole tunneling rates and their dominant contribution to the broadening of the YSR state. Indeed, excellent theoretical agreement can be obtained from Eqs. (3.19)-(3.21) when applying the Tien-Gordon approach to the electron and hole tunneling rates separately:

$$\begin{aligned}
\Gamma_{e,\mathrm{eff}}(\omega) &= 2\pi t^2 |u|^2 \sum_n J_n^2\left(\frac{eV_{\mathrm{HF}}}{\hbar\Omega}\right)\nu(\omega_n),\\
\Gamma^{n_{\mathrm{F}}}_{e,\mathrm{eff}}(\omega) &= 2\pi t^2 |u|^2 \sum_n J_n^2\left(\frac{eV_{\mathrm{HF}}}{\hbar\Omega}\right)\nu(\omega_n) n_{\mathrm{F}}(\omega_n),\\
\Gamma^{1-n_{\mathrm{F}}}_{e,\mathrm{eff}}(\omega) &= 2\pi t^2 |u|^2 \sum_n J_n^2\left(\frac{eV_{\mathrm{HF}}}{\hbar\Omega}\right)\nu(\omega_n)[1 - n_{\mathrm{F}}(\omega_n)],
\end{aligned} \tag{6.4}$$

with $\omega_n = \omega + n\hbar\Omega$. The corresponding definitions for $\Gamma_{h,\mathrm{eff}}$ replace $|u|^2 \to |v|^2$. Note that we assumed a $\hbar\Omega$ spacing as each rate corresponds to a single-particle tunneling event. Figures 6.3c and d are numerical simulations of the differential conductance obtained from the total current calculated by inserting these effective rates in Eqs. (3.19)-(3.21). Unlike the simulations for bare superconductors, these simulations use only a few experimental parameters as input, with Figs. 6.3c and d differing only in the magnitude of the tunneling t across the junction. The agreement between theory and experiment is remarkable.

Let us now briefly explain why these effective rates lead to the differential conductance spectra measured in Fig. 6.3b. In the absence of radiation, the resonant Andreev reflection current in Eq. (3.21) is non-zero only when both the electron and hole tunneling rates are beyond their respective thresholds (6.3). In the presence of radiation, the effective rates $\Gamma_{e,\mathrm{eff}}$ and $\Gamma_{h,\mathrm{eff}}$, give rise to four V-shaped regions with vertices at the thresholds (6.3) as a result of the maximal number of emitted or absorbed photons eV_{HF}. Below the low-voltage threshold of the V-shapes, the corresponding tunneling rate is zero. Thus, current can only be measured within the outermost V-shapes, that is, the ones originating at $eV = \pm(\Delta + \epsilon_0)$. The Y-shape has its origin in the asymmetry in the electron and hole YSR wave functions $|u|^2 \ll |v|^2$. This leads to a hole tunneling rate $\Gamma_{h,\mathrm{eff}}$ in general significantly larger than the electron tunneling rate $\Gamma_{e,\mathrm{eff}}$. Thus, the electron tunneling is the rate-limiting process in the resonant Andreev reflection and its features translate into stronger conductance signals. This also explains why in Fig. 6.3b the positive-voltage V-shape only shows features originating in the photon-assisted electron tunneling thresholds. Similarly, at negative voltages, the signatures at the left arm and the inner part of the Y-shape correspond to electron thresholds. More mathematically, the suppression of the hole threshold signatures has its origin in the dominance of the hole tunneling rate $\Gamma_{h,\mathrm{eff}}$ in the resonance broadening $\Gamma(\omega)$, which leads to smaller, broader peaks at the hole thresholds. Only at the low-voltage arm of the Y-shape do the hole thresholds contribute noticeably in Fig. 6.3b. In this region, where the hole tunneling just sets in, both rates are comparable, so that the individual electron and hole thresholds contribute to the conductance signatures leading to the double structure visible in this region.

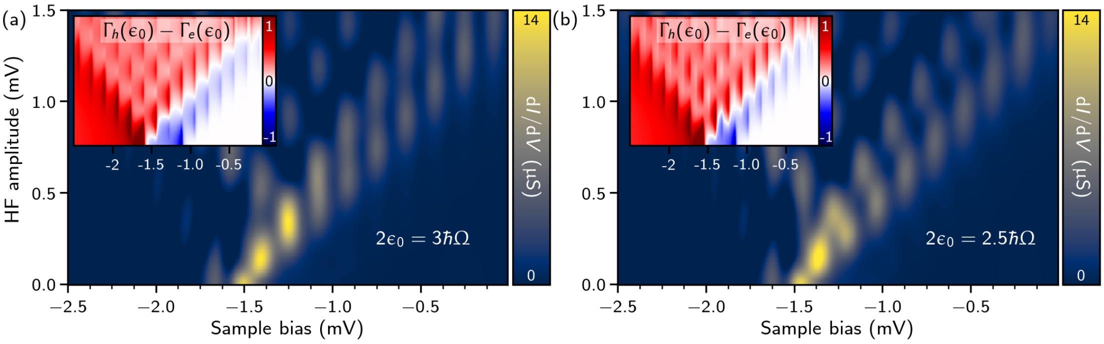

FIGURE 6.4: Numerical differential conductance spectra at negative bias via a YSR state under HF irradiation. Parameters are chosen to reproduce the Y shape observed in experiment. The peaks of the low voltage arm of the Y shape correspond to hole thresholds while the ones immediately above correspond to electron thresholds. In panel (a), the YSR energy satisfies $2\epsilon_0 = 3\hbar\Omega$, causing the peaks of both branches to occur at the same sample bias. This situation is close to the actual experimental parameters. In panel (b), with $2\epsilon_0 = 2.5\hbar\Omega$, the electron and hole thresholds are shifted by $\hbar\Omega/2$ from one another. The insets show the difference between the hole and electron tunneling rates in arbitrary units. Hole threshold peaks are only visible in the region were electron and hole tunneling rates are comparable and both nonzero, i.e., the white region between the blue and red areas.

The origin of the double structure is further illustrated in the numerical simulations of Fig. 6.4. Panel (a) shows the low-voltage arm of a Y-shape for which the YSR energy and the radiation frequency satisfy $2\epsilon_0 = 3\hbar\Omega$, as is the case in the experiment. Due to this relation, the peaks originating from electron and hole thresholds that form the double structure occur at the same voltages, appearing vertically on top of each other. Panel (b) differs only in the parameter ϵ_0, made to satisfy $2\epsilon_0 = 2.5\hbar\Omega$. This change shifts the peaks from electron and hole thresholds in opposite directions causing them to alternate in bias voltage. The insets show the difference between the electron and hole tunneling rates for each case. The asymmetry in the electron and hole YSR wave functions causes the hole tunneling rate to dominate for most bias voltages and radiation amplitudes with the exception of its low-voltage arm, where it has not yet completely set in. It is around this white region where the two rates are comparable, giving rise to the double structure.

In view of this discussion and the modifications to the rates in the current Eqs. (3.19)-(3.21) it is easy to understand why single-electron tunneling at low junction conductances does comply with the predictions of the Tien-Gordon-like Eq. (6.1). At low conductances, the resonance broadening is dominated by the frequency-independent thermal rates Γ_1 and Γ_2, leading to current integrands that are effectively linear in the electron or hole tunneling rates. This gives rise to independent conductance signatures at the corresponding electron and hole thresholds, as is well captured by Eq. (6.1).

6.5 CONCLUSION

Photon-assisted tunneling is a powerful tool to investigate and identify the different possible tunneling processes between two superconductors. For bare superconductors, the Tien-Gordon model successfully predicts the sideband splitting and modulation with radiation amplitude based on the charge transferred in an elementary tunneling event. These predictions break down for resonant

Andreev reflections via YSR states at high junction conductances. In this case, the individual electron and hole thresholds and their dominance of the broadening of the resonance require a more complete treatment that include effective photon-assisted electron and hole tunneling rates.

In the context of topological state engineering, resonant Andreev reflections underlie the tunneling signatures when probing putative Majorana modes [LLN09; Fle10] in chains of magnetic adatoms on s-wave superconductors [NP+14; Rub+15a; Paw+16; Fel+17; Jeo+17; Kim+18]. In the following Chapter, we develop a full theory of photon-assisted Andreev reflections via subgap states and argue that photon-assisted tunneling can be implemented to distinguish true zero-energy subgap states from states with a small but non-zero energy.

7

PHOTON-ASSISTED RESONANT ANDREEV REFLECTIONS: YU-SHIBA-RUSINOV AND MAJORANA STATES

7.1 INTRODUCTION

As discussed in the previous Chapter, photon-assisted tunneling frequently provides information on the underlying charge-transfer process. In particular, the Tien-Gordon approach and its extensions predict that the sideband spacing in bias voltage is a direct fingerprint of the number of electrons transferred in a single tunneling event. In this Chapter[1], we develop a full theory of photon-assisted tunneling into subgap states in superconductors in the limit of small temperatures and bias voltages where tunneling is dominated by resonant Andreev processes and does not conform to the predictions of simple Tien-Gordon theory. Our analysis is based on a systematic Keldysh calculation of the subgap conductance and provides a detailed analytical understanding of photon-assisted tunneling into subgap states, in excellent agreement with the experiment of Ref. [Pet+20]. Our theory includes tunneling to all orders in perturbation theory, generalizing the results of [Rub+15b]. We focus on tunneling from superconducting electrodes and into Yu-Shiba-Rusinov states associated with magnetic impurities or adatoms, but also explicitly extend our results to include normal-metal electrodes or other types of subgap states in superconductors. In particular, we argue that photon-assisted Andreev reflections provide a high-accuracy method to measure small, but nonzero energies of subgap states which can be important for distinguishing conventional subgap states from Majorana bound states.

Indeed, resonant Andreev reflections are an important tunneling process not only for YSR states, but also for other subgap states in superconductors. In particular, they dominate tunneling into Majorana bound states, where they are predicted to lead to a universal zero-bias conductance of $2e^2/h$ for tunneling from a normal-metal lead [LLN09; Fle10]. This has been at the focus of a large number of experiments [Lut+18] and recent measurements show evidence for this quantized conductance [Nic+17]. Our theory for photon-assisted resonant Andreev reflections is readily adapted to include tunneling into Majorana bound states [TZL15; Zan+19], and we find that photon-assisted tunneling can be an important tool to differentiate Majorana bound states from other subgap

---

[1] This Chapter is based on Ref. [AG+20] © 2020 American Physical Society. The author contributed to the development of the theory, the writing of the manuscript, wrote one of the two independently-developed codes, performed the numerical calculations and elaborated the Figures.

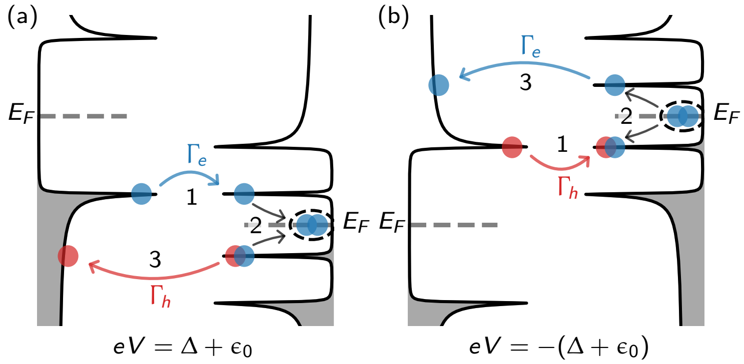

FIGURE 7.1: Resonant Andreev reflections via YSR bound states in superconductor-superconductor junctions at threshold (schematic, no high-frequency radiation). (a) For positive bias voltages, an electron (blue) first tunnels from the coherence peak of the superconducting tip (left superconductor) into the positive-energy YSR state, then forms a Cooper pair with another electron creating a hole (red) in the negative-energy YSR state. Finally, the hole tunnels back into the tip. Thus a Cooper pair is transferred into the substrate (right superconductor). (b) For negative bias voltages, a hole first tunnels from the coherence peak of the tip into the negative-energy YSR state. Then a Cooper pair breaks up in the substrate filling the hole and occupying the positive-energy YSR state. Finally the electron tunnels into the tip. The processes at positive and negative bias both create a pair of quasiparticles in the tip and generate or break up a Cooper pair in the substrate.

states. This is particularly true for tunneling from superconducting tips which have been extensively used for improved resolution in Majorana experiments on chains of magnetic adatoms [NP+14; Rub+15a; Fel+17; Rub+17]. Since tunneling into a Majorana bound state leaves behind an unpaired electron in the superconducting tip, it leads to two symmetric Majorana peaks at bias voltages $eV = \pm\Delta$, where Δ denotes the superconducting gap of the tip [Pen+15a]. This should be contrasted with tunneling into a conventional subgap state with a small, but nonzero energy ϵ_0, which appears as differential-conductance peaks at $eV = \pm(\Delta + \epsilon_0)$. Thus, the small energy of the subgap state can only be extracted from experiment as a difference of two much larger energies, the position of the resonance peak in $\mathrm{d}I/\mathrm{d}V$ and the superconducting gap of the tip. This is inherently prone to errors and requires an accurate determination of the tip gap. We find that in photon-assisted tunneling, the subgap energy appears directly as a spacing between resonant peaks in the spectrum, even for a superconducting tip. Moreover, these splittings appear in differential-conductance maps with high multiplicity, which effectively enhances the ability to resolve closely-spaced peaks. Before engaging in the technical derivation of the photon-assisted tunneling current, we begin with a more qualitative discussion of resonant Andreev reflections.

7.2 RESONANT ANDREEV PROCESSES VIA YSR STATES

YSR states induce additional resonances in the tunneling conductance at subgap voltages $e|V| < 2\Delta$. At zero temperature, the subgap current cannot be carried by single electrons. Due to the absence of bulk states at these energies, single electrons cannot leave the junction region. Instead, the dominant current-carrying process is an Andreev process closely related to the lowest multiple

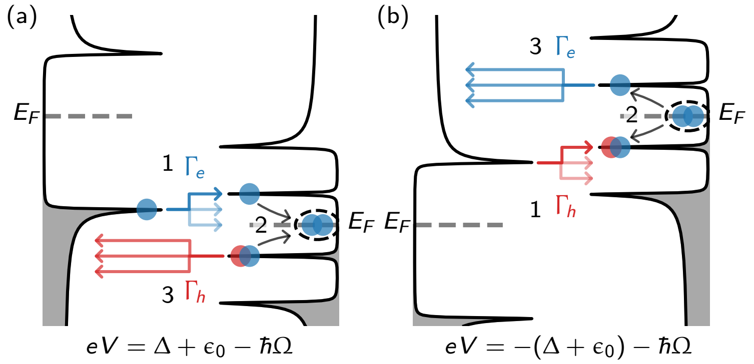

FIGURE 7.2: Photon-assisted resonant Andreev reflections via YSR bound states in superconductor-superconductor junctions (schematic). Panel (a) shows the process for positive bias voltages, panel (b) for negative biases. The basic process is as in Fig. 7.1. The high-frequency radiation (frequency Ω) allows electrons and holes to change their energy by multiples of $\hbar\Omega$. The number of relevant sidebands is limited by the maximal energy eV_{HF} that the tunneling electrons and holes can gain or lose due to the high-frequency field and therefore grows linearly in V_{HF}.

Andreev process discussed in Section 6.3 with $m = 2$ [Dea+10; Rub+15b; Ran+16; Lee+17; Bra+18; Far+18]. This resonant Andreev reflection is best viewed as a coherent multistep process and was already explained in Section 3.3. Due to its central importance to this Chapter, we reproduce and expand the explanation here. Consider first the situation when electrons are tunneling from the tip into the substrate (positive bias voltage, Fig. 7.1a). In this case, the tunneling amplitude involves the following steps. An electron from the tip tunnels into the positive energy YSR state. Subsequently, the electron combines with an electron in the substrate to form a Cooper pair, allowing the charge to exit the junction region and creating a hole in the negative-energy YSR state. Finally, the hole tunnels back into the tip.

This process must satisfy two conditions to be energetically allowed, one each for electron and hole [Rub+15b; Pet+20]. The electron tunneling process virtually occupies the YSR state of energy ϵ_0 and leaves an unpaired electron behind in the tip, and is thus allowed when $eV > \Delta + \epsilon_0$. The hole tunneling process injects a hole into the quasiparticle continuum and thus requires $eV > \Delta - \epsilon_0$. Since $\epsilon_0 > 0$, the condition for hole tunneling is automatically satisfied whenever the condition for electron tunneling is met. Thus, resonant Andreev reflection induces a peak in the differential conductance at the threshold bias voltage $eV^{\text{th}}_{e+} = \Delta + \epsilon_0$ of electron tunneling. In contrast, there is no peak at the hole threshold $eV^{\text{th}}_{h+} = \Delta - \epsilon_0$ since the electron process is not yet energetically allowed.

In the presence of an *ac* field, both the electron and the hole can emit or absorb photons during tunneling and the energetic conditions change to $eV > \Delta + \epsilon_0 + n\hbar\Omega$ for the electron and $eV > \Delta - \epsilon_0 + m\hbar\Omega$ for the hole. Correspondingly, there are two sets of sidebands in the differential conductance, one at $eV = \Delta + \epsilon_0 + n\hbar\Omega$ due to the condition for electron tunneling and another at $eV = \Delta - \epsilon_0 + m\hbar\Omega$ due to the condition for hole tunneling. The junction in the presence of radiation is depicted in Fig. 7.2, where the absorption or emission of only one photon is considered. Electron and hole can both gain or lose a maximal energy of eV_{HF} due to the *ac* field. Thus, the electron sidebands are

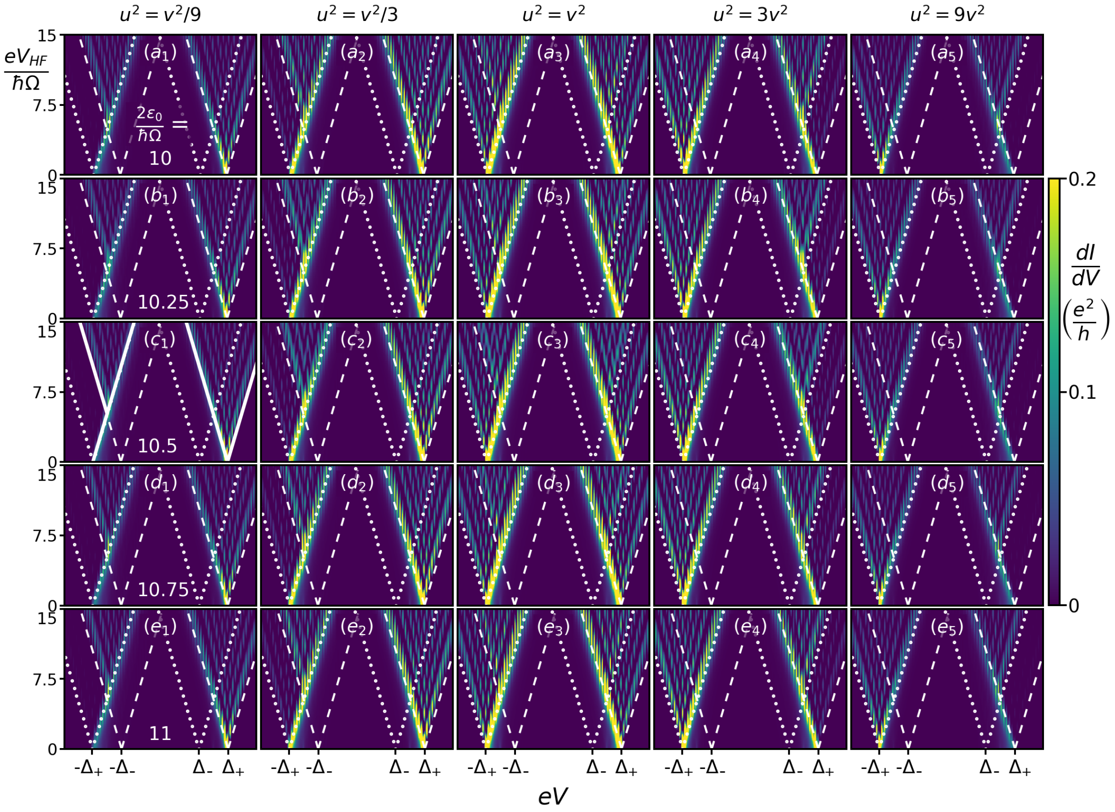

FIGURE 7.3: Differential conductance (color scale) as a function of bias voltage eV and amplitude eV_{HF} of the high-frequency radiation for tunneling into YSR state from a superconducting tip via resonant Andreev reflections. The panels differ in the ratio between electron and hole wave functions u and v (left to right) and in the ratio between YSR state energy ϵ_0 and photon energy $\hbar\Omega$ (top to bottom). Numerical values are indicated in the figure. These results are obtained for $u^2 + v^2 = 1$ fixed for all panels. The regions with electron and hole sidebands are indicated by white dashed and dotted V-shapes, respectively, centered at $e|V| = \Delta_\pm = \Delta \pm \epsilon_0$. Notice the appearance of V and Y-shaped regions, as highlighted in panel (c1). For a detailed discussion, see Sec. 7.2. Parameters: $\Omega/\Delta = 0.05$, $\nu_0|t| = 0.04$.

restricted to the voltage region

$$|eV - (\Delta + \epsilon_0)| \lesssim eV_{\mathrm{HF}}, \tag{7.1}$$

and the hole sidebands to

$$|eV - (\Delta - \epsilon_0)| \lesssim eV_{\mathrm{HF}}. \tag{7.2}$$

These V-shaped regions are indicated in Fig. 7.3 as dashed (electrons) and dotted (holes) lines. The sidebands are observable only as long as both electron and hole tunneling are allowed. For positive bias, this limits them to the voltage range (7.1) for electron sidebands. Within this region, only electron sidebands are observed for $eV > \Delta - \epsilon_0 + eV_{\mathrm{HF}}$, i.e., outside the dotted V-shape for hole sidebands. Both electron and hole sidebands contribute for $eV < \Delta - \epsilon_0 + eV_{\mathrm{HF}}$, which corresponds to the region where the dashed and dotted V-shapes overlap.

At negative bias voltages, there is a corresponding process in which a hole tunnels from the tip into the negative-energy YSR state, a Cooper pair breaks up and occupies both YSR states at positive and negative energies, and finally, an electron tunnels back from the positive energy YSR state into the tip, see Fig. 7.2b. In this process, the hole sidebands are limited to the region

$$|eV + (\Delta + \epsilon_0)| \lesssim eV_{\mathrm{HF}}, \tag{7.3}$$

while electron sidebands can appear in the region

$$|eV + (\Delta - \epsilon_0)| \lesssim eV_{\mathrm{HF}}. \tag{7.4}$$

In the absence of high-frequency radiation, it is now the electron process that is above threshold whenever the hole process is, and sidebands can only be observed within the hole sideband region (7.3).

Based on our full theoretical results (see Section 7.4), Fig. 7.3 exhibits the differential conductance as a function of both bias voltage V and amplitude V_{HF} of the ac field. From top to bottom, the panels differ in the ratio between YSR energy ϵ_0 and photon energy $\hbar\Omega$. From left to right, the panels differ in the ratio between electron and hole wave functions u and v, respectively, evaluated at the tip position. First consider the column of central panels for equal amplitudes of electron and hole wave functions, $|u|^2 = |v|^2$. The differential conductance exhibits pronounced V-shapes centered at $eV = \pm(\Delta + \epsilon_0)$. At positive bias, this V-shape reflects the region with electron sidebands given in Eq. (7.1), at negative biases the region with hole sidebands given in Eq. (7.3).

These panels also show clear evidence for the importance of both the electron and the hole condition. The panels in Fig. 7.3 delineate the V-shaped regions both for electron tunneling (dashed white lines) and for hole tunneling (dotted white lines). The sideband structure within the outer V-shaped regions differs markedly between the overlap region of the two V-shapes and the region outside the inner V-shape. Generically, one observes a larger number of sidebands within the overlap region where both electron and hole thresholds contribute. Only when $2\epsilon_0$ is commensurate with $\hbar\Omega$, electron and hole thresholds coincide and the sidebands in the overlap region appear brighter, but not more numerous.

Notably, the inner arms of the V-shapes appear brighter than the outer ones. This can be understood as follows. The sidebands appear brighter in the differential conductance, if the YSR resonance is sharp. The width of the YSR resonance is controlled by the electron and hole tunneling rates. Along the inner arm, one of the tunneling processes is just barely setting in, so that the width is considerably smaller than along the outer arm, where both electron and hole tunneling are fully allowed.

The patterns depend strongly on the ratio between electron and hole wave functions. Consider now the leftmost column of panels in Fig. 7.3, for which the hole wave function is considerably larger than the electron wave function, $|u|^2 = |v|^2/9$. While one still observes a V-shaped region of sidebands for positive bias voltages, the region takes on a Y-shape for negative biases. Since the hole wave function is much larger, hole tunneling rates are intrinsically larger than electron tunneling rates. In this case, electron tunneling is effectively the rate-limiting process (see Section 7.4.1.iii for a careful discussion of this statement) and electron thresholds are considerably more pronounced than hole thresholds. Thus, sidebands are only observed within the overlap region. The only exception is the "stem" of the Y-shape along which hole tunneling just sets in and is still comparable in magnitude to electron tunneling. The situation is analogous in the rightmost column in Fig. 7.3, for which the electron tunneling

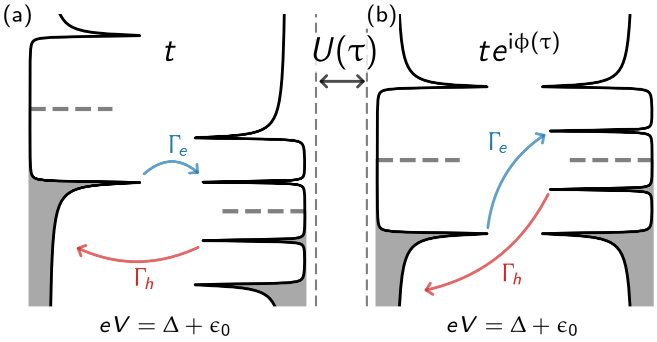

FIGURE 7.4: Alternative representations of electron and hole tunneling in the presence of a bias voltage: (a) Left and right superconductors have chemical potentials which are shifted relative to one another by the applied bias voltage eV. In this representation, tunneling is horizontal, leaving the energy unchanged. (b) Alternatively, a time-dependent unitary transformation, see Eq. (7.9), shifts the chemical potentials of left and right superconductor such that they become equal, and tunneling of electrons and holes is associated with an energy transfer equal to eV. We use the representation in panel (a) for figures, but the calculations (and their description) are systematically performed using the representation in panel (b).

rate is typically much larger than the hole tunneling rate and a (reflected) Y-like shape appears at positive bias voltages.

Since one set of sidebands dominates for strongly asymmetric electron and hole wave functions, the sidebands no longer depend sensitively on the commensurability between $2\epsilon_0$ and $\hbar\Omega$, but appear with a regular voltage spacing of $\hbar\Omega$. In view of the simple Tien-Gordon relation in Eq. (6.1), this seemingly suggests that the underlying tunneling process is a single-electron process. Nevertheless, resonant Andreev reflections transfer electron pairs into the substrate superconductor and should be viewed as a single coherent process. This emphasizes that photon-assisted resonant Andreev reflections do not conform to the predictions of a simple Tien-Gordon approach.

7.3 MODEL

We consider a junction involving a superconducting tip and substrate (or other kinds of superconducting electrodes) with Hamiltonians $\tilde{H}_L$ and $\tilde{H}_R$, respectively. Electrons can tunnel between tip and substrate as described by the tunneling Hamiltonian

$$\tilde{H}_T = \sum_\sigma \left[t c^\dagger_{L,\sigma}(\mathbf{R}) c_{R,\sigma}(\mathbf{R}) + \text{h.c.} \right], \tag{7.5}$$

where $c^\dagger_{\alpha,\sigma}(\mathbf{r})$ creates an electron at position $\mathbf{r}$ and spin σ in the tip ($\alpha = L$) or the substrate ($\alpha = R$) and $\mathbf{R}$ denotes the position of the tip. The Hamiltonian

$$\tilde{H} = \tilde{H}_L + \tilde{H}_R + \tilde{H}_T \tag{7.6}$$

measures energy on an absolute scale and conserves the total particle number $N = N_L + N_R$. The time-dependent bias $V(\tau)$ between tip and substrate is included by holding tip and substrate at different chemical potentials μ_L and μ_R,

$$eV(\tau) = \mu_L - \mu_R, \tag{7.7}$$

and is the sum of an applied *dc* voltage V and an *ac* voltage

$$V_{\mathrm{ac}}(\tau) = V_{\mathrm{HF}} \cos(\Omega\tau) \tag{7.8}$$

generated by the radiation field of frequency Ω [TG63].

To apply the usual BCS mean-field description of the superconducting tip and substrate, we perform a time-dependent canonical transformation (setting $\hbar = 1$)

$$U(\tau) = \exp\left\{ i \int_0^\tau \mathrm{d}\tau' [\mu_L(\tau')N_L + \mu_R(\tau')N_R] \right\}, \tag{7.9}$$

so that single-particle energies in tip and substrate are measured from the respective chemical potentials μ_L and μ_R. The transformed Hamiltonian $H = U\tilde{H}U^\dagger - iU\partial_\tau U^\dagger$ takes the form

$$H = (\tilde{H}_L - \mu_L N_L) + (\tilde{H}_R - \mu_R N_R) + U\tilde{H}_T U^\dagger. \tag{7.10}$$

Here, we used that $\tilde{H}_L$ and $\tilde{H}_R$ conserve N_L and N_R, so that $U\tilde{H}_\alpha U^\dagger = \tilde{H}_\alpha$. Then, the time dependence enters only through the transformed tunneling Hamiltonian $H_T = U\tilde{H}_T U^\dagger$ with

$$H_T = \sum_\sigma \left[t e^{i\phi(\tau)} c^\dagger_{L,\sigma}(\mathbf{R}) c_{R,\sigma}(\mathbf{R}) + \mathrm{h.c.} \right], \tag{7.11}$$

where the tunneling amplitude t acquires a time-dependent phase

$$\phi(\tau) = eV\tau + \frac{eV_{\mathrm{HF}}}{\Omega} \sin(\Omega\tau) \tag{7.12}$$

as a result of the canonical transformation. While the time-independent $\tilde{H}_T$ conserves the energy of the tunneling electron or hole, the time-dependent H_T changes the energy due to both, the applied *dc* and *ac* biases. This corresponds to different representations of the same tunneling process as illustrated in Fig. 7.4.

In the transformed Hamiltonian, we can now make the usual BCS mean field approximation for both $H_L = \tilde{H}_L - \mu_L N_L$ and $H_R = \tilde{H}_R - \mu_R N_R$. The unperturbed Hamiltonian $H_0 = H_L + H_R$ can then be written as

$$\begin{aligned} H_0 &= \sum_{\mathbf{k},\alpha} \sum_\sigma \left[\xi_{\mathbf{k},\alpha} c^\dagger_{\alpha,\mathbf{k}\sigma} c_{\alpha,\mathbf{k}\sigma} + \left(\Delta c^\dagger_{\alpha,\mathbf{k}\uparrow} c^\dagger_{\alpha,-\mathbf{k}\downarrow} + \mathrm{h.c.} \right) \right] \\ &\quad + \sum_{\mathbf{k},\mathbf{k}'} \sum_\sigma (K - JS\sigma) c^\dagger_{R,\mathbf{k}\sigma} c_{R,\mathbf{k}'\sigma}, \end{aligned} \tag{7.13}$$

where $\xi_{\mathbf{k},\alpha} = \epsilon_{\mathbf{k}} - \mu_\alpha$ denotes the normal-state dispersion and $c^\dagger_{\alpha,\mathbf{k}\sigma}$ creates an electron with momentum $\mathbf{k}$. The superconducting gap Δ is taken to be identical for tip and substrate. A magnetic adatom with spin $\mathbf{S}$ is located at the origin and modeled as a classical impurity which couples to the substrate electrons via potential scattering of strength K and exchange coupling J. Note that we choose the spin quantization axis of the electrons parallel to the impurity spin.

The current operator $I = -e\dot{N}_L$ takes the form

$$\begin{aligned} I &= -ie[H_T, N_L] \\ &= ie \sum_\sigma \left(t e^{i\phi(\tau)} c^\dagger_{L,\sigma}(\mathbf{R}) c_{R,\sigma}(\mathbf{R}) - \mathrm{h.c.} \right) \end{aligned} \tag{7.14}$$

and the current becomes

$$I(\tau) = e\mathrm{Tr}\left\{\tau_z\left[\hat{t}(\tau)G^<_{RL}(\tau,\tau) - G^<_{LR}(\tau,\tau)\hat{t}^*(\tau)\right]\right\}. \tag{7.15}$$

Here, we have expressed the expectation values in terms of the lesser Green function in Nambu space,

$$G^<_{\alpha\beta}(\tau_1,\tau_2) = i\begin{pmatrix} \langle c^\dagger_{\beta\uparrow}(\tau_2)c_{\alpha\uparrow}(\tau_1)\rangle & \langle c_{\beta\downarrow}(\tau_2)c_{\alpha\uparrow}(\tau_1)\rangle \\ \langle c^\dagger_{\beta\uparrow}(\tau_2)c^\dagger_{\alpha\downarrow}(\tau_1)\rangle & \langle c_{\beta\downarrow}(\tau_2)c^\dagger_{\alpha\downarrow}(\tau_1)\rangle \end{pmatrix}, \tag{7.16}$$

introduced the hopping matrix

$$\hat{t}(\tau) = \begin{pmatrix} te^{i\phi(\tau)} & 0 \\ 0 & -t^*e^{-i\phi(\tau)} \end{pmatrix}, \tag{7.17}$$

and used the Pauli matrix τ_z in Nambu space. Here and in the following, electron operators (as well as Green functions and self energies) without momentum or position labels refer to the tip position $\mathbf{R}$.

Writing Dyson equations for the Keldysh Green function and using the Langreth rules, the lesser Green functions can be written as

$$\begin{aligned} G^<_{LR} &= (g_L\hat{t}G_R)^< &&= g^<_L\hat{t}G^a_R + g^r_L\hat{t}G^<_R \\ G^<_{RL} &= (G_R\hat{t}^*g_L)^< &&= G^<_R\hat{t}^*g^a_L + G^r_R\hat{t}^*g^<_L. \end{aligned} \tag{7.18}$$

The superscripts r and a denote retarded and advanced Green functions. The bare Green function (in Nambu space) of tip or substrate in the absence of tunneling is denoted as g_α ($\alpha = L, R$), while the Green function of the substrate which accounts for the tip-substrate tunneling through a self energy

$$\Sigma_R(\tau,\tau') = \hat{t}^*(\tau)g_L(\tau,\tau')\hat{t}(\tau') \tag{7.19}$$

takes the form $G_R = [g_R^{-1} - \Sigma_R]^{-1}$. Inserting Eqs. (7.18) into the expression (7.15) for the current, we find

$$\begin{aligned} I(\tau) \quad = \quad & e\int \mathrm{d}\tau'\,\mathrm{Tr}\left\{\tau_z\left[G^<_R(\tau,\tau')\Sigma^a_R(\tau',\tau) + G^r_R(\tau,\tau')\Sigma^<_R(\tau',\tau)\right.\right. \\ & \left.\left. -\Sigma^<_R(\tau,\tau')G^a_R(\tau',\tau) - \Sigma^r_R(\tau,\tau')G^<_R(\tau',\tau)\right]\right\}. \end{aligned} \tag{7.20}$$

Here, we used that the hopping matrix $\hat{t}$ commutes with τ_z.

7.4 RESONANT ANDREEV REFLECTIONS

While the YSR states resonantly enhance Andreev processes in the substrate, no such enhancement occurs for Andreev reflections in the tip. For this reason, we effectively neglect the latter. In this approximation, there are no multiple Andreev reflections, and the dominant processes contributing to the subgap conductance involve a single resonant Andreev reflection in the substrate. We can implement this approximation by neglecting the off-diagonal contributions to the Nambu Green function g_L of the tip when computing the self energy Σ_R. In this approximation, g_L is proportional to the unit matrix (see App. A for details).

To compute the self energy Σ_R within this approximation, we note that

$$e^{i\phi(\tau)} = \sum_{n=-\infty}^{\infty} J_n\left(\frac{eV_{\mathrm{HF}}}{\Omega}\right) e^{i(eV+n\Omega)\tau}, \tag{7.21}$$

where $J_n(x)$ denotes a Bessel function. Inserting this into Eq. (7.19), we obtain

$$\begin{aligned}\Sigma_R(\tau,\tau') = |t|^2 \sum_{n,m} J_n\left(\frac{eV_{\mathrm{HF}}}{\Omega}\right) J_m\left(\frac{eV_{\mathrm{HF}}}{\Omega}\right)\\ \times e^{-i(eV+n\Omega)\tau\tau_z} g_L(\tau-\tau') e^{i(eV+m\Omega)\tau'\tau_z}.\end{aligned} \tag{7.22}$$

This expression can be viewed as a sum of a diagonal ($n = m$) and an off-diagonal ($n \neq m$) contribution,

$$\Sigma_R = \Sigma_R^0 + \Sigma_R^1 \tag{7.23}$$

with

$$\begin{aligned}\Sigma_R^0(\tau,\tau') = |t|^2 \sum_n J_n^2(eV_{\mathrm{HF}}/\Omega)\\ \times e^{-i(eV+n\Omega)\tau\tau_z} g_L(\tau-\tau') e^{i(eV+n\Omega)\tau'\tau_z}.\end{aligned} \tag{7.24}$$

The calculation simplifies significantly when retaining only the diagonal self energy Σ_R^0. We find that this is frequently an excellent approximation. For this reason, we first discuss this simplified situation (referred to below as diagonal approximation) before presenting the more general case.

7.4.1 DIAGONAL APPROXIMATION

i) DERIVATION

Within the diagonal approximation, the self energy is only a function of the difference $\tau - \tau'$ of its time arguments and thus diagonal in frequency representation. Then, the exponential factors in Eq. (7.24) effectively act as translation operators and we obtain

$$\Sigma_R^0(\omega) = |t|^2 \sum_n J_n^2(eV_{\mathrm{HF}}/\Omega) g_L(\omega - (eV + n\Omega)\tau_z). \tag{7.25}$$

Here, the frequency argument of the Green function g_L reflects that due to bias voltage and ac field, electrons (holes) propagating in the substrate lose (gain) an energy $eV + n\Omega$ when tunneling into the tip.

As we are considering subgap energies in the substrate, we only retain the contribution to the substrate Green function which originate from the YSR state with energy ϵ_0. Then, the retarded and advanced Green functions become (see App. B for details)

$$G_R^{r/a}(\omega) = \varphi \frac{1}{\omega - \epsilon_0 - \Lambda(\omega) \pm \frac{i}{2}\Gamma(\omega)} \varphi^\dagger. \tag{7.26}$$

Here, $\varphi = (u, v)^T$ denotes the Bogoliubov-de Gennes wave function of the positive-energy YSR state at the tip position $\mathbf{R}$ and we separated the retarded and advanced self energy projected onto the YSR state

$$\tilde{\Sigma}_R^{0,r/e}(\omega) = \varphi^\dagger \Sigma_R^0(\omega) \varphi = \Lambda(\omega) \mp \frac{i}{2}\Gamma(\omega) \tag{7.27}$$

into real and imaginary parts.

The projected self energy takes the explicit form

$$\begin{aligned}\tilde{\Sigma}^0_R(\omega) &= |t|^2 \sum_n J_n^2(eV_{\rm HF}/\Omega) \\ &\times \left\{|u|^2 g_L(\omega-(eV+n\Omega)) + |v|^2 g_L(\omega+(eV+n\Omega))\right\}. \end{aligned} \tag{7.28}$$

Using Eq. (A.8) in App. A, the imaginary part $\Gamma(\omega)$ is given by

$$\begin{aligned}\Gamma(\omega) &= \sum_n J_n^2(eV_{\rm HF}/\Omega) \\ &\times [\Gamma_e(\omega-(eV+n\Omega)) + \Gamma_h(\omega+(eV+n\Omega))], \end{aligned} \tag{7.29}$$

which combines contributions to the broadening of the YSR state due to photon-assisted tunneling of electrons and holes into the tip. Here, we defined the electron and hole tunneling rates

$$\Gamma_e(\omega) = 2\pi|u|^2|t|^2\nu(\omega), \tag{7.30}$$

$$\Gamma_h(\omega) = 2\pi|v|^2|t|^2\nu(\omega) \tag{7.31}$$

with the BCS density of states

$$\nu(\omega) = \nu_0 \frac{|\omega|}{\sqrt{\omega^2-\Delta^2}}\theta(|\omega|-\Delta) \tag{7.32}$$

of the tip. (ν_0 is the normal-state density of states per spin direction.) Similarly, the real part of the self energy becomes

$$\begin{aligned}\Lambda(\omega) &= -\pi\nu_0|t|^2 \sum_n J_n^2(eV_{\rm HF}/\Omega) \\ &\times \left\{ \frac{|u|^2[\omega-(eV+n\Omega)]}{\sqrt{\Delta^2-[\omega-(eV+n\Omega)]^2}}\theta(\Delta-|\omega-(eV+n\Omega)|) \right. \\ &\left. + \frac{|v|^2[\omega+(eV+n\Omega)]}{\sqrt{\Delta^2-[\omega+(eV+n\Omega)]^2}}\theta(\Delta-|\omega+(eV+n\Omega)|) \right\}, \end{aligned} \tag{7.33}$$

describing a (frequency-dependent) renormalization of the energy of the YSR state.

The lesser self energy can be expressed by inserting Eq. (A.9) into Eq. (7.28). This yields

$$\begin{aligned}\tilde{\Sigma}^<_R(\omega) &= i \sum_n J_n^2(eV_{\rm HF}/\Omega) \\ &\times [\Gamma_e(\omega-(eV+n\Omega)) n_F(\omega-(eV+n\Omega)) \\ &+ \Gamma_h(\omega+(eV+n\Omega))] n_F(\omega+(eV+n\Omega))]. \end{aligned} \tag{7.34}$$

This also yields the lesser Green function

$$G^<_R(\omega) = \psi \frac{\tilde{\Sigma}^<_R(\omega)}{[\omega-\epsilon_0-\Lambda(\omega)]^2+\frac{1}{4}\Gamma^2(\omega)}\psi^\dagger \tag{7.35}$$

of the substrate using the relation (B.9) in App. B.

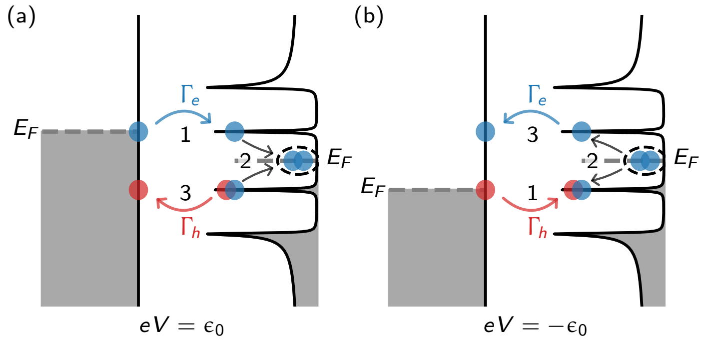

FIGURE 7.5: Resonant Andreev reflections from a YSR state with a normal-state electrode for (a) positive and (b) negative polarity of the bias voltage V (schematic, no high-frequency radiation).

Within the diagonal approximation, we can then express Eq. (7.20) for the current in frequency representation,

$$\begin{aligned} I(\tau) \quad = \quad & e \int \frac{\mathrm{d}\omega}{2\pi} \mathrm{Tr}\left\{\tau_z \left[G^<_R(\omega)\Sigma^a_R(\omega) + G^r_R(\omega)\Sigma^<_R(\omega)\right.\right. \\ & \left.\left. -\Sigma^<_R(\omega)G^a_R(\omega) - \Sigma^r_R(\omega)G^<_R(\omega)\right]\right\}. \end{aligned} \tag{7.36}$$

This can be written in the alternative form

$$\begin{aligned} I \quad = \quad & e \int \frac{\mathrm{d}\omega}{2\pi} \mathrm{Tr}\left\{\tau_z \left[G^r_R(\omega)(\Sigma^r_R(\omega) - \Sigma^a_R(\omega))G^a_R(\omega)\Sigma^<_R(\omega)\right.\right. \\ & \left.\left. -G^r_R(\omega)\Sigma^<_R(\omega)G^a_R(\omega)\left(\Sigma^r_R(\omega) - \Sigma^a_R(\omega)\right)\right]\right\} \end{aligned} \tag{7.37}$$

using that the self energy Σ_R is also diagonal in Nambu space and commutes with τ_z as well as the identities $G^r_R - G^a_R = G^r_R(\Sigma^r_R - \Sigma^a_r)G^a_R$ and $G^<_R = G^r_R\Sigma^<_R G^a_R$ (see Appendix B).

With this, we are now in a position to evaluate the current in Eq. (7.37) and obtain

$$\begin{aligned} I = 2e \int \frac{\mathrm{d}\omega}{2\pi} & \sum_{n,m} J^2_n(eV_{\mathrm{HF}}/\Omega)J^2_m(eV_{\mathrm{HF}}/\Omega) \\ & \times \frac{\Gamma_e(\omega - (eV + n\Omega))\Gamma_h(\omega + (eV + m\Omega))}{[\omega - \epsilon_0 - \Lambda(\omega)]^2 + \frac{1}{4}\Gamma^2(\omega)} \\ & \times [n_F(\omega - (eV + n\Omega)) - n_F(\omega + (eV + m\Omega))] \end{aligned} \tag{7.38}$$

after some straightforward algebra. This expression generalizes the results of Ref. [Rub+15b] to include photon-assisted processes and is a main result of this Chapter. While the current does not obey the simple Tien-Gordon relations (6.1), the electron and hole tunneling rates by themselves behave in a Tien-Gordon-like manner. Equation (7.38) is not only in excellent agreement with the more complete treatment shown below, but also with recent experimental results [Pet+20]. Note that we have approximated the substrate Green function by retaining the contribution of the subgap state only. As a result, Eq. (7.38) describes only those sidebands which fall within the superconducting gap. In effect, this imposes upper cutoffs on the frequency and amplitude of the HF radiation. Except for these cutoffs, the results are independent of the substrate gap.

ii) NORMAL-METAL TIP

As a first application of Eq. (7.38), consider a normal-metal tip (temporarily setting $\Delta = 0$ in the self energy) in the absence of the ac field. Then, the self energy is purely imaginary and frequency independent, so that the bias voltage enters only into the Fermi functions (see Fig. 7.5 for a schematic representation). This allows one to evaluate the zero-temperature differential conductance,

$$\frac{\mathrm{d}I}{\mathrm{d}V} = \frac{2e^2}{h} \sum_{\pm} \frac{\gamma_e \gamma_h}{(eV \pm \epsilon_0)^2 + (\gamma_e + \gamma_h)^2/4}, \tag{7.39}$$

where we have reinstated Planck's constant and defined $\gamma_e = 2\pi |u|^2 |t|^2 \nu_0$ as well as $\gamma_h = 2\pi |v|^2 |t|^2 \nu_0$. This yields two symmetric resonances at $eV = \pm\epsilon_0$ with peak height

$$\left.\frac{\mathrm{d}I}{\mathrm{d}V}\right|_{\text{peak}} = \frac{2e^2}{h} \frac{4|u|^2|v|^2}{(|u|^2 + |v|^2)^2}. \tag{7.40}$$

Thus, the peak height depends on the relative magnitudes of the electron and hole wave functions of the YSR state and has a maximal value of $2e^2/h$, as long as the positive- and negative-energy peaks are well separated. Specifically, the peak height becomes maximal when the electron and hole wave functions at the tip position are equal, $|u|^2 = |v|^2$. For a YSR state with zero energy, the two peaks coalesce and the maximal peak height equals $4e^2/h$. This should be compared to analogous results for Majorana bound states which give a peak conductance of $2e^2/h$ [LLN09; Fle10], reflecting the fact that unlike YSR states, Majorana bound states effectively correspond to only half a conventional fermionic excitation. We elaborate on this in Section 7.5.

In the presence of the ac field, the zero-temperature differential conductance becomes

$$\frac{\mathrm{d}I}{\mathrm{d}V} = \frac{2e^2}{h} \sum_n \sum_{\pm} \frac{J_n^2(eV_{\text{HF}}/\hbar\Omega)\gamma_e\gamma_h}{(eV + n\hbar\Omega \pm \epsilon_0)^2 + \frac{(\gamma_e+\gamma_h)^2}{4}}, \tag{7.41}$$

using the Bessel-function identity $\sum_n J_n^2(x) = 1$. Thus, the conductance peaks at $eV = \pm\epsilon_0$ develop sidebands whose spacings are given by the photon frequency $\hbar\Omega$ and whose amplitudes are controlled by Bessel functions.

At finite temperatures, the peaks become convolutions of the Lorentzian with derivatives of the Fermi function. Here, we assume that the temperature is still sufficiently small compared to the substrate gap so that we can neglect inelastic processes which couple the YSR state to the quasiparticle continuum of the substrate. Once the latter become relevant, there is an additional contribution to the current originating from single-electron tunneling. (An experimental fingerprint of the latter is that it generically leads to asymmetric conductance peaks at $eV = \pm\epsilon_0$ [BVZ06; Rub+15b].)

iii) SUPERCONDUCTING TIP

We can now make contact with the physical discussion for a superconducting tip in Section 7.2. The advantages of superconducting tips are twofold. First, they enhance energy resolution owing to the sharp peak in the BCS density of states at the gap edge. Second, when the tip is superconducting, the YSR peaks appear at $eV = \pm(\Delta + \epsilon_0)$ and the Fermi-function factor in Eq. (7.38) equals ± 1 to exponential precision in T/Δ. Thus, the current is insensitive to temperature as long as $T \ll \Delta$, a much weaker condition than for normal-state tips where temperature should be compared to the intrinsic width of the YSR resonance [Žit16].

Expression (7.38) clearly exhibits the coherent nature of the underlying tunneling process. Analogous to conventional resonant tunneling through a bound state [Bra97; LY+97], the electron and hole tunneling rates Γ_e and Γ_h enter not only in the numerator, but also determine the broadening of the YSR resonance denominator, as advanced in Section 3.3. The current is then nonperturbative in the tip-substrate tunneling, and consequently *sublinear* in the normal-state conductance of the tunnel junction [Rub+15b].

An explicit evaluation of the differential conductance must take into account that as a consequence of the BCS density of states of the tip, the tunneling rates are themselves functions of ω [Rub+15b]. In the following, we partially reproduce the derivation of the differential conductance peaks in the absence of radiation of Section 3.3, for which Eq. (7.38) reduces to Eq. (3.21). For positive bias voltages near the threshold $eV_{e_+}^{\mathrm{th}} = \Delta + \epsilon_0$ the hole tunneling rate is nonsingular:

$$\Gamma_h^{\mathrm{th},e} \simeq \gamma_h \sqrt{\frac{\Delta}{4\epsilon_0}}, \tag{7.42}$$

where we have assumed that the resonance broadening is small compared to ϵ_0 such that the current integral has weight for ω close to ϵ_0. We further assumed $\epsilon_0 \ll \Delta$. In contrast, the electron tunneling rate becomes singular,

$$\Gamma_e(\omega - eV_{e_+}^{\mathrm{th}}) \simeq \gamma_e \sqrt{\frac{\Delta}{2(\epsilon_0 - \omega)}}\theta(\epsilon_0 - \omega). \tag{7.43}$$

This situation corresponds to the schematic representation of Fig. 7.1(a), where the positive-energy YSR state matches with the BCS singularity while the negative-energy YSR is at a distance $2\epsilon_0$ from the singularity. Thus, the characteristic electron scattering rate $\Gamma_e^{\mathrm{th},e}$ depends on whether the broadening Γ is dominated by electron or hole tunneling. If the hole tunneling dominates the broadening, $\Gamma_h^{\mathrm{th},e} \gg \Gamma_e^{\mathrm{th},e}$, the characteristic electron tunneling rate becomes $\Gamma_e^{\mathrm{th},e} \sim \gamma_e(\Delta/\Gamma_h^{\mathrm{th},e})^{1/2}$, and we find

$$\left.\frac{\mathrm{d}I}{\mathrm{d}V}\right|_{\mathrm{peak},+} \sim \frac{2e^2}{h}\frac{\Gamma_e^{\mathrm{th},e}}{\Gamma_h^{\mathrm{th},e}} \sim \frac{2e^2}{h}\frac{\gamma_e \epsilon_0^{3/4}}{\gamma_h^{3/2}\Delta^{1/4}}. \tag{7.44}$$

If, on the contrary, electron tunneling dominates the broadening, $\Gamma_e^{\mathrm{th},e} \gg \Gamma_h^{\mathrm{th},e}$, we can find $\Gamma_e^{\mathrm{th},e}$ by comparing $\Gamma_e(\omega - eV_{e_+}^{\mathrm{th}})$ to the $\omega - \epsilon_0$ term in the resonance denominator of Eq. (7.38). This yields $\Gamma_{e,2}^{\mathrm{th},e} \sim (\gamma_e^2\Delta)^{1/3}$, and Eq. (7.38) gives the peak differential conductance

$$\left.\frac{\mathrm{d}I}{\mathrm{d}V}\right|_{\mathrm{peak},+} \sim \frac{2e^2}{h}\frac{\Gamma_h^{\mathrm{th},e}}{\Gamma_{e,2}^{\mathrm{th},e}} \sim \frac{2e^2}{h}\frac{\gamma_h \Delta^{1/6}}{\gamma_e^{2/3}\epsilon_0^{1/2}}. \tag{7.45}$$

Analogous considerations apply to negative bias voltages near the threshold $eV_{h_-}^{\mathrm{th}} = -(\Delta + \epsilon_0)$, where the hole tunneling rate becomes singular at threshold while the electron tunneling rate $\Gamma_e^{\mathrm{th},h} = \gamma_e(\Delta/4\epsilon_0)^{1/2}$ remains regular, see Fig. 7.1(b). When electron tunneling dominates, $\Gamma_e^{\mathrm{th},h} \gg \Gamma_h^{\mathrm{th},h}$, we find the characteristic hole tunneling rate $\Gamma_h^{\mathrm{th},h} \sim \gamma_h(\Delta/\Gamma_e^{\mathrm{th},h})^{1/2}$ and the peak differential conductance becomes

$$\left.\frac{\mathrm{d}I}{\mathrm{d}V}\right|_{\mathrm{peak},-} \sim \frac{2e^2}{h}\frac{\Gamma_h^{\mathrm{th},h}}{\Gamma_e^{\mathrm{th},h}} \sim \frac{2e^2}{h}\frac{\gamma_h \epsilon_0^{3/4}}{\gamma_e^{3/2}\Delta^{1/4}}. \tag{7.46}$$

If on the other hand, broadening is dominated by hole tunneling, $\Gamma_h^{\mathrm{th},h} \gg \Gamma_e^{\mathrm{th},h}$, we find $\Gamma_{h,2}^{\mathrm{th},h} \sim (\gamma_h^2\Delta)^{1/3}$ and

$$\left.\frac{\mathrm{d}I}{\mathrm{d}V}\right|_{\mathrm{peak},-} \sim \frac{2e^2}{h}\frac{\Gamma_e^{\mathrm{th},h}}{\Gamma_{h,2}^{\mathrm{th},h}} \sim \frac{2e^2}{h}\frac{\gamma_e \Delta^{1/6}}{\gamma_h^{2/3}\epsilon_0^{1/2}}. \tag{7.47}$$

In the presence of the high-frequency radiation, Eq. (7.38) exhibits photon-assisted sidebands in the differential conductance as reflected in the frequency arguments which are shifted by multiples of $\hbar\Omega$. The strength of these sidebands, set by the Bessel functions, oscillates as a function of V_{HF}. Moreover, the Bessel functions rapidly diminish as their argument becomes larger than their index, so that the sums over n and m – and thus the photon-assisted sidebands – are effectively restricted to the range $|n|, |m| < eV_{\mathrm{HF}}/\hbar\Omega$. These are the limits indicated in Fig. 7.3 by white (dashed and dotted) lines and reflect the fact that the tunneling electrons and holes can gain or lose at most eV_{HF} in energy due to the HF field.

Equation (7.38) also makes the separate thresholds for electron and hole tunneling explicit, which were underlying much of our discussion in Section 7.2. The tunneling rates $\Gamma_{e/h}$ are proportional to the BCS density of states with its onset of density of states at $\pm\Delta$. Using the resonance denominator in Eq. (7.38) to replace ω by the bound state energy ϵ_0 in the electron and hole tunneling rates $\Gamma_e(\omega-(eV+n\Omega))$ and $\Gamma_h(\omega+(eV+m\Omega))$, we read off thresholds at $eV = \pm\Delta + \epsilon_0 - n\Omega$ for electron tunneling and at $eV = \pm\Delta - \epsilon_0 - m\Omega$ for hole tunneling, in agreement with the results quoted in Section 7.2.

We now use Eq. (7.38) to analyze the strength of the photon-assisted sidebands more systematically. In the presence of the high-frequency radiation, the electron and hole tunneling rates split into photon-assisted sidebands, see Eq. (7.29). To understand the pattern of sidebands in the differential conductance, we assume that the broadening Γ is small compared to the photon energy Ω. Then, we can write the electron and hole tunneling rates as

$$\sum_n J_n^2\left(\frac{eV_{\mathrm{HF}}}{\hbar\Omega}\right)\Gamma_e(\omega-(eV+n\hbar\Omega)) \simeq \Gamma_{e,0} + \delta\Gamma_e(\omega), \tag{7.48}$$

$$\sum_m J_m^2\left(\frac{eV_{\mathrm{HF}}}{\hbar\Omega}\right)\Gamma_h(\omega+(eV+m\hbar\Omega)) \simeq \Gamma_{h,0} + \delta\Gamma_h(\omega). \tag{7.49}$$

Here, $\Gamma_{e,0}$ and $\Gamma_{h,0}$ denote the contributions of all nonresonant sidebands which are independent of ω to leading order, while $\delta\Gamma_e(\omega)$ and $\delta\Gamma_h(\omega)$ are the ω-dependent contributions of the resonant sidebands. The distribution of weight over sidebands implies that with one exception discussed below, we can typically neglect the contribution of $\delta\Gamma_e(\omega)$ and $\delta\Gamma_h(\omega)$ to the broadening in the denominator of Eq. (7.38). Similarly, we need to retain the contribution of a resonant sideband in the numerator to obtain a nonzero contribution to the differential conductance. (Recall that the Fermi functions as well as $\Gamma_{e,0}$ and $\Gamma_{h,0}$ are essentially independent of bias voltage.) With these considerations, we obtain the estimate

$$\left.\frac{\mathrm{d}I}{\mathrm{d}V}\right|_{\mathrm{peak}} \sim \frac{2e^2}{h}\frac{\Gamma_{e,0}\delta\Gamma_h^{\mathrm{th}} + \Gamma_{h,0}\delta\Gamma_e^{\mathrm{th}}}{(\Gamma_{e,0}+\Gamma_{h,0})^2}, \tag{7.50}$$

where $\delta\Gamma^{\mathrm{th}}_{e/h}$ is given by evaluating $\delta\Gamma_{e/h}(\omega)$ within $\Gamma_{e,0}+\Gamma_{h,0}$ of the resonance.

When $|u|^2 = |v|^2$, we have, in magnitude, $\Gamma_{e,0} \approx \Gamma_{h,0}$ and $\delta\Gamma^{\mathrm{th}}_{e} \approx \delta\Gamma^{\mathrm{th}}_{h}$. We then expect electron and hole sidebands to have comparable strengths and we find a peak conductance of order

$$\left.\frac{\mathrm{d}I}{\mathrm{d}V}\right|_{\mathrm{peak}} \sim \frac{2e^2}{h}\frac{\delta\Gamma^{\mathrm{th}}_{e/h}}{\Gamma_{e,0}+\Gamma_{h,0}}. \tag{7.51}$$

Here, we assume for simplicity that the electron and hole sidebands are not overlapping when writing the numerator. This situation corresponds to the central column of Figure 7.3, where one can see both electron and hole sidebands within their respective V-shapes but always restricted to the outer V-shape at both negative and positive bias. Next consider asymmetric electron and hole wave functions, say $|u|^2 \ll |v|^2$. Then, $\Gamma_{e,0} \ll \Gamma_{h,0}$, and Eq. (7.50) reduces to

$$\left.\frac{\mathrm{d}I}{\mathrm{d}V}\right|_{\mathrm{peak}} \sim \frac{2e^2}{h}\left[\frac{\Gamma_{e,0}\delta\Gamma^{\mathrm{th}}_{h}}{\Gamma^2_{h,0}} + \frac{\delta\Gamma^{\mathrm{th}}_{e}}{\Gamma_{h,0}}\right]. \tag{7.52}$$

At first sight, the first term in the square brackets is suppressed because of the additional factor $\Gamma_{e,0}/\Gamma_{h,0}$. However, the asymmetry between the electron and hole wave functions also implies $\delta\Gamma^{\mathrm{th}}_{h} \gg \delta\Gamma^{\mathrm{th}}_{e}$, so that the two terms in the square brackets are of the same order as they stand. However, the first term is indeed suppressed since the denominator also includes the resonant contributions. For $|u|^2 \ll |v|^2$, these are dominated by $\delta\Gamma_h(\omega)$. This contribution thus suppresses the sidebands of the numerator due to $\delta\Gamma_h$. We can then indeed neglect the first term in square brackets and obtain

$$\left.\frac{\mathrm{d}I}{\mathrm{d}V}\right|_{\mathrm{peak}} \sim \frac{2e^2}{h}\frac{\delta\Gamma^{\mathrm{th}}_{e}}{\Gamma_{h,0}}. \tag{7.53}$$

This explains why hole sidebands are suppressed relative to electron sidebands and thus the appearance of the Y-shaped pattern at negative bias voltages as well as the appearance of only a single (electron) set of sidebands at positive bias voltages. This is the situation corresponding to the Y-shape of the left-most column in Figure 7.3, where only the electron sidebands within the outer V-shape are visible (in addition to the Y-shape stem sidebands). Similarly, when $|v|^2 \ll |u|^2$, we have $\Gamma_{h,0} \ll \Gamma_{e,0}$, and we find

$$\left.\frac{\mathrm{d}I}{\mathrm{d}V}\right|_{\mathrm{peak}} \sim \frac{2e^2}{h}\frac{\delta\Gamma^{\mathrm{th}}_{h}}{\Gamma_{e,0}}, \tag{7.54}$$

so that hole sidebands are dominant. This is the situation corresponding to the Y-shape of the right-most column in Figure 7.3. We finally note that these results imply that the sidebands reduce in strength as electron and hole wave function become more asymmetric, in agreement with Figure 7.3.

Equation (7.38) also includes the effects of the real part Λ of the self energy. It is interesting to note that in the absence of the ac field, the real part does not contribute. Indeed, without ac field, the self energy is either purely real or purely imaginary. Current only flows when both imaginary parts Γ_e and Γ_h are nonzero, and consequently, $\Lambda(\omega)$ does not contribute. The situation is different in the presence of the ac field, since now the imaginary parts must only be nonzero when absorbing or emitting certain numbers of photons. Contributions to the self energy when absorbing or emitting a different number of photons can still be real and contribute to the resonance denominator in the expression for the current.

Our calculation assumes that we can retain only the contribution of the YSR bound state to the substrate Green function. This requires that the tip-induced broadening of the YSR state remains small compared to the superconducting gap. The characteristic magnitude of the tip density of states is given by the normal-state density of states ν_0 and the YSR wave function at the tip position is of order $|u|^2, |v|^2 \sim \nu_0\Delta$ [PGO13]. This yields the estimate $|t|^2\nu_0^2\Delta$ for the broadening of the YSR state. Our approximation for the substrate Green function is thus accurate as long as $\nu_0|t| \ll 1$. In view of the normal-state tunneling conductance of the junction, $G_T = (2e^2/h)4\pi^2(\nu_0|t|)^2$, this is equivalent to the condition $G_T \ll 2e^2/h$.

7.4.2 EXACT TREATMENT

i) DERIVATION

We now consider the exact self energy (setting again $\hbar = 1$)

$$\begin{aligned}\Sigma_R(\tau,\tau') = |t|^2 \sum_{n,m} & J_n(eV_{\mathrm{HF}}/\Omega) J_m(eV_{\mathrm{HF}}/\Omega) \\ & \times e^{-i(eV+n\Omega)\tau\tau_z} g_L(\tau-\tau') e^{i(eV+m\Omega)\tau'\tau_z}.\end{aligned} \tag{7.55}$$

including the nondiagonal contribution. In frequency representation defined through

$$\Sigma_R(\tau,\tau') = \int \frac{\mathrm{d}\omega}{2\pi}\frac{\mathrm{d}\omega'}{2\pi} e^{-i\omega\tau + i\omega'\tau'} \Sigma_R(\omega,\omega'), \tag{7.56}$$

this becomes

$$\begin{aligned}\Sigma_R(\omega,\omega') = |t|^2 \sum_{n,m} & J_n(eV_{\mathrm{HF}}/\Omega) J_m(eV_{\mathrm{HF}}/\Omega) \\ & \times 2\pi\delta(\omega - \omega' - (n-m)\Omega\tau_z) g_L(\omega - (eV+n\Omega)\tau_z).\end{aligned} \tag{7.57}$$

As this is nonzero only when the frequency arguments ω and ω' differ by multiples of Ω, we can write

$$\Sigma_R(\omega,\omega') = \sum_m 2\pi\delta(\omega-\omega'-m\Omega)\Sigma_m(\omega') \tag{7.58}$$

with

$$\Sigma_m(\omega) = \sum_n J_n \begin{bmatrix} J_{n+m} g_L(\omega_{-,n}) & 0 \\ 0 & J_{n-m} g_L(\omega_{+,n}) \end{bmatrix}. \tag{7.59}$$

Here, we temporarily omitted the arguments of the Bessel functions and introduced $\omega_{\pm,n} = \omega \pm (eV + n\Omega)$ for compactness. We also note that the self energy satisfies the relation

$$\Sigma_{-m}(\omega + m\Omega) = \Sigma_m(\omega), \tag{7.60}$$

which can be confirmed using the explicit expression (7.59).

Iteration of the Dyson equation $G_R = g_R + g_R\Sigma_R G_R$ implies that the Green function $G_R(\omega,\omega')$ is also nonzero only when its frequency arguments ω and ω'

differ by multiples of Ω. Thus, we define

$$G_R(\omega,\omega') = \sum_m 2\pi\delta(\omega-\omega'-m\Omega)G_m(\omega') \tag{7.61}$$

with

$$G_R(\tau,\tau') = \sum_n \int \frac{\mathrm{d}\omega}{2\pi} e^{-i\omega(\tau-\tau')-in\Omega\tau} G_n(\omega). \tag{7.62}$$

Inserting Eqs. (7.58) and (7.61) into the Dyson equation, we find

$$\begin{aligned} G_n(\omega) &= g_R(\omega)\delta_{n,0} \\ &\quad + \sum_m g_R(\omega+n\Omega)\Sigma_{n-m}(\omega+m\Omega)G_m(\omega), \end{aligned} \tag{7.63}$$

which provides a set of linear equations to compute the $G_n(\omega)$.

Writing the current in Eq. (7.20) using Eqs. (7.58) and (7.61) and focusing on the dc contribution, we find

$$\begin{aligned} I_{\mathrm{dc}} &= \int \frac{\mathrm{d}\omega}{2\pi} \sum_n \mathrm{Tr}\Big\{\tau_z \\ &\times \left[G_n^<(\omega)\Sigma^a_{-n}(\omega+n\Omega) + G_n^r(\omega)\Sigma^<_{-n}(\omega+n\Omega)\right. \\ &\left.-\Sigma_n^<(\omega)G^a_{-n}(\omega+n\Omega) - \Sigma_n^r(\omega)G^<_{-n}(\omega+n\Omega)\right]\Big\}. \end{aligned} \tag{7.64}$$

This can be made more compact by using Eq. (7.60),

$$\begin{aligned} I_{\mathrm{dc}} = \int \frac{\mathrm{d}\omega}{2\pi} \sum_n \mathrm{Tr}\Big\{\tau_z &\left[G_n^<(\omega)\Sigma^a_n(\omega) + G_n^r(\omega)\Sigma^<_n(\omega)\right. \\ &\left.-\Sigma_n^<(\omega)G^a_n(\omega) - \Sigma_n^r(\omega)G^<_n(\omega)\right]\Big\}. \end{aligned} \tag{7.65}$$

Together with the expressions (7.59) and (7.63) for the self energy and the Green function, respectively, this constitutes our final result.

ii) RESULTS

We solve Eq. (7.63) numerically by truncating the system of equations at a sufficiently high $|n| \gg V_{\mathrm{HF}}/\Omega$ and compute the current from Eq. (7.65). Due to the terms of the self energy which are off-diagonal in frequency, the exact solution is sensitive to Green functions which are evaluated at frequencies shifted by integer multiples of the photon energy. This suggests that the exact solution deviates from the diagonal approximation when the tunneling-induced broadening of the Green functions becomes of the order of or larger than the photon energy. Conversely, the diagonal approximation is expected to be accurate in the limit of small broadening and well-resolved photon sidebands.

Figure 7.6 compares representative numerical results obtained in the diagonal approximation and the numerically exact solution. The results consider the parameter regime $u^2 = v^2/9$ where the Y-shape appears at negative voltages. The choice of $V_{\mathrm{HF}}/\Omega = 2$ implies that the resonances at negative voltages are associated with the lower part (stem) of the Y-shape. Panel (a) shows both negative and positive voltages for strong tunneling-induced broadening. At positive biases, we find that the sidebands are no longer well resolved due to the broadening and the differences between the diagonal approximation and exact result are largely quantitative. The self energy already present in the diagonal approximation, including the hole contribution to the broadening, dominates

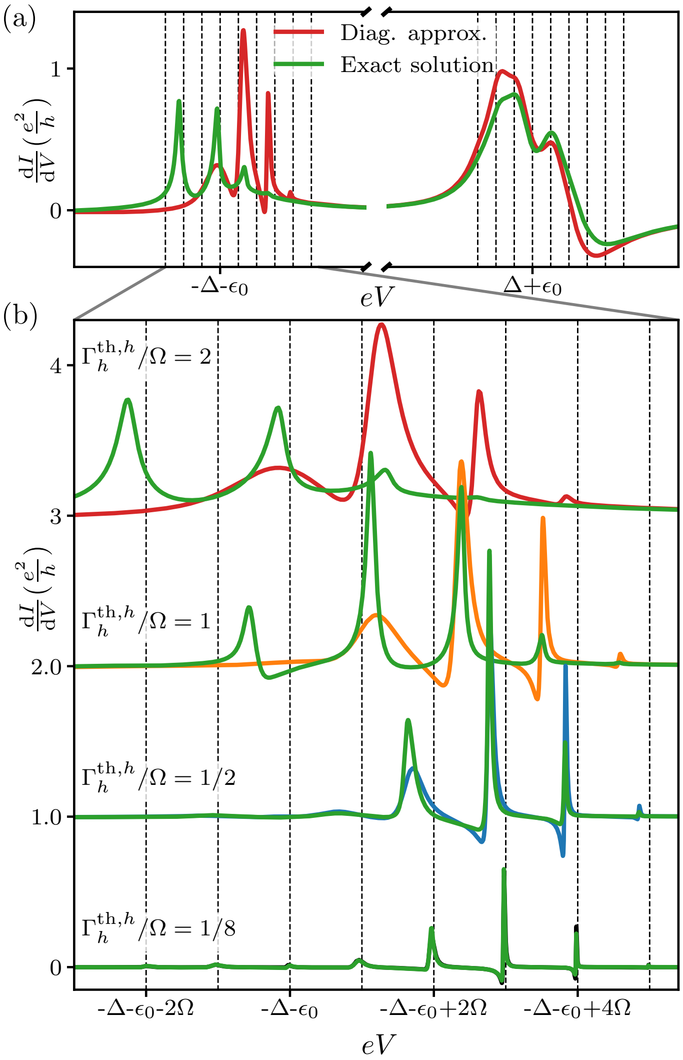

FIGURE 7.6: Comparison between diagonal approximation (different colors) and the exact solution (green) for $\epsilon_0/\Delta = 0.4$, $\Omega/\Delta = 0.025$ and $u^2 = v^2/9$. (a) $\mathrm{d}I/\mathrm{d}V$ at negative and positive voltages at strong tip-sample tunneling ($\Gamma_h^{\text{th},h} = 2\Omega$). The resonances at negative bias voltages are shifted relative to the diagonal approximation, while the differences are merely quantitative at positive biases. (b) Closeup of threshold region at negative bias voltages region for increasing tip-sample tunneling $\Gamma_h^{\text{th},h}$ as indicated in the figure (from bottom to top; offset for clarity). The differences between exact solution (green) and diagonal approximation become substantial once $\Gamma_h^{\text{th},h}$ becomes comparable to the photon energy Ω. Dashed lines indicate multiples of the photon energy Ω.

over additional contributions in the exact solution. In contrast, we find distinct differences at negative voltages: Here, the hole contribution to the broadening is still suppressed around the threshold voltage along the stem of the Y-shape and the resonances remain well resolved. One then observes that the sidebands are distinctly shifted to higher bias voltages in the exact solution, while the width of the resonances remains essentially unchanged, i.e., the dominant effect is associated with the real part of the self energy.

Panel (b) explores the dependence on the strength of tip-substrate tunneling, focusing on the region of negative voltages. We quantify the four different strengths of tip-substrate tunneling by the threshold value for the hole tunneling rate

$$\Gamma_h^{\mathrm{th},h} = \frac{1}{2}\left(\gamma_h^2\Delta\right)^{1/3}, \tag{7.66}$$

as evaluated for the regime of dominant hole tunneling. For weak tip-substrate tunneling, $\Gamma_h^{\mathrm{th},h}/\Omega = 1/8$, the brodening is small compared to the photon energy and in agreeement with expectations, the diagonal approximation is essentially identical to the exact solution. For $\Gamma_h^{\mathrm{th},h}/\Omega = 1/2$, quantitative differences such as modified peak heights begin to appear, but the peak positions still remain identical. The differences become more pronounced for $\Gamma_h^{\mathrm{th},h}/\Omega = 1$ and $\Gamma_h^{\mathrm{th},h}/\Omega = 2$, where we observe substantial shifts of the peaks to higher bias voltages. Also note that the resonance width grows with increasing $\Gamma_h^{\mathrm{th},h}/\Omega$ as expected. These results show that the diagonal approximation is accurate in the regime of highly resolved sidebands.

We finally point out that the diagonal approximation is exact for a normal-state tip with a constant density of states ν_0. In this case, the retarded and advanced self energies in Eq. (7.19) are purely imaginary,

$$\Sigma_R^{r,a}(\tau,\tau') = \mp i\pi|t|^2\nu_0\delta(\tau-\tau'), \tag{7.67}$$

and independent of the ac field. This makes also the retarded and advanced substrate Green functions independent of the ac field, so that $\Sigma_n^{r,a}$ is nonzero for $n=0$ only,

$$\Sigma_{n=0}^{r,a}(\omega) \quad = \quad \mp i\pi|t|^2\nu_0. \tag{7.68}$$

Then, $G_n^{r,a}$ is nonzero for $n=0$ only and only the $n=0$ term contributes to the dc current in Eq. (7.65). Moreover, one readily ascertains from the Dyson equation (7.63) and the Langreth rules that the $n=0$ components satisfy a closed set of equations which is just the set of equations which leads to the diagonal approximation.

7.5 MAJORANA BOUND STATES

7.5.1 BASIC RESULTS

Our considerations for YSR states apply to photon-assisted tunneling into Majorana bound states with only minor modifications. First, Majorana bound states have zero energy so that we set $\epsilon_0 = 0$. Second, their electron and hole wave functions are equal in magnitude, satisfying $u = v^*$ for spinless fermions (and corresponding expressions for spinful electrons in a four-component Nambu formalism). Finally, an isolated Majorana bound state is a solution of the particle-hole symmetric Bogoliubov-de Gennes equation which doubles the degrees of freedom. Due to this doubling of degrees of freedom, the expression

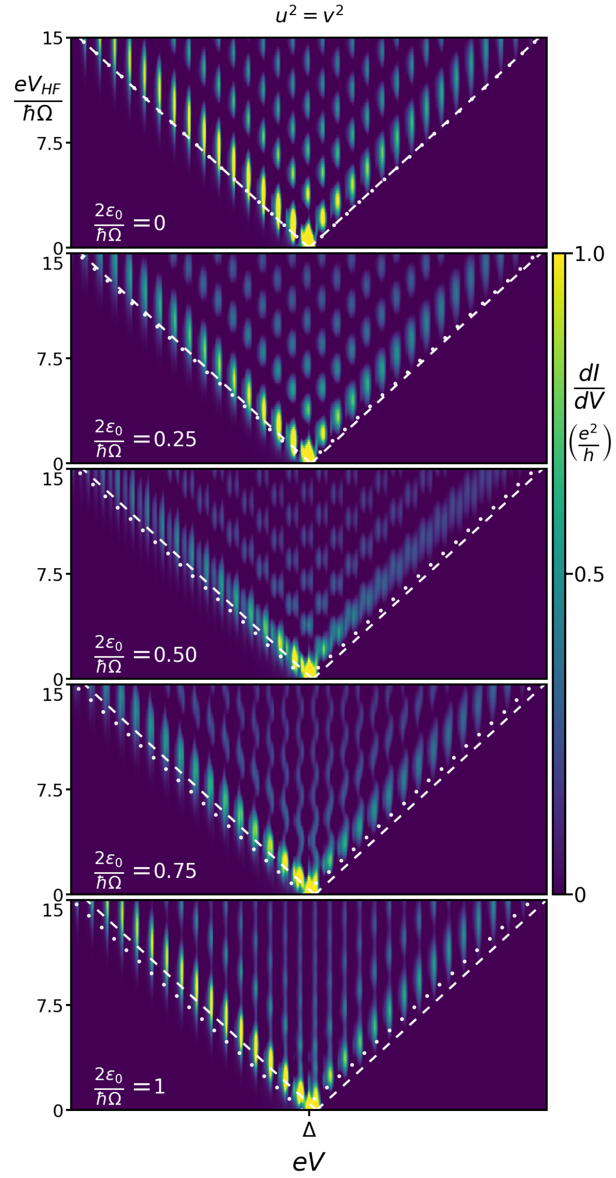

FIGURE 7.7: Differential conductance (color scale) as a function of bias voltage eV and amplitude eV_{HF} of the high-frequency radiation for tunneling into a YSR state with equal electron and hole wave functions, $|u|^2 = |v|^2$ and small YSR energies ϵ_0 increasing from zero to $\hbar\Omega/2$ from top to bottom as indicated in the panels. The regions with electron and hole sidebands are indicated by white dashed and dotted lines, respectively. The five panels show clearly that a nonzero energy of the YSR state generates a splitting of the photon-assisted sidebands which appears with high multiplicity throughout the V-shaped region. This provides the basis for a high-resolution measurement of the energy of the subgap state, which can be used to identify YSR (or Andreev) bound states with near-zero energy ϵ_0 with high resolution, and thereby distinguish them from Majorana bound states. Parameters: $\Omega/\Delta = 0.05$, $\nu_0|t| = 0.04$.

for the current must be multiplied by a factor of $1/2$ relative to the case of a YSR state.

First consider photon-assisted resonant Andreev processes into Majorana bound states from a normal-metal tip. Using these translation rules, we obtain corresponding results directly from the results for YSR states given in Section 7.4.1.ii. The equal magnitude of electron and hole wave functions makes the peak conductance universal and equal to $2e^2/h$ for Majorana bound states [LLN09; Fle10]. This corresponds to half of the maximal peak conductance of a zero-energy YSR state, reflecting that Majorana bound states are effectively only half of an ordinary subgap state.

In the presence of high-frequency radiation, there are photon-assisted sidebands and, reinstating again Plank's constant, one obtains from Eq. (7.41) that

$$\frac{\mathrm{d}I}{\mathrm{d}V} = \frac{2e^2}{h} \sum_n J_n^2(eV_{\mathrm{HF}}/\hbar\Omega) \frac{\gamma^2}{(eV + n\hbar\Omega)^2 + \gamma^2}, \tag{7.69}$$

where we introduced $\gamma = \gamma_e = \gamma_h$. Thus, the familiar Majorana zero-bias peak of height $2e^2/h$ splits into photon sidebands with a sideband spacing in bias voltage of $\hbar\Omega/e$. As for YSR states, this can be traced back to the existence of separate threshold conditions for electrons and holes. For Majorana bound states, these two sets of conditions coincide by particle-hole symmetry, leading to a sideband spacing of $\hbar\Omega/e$ seemingly indicating single-electron tunneling despite the underlying resonant Andreev process.

For a superconducting tip, we focus on the limit of well-resolved sidebands where the diagonal approximation (7.38) is accurate and obtain

$$\begin{aligned} I = e\,\mathrm{sgn}(V) \int \frac{\mathrm{d}\omega}{2\pi} \sum_{n,m} & J_n^2(eV_{\mathrm{HF}}/\Omega) J_m^2(eV_{\mathrm{HF}}/\Omega) \\ & \times \frac{\Gamma_e(\omega - (eV + n\Omega))\Gamma_h(\omega + (eV + m\Omega))}{[\omega - \epsilon_0 - \Lambda(\omega)]^2 + \frac{1}{4}\Gamma^2(\omega)}, \end{aligned} \tag{7.70}$$

where $\Gamma_e(\omega)$ and $\Gamma_h(\omega)$ are now evaluated with $|u|^2 = |v|^2$ and thus equal. Up to an overall scale factor of $1/2$, the result is identical to that for a YSR state with $\epsilon_0 = 0$ and $|u|^2 = |v|^2$ as shown in the top panel in Fig. 7.7. For $\epsilon_0 = 0$, the V-shapes for the electron and hole conditions coincide and are centered on $eV = \pm\Delta$. This also implies that similar to the case of a normal-state tip, there is only one set of sidebands with spacing $\hbar\Omega$ which is enhanced by the fact that electron and hole resonances coincide. While the pattern of resonances at $eV = \pm\Delta$ is necessarily symmetric with respect to a change of sign of the bias voltage, the individual V-shapes are asymmetric about $eV = \Delta$ (or, analogously, $eV = -\Delta$). This is a consequence of the fact that the broadening is smaller on the small-bias side of the V shape, leading to sharper features and a larger differential conductance (see Fig. 7.7; this is not properly reflected by the color scale in Fig. 7.8 due to saturation effects).

7.5.2 MAJORANA VS. YSR STATES

It is frequently a challenge to distinguish zero-energy Majorana bound states from other low-energy subgap states. Moreover, in many experiments, putative Majorana states might be accompanied by close-lying YSR states [NP+14; Rub+15a; Fel+17; Kim+18; Sch+20]. Our results on YSR and Majorana bound states imply that photon-assisted tunneling provides a high-resolution method to determine the energy of subgap states. In principle, superconducting tips are

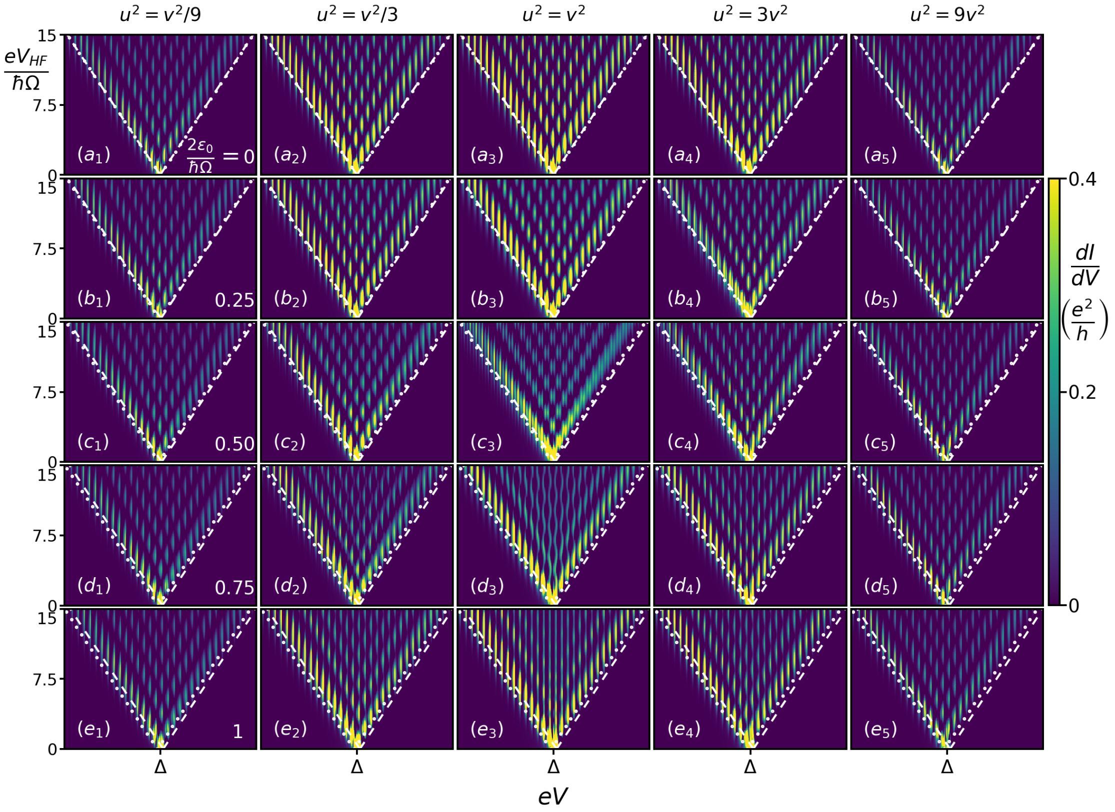

FIGURE 7.8: Differential conductance (color scale) as a function of bias voltage eV and amplitude eV_{HF} of the high-frequency radiation for tunneling into YSR state into a YSR state with various ratios of electron and hole wave functions and small YSR energies ϵ_0 increasing from zero to $\hbar\Omega/2$ from top to bottom, as indicated in the panels. The regions with electron and hole sidebands are indicated by white dashed and dotted lines, respectively. The splitting of the sidebands due to a small nonzero energy ϵ_0 appearing for equal electron and hole wave functions (central column of panels) are less pronounced for asymmetric electron and hole wave functions. For YSR states, the ratio of electron and hole wave functions typically varies as a function of position. In STM experiments, one can therefore generically choose a tip position for which electron and hole wave functions have similar magnitude. Parameters: $\Omega/\Delta = 0.05$, $\nu_0|t| = 0.04$.

preferable over normal-metal tips because the gap suppresses thermal excitations and the strongly peaked BCS density of states allows for high energy resolution. At the same time, $\mathrm{d}I/\mathrm{d}V$ peaks due to subgap states with a zero or small energy ϵ_0 no longer appear as (near) zero-bias peaks, but rather at $eV = \Delta + \epsilon_0$ [NP+14; Rub+15a; Fel+17]. Thus, the small energy ϵ_0 of the bound states is effectively extracted as a difference of two much larger energies, $\Delta + \epsilon_0$ and Δ. In particular, this implies that inaccuracies in the determination of the tip gap carry over fully into the accuracy with which the bound state energy can be determined.

The existence of independent thresholds for electrons and hole tunneling in photon-assisted resonant Andreev reflections provides a method to extract the bound state energy from a line splitting which appears directly in the measured tunneling spectra [Pet+20]. Moreover, this line splitting appears with a high multiplicity throughout the V-shaped region within which one observes thresholds for photon-assisted tunneling. To illustrate this, consider first resonant Andreev reflections into a YSR state with equal electron and hole wave functions and a small energy ϵ_0, as shown in Fig. 7.7. Up to an overall prefactor of $1/2$, the panel for $\epsilon_0 = 0$ is identical to the result for a Majorana bound state. One observes that even a small ϵ_0 which is just a fraction of the photon energy $\hbar\Omega$ leads to a splitting of the sidebands and can thus be accurately detected. This is most evident for $\epsilon_0 = \hbar\Omega/4$, making experiments with variable photon energies particularly advantageous.

In addition to the line splitting, there is also a characteristic change in the dependence of the sideband strengths as a function of the amplitude V_{HF} of the high-frequency radiation. As seen in Fig. 7.7 and Fig. 7.8, the sideband strengths exhibit repeated zeros as a function of V_{HF}. The zeros originate from the oscillations of the Bessel functions in Eq. (7.38). Physically, these can be considered a result of interference between various sequences of emissions and absorptions of 'photons' contributing to a sideband. (Notice that the sideband strength is nonperturbative in V_{HF} and emerges from processes of all orders when viewed from the point of view of perturbation theory.) Different sidebands are controlled by Bessel functions of different order, and the corresponding phase shift leads to a shift in the locations of the zeros between neighboring sidebands.

The behavior of the zeros in Figs. 7.7 then emerges as follows. The separate thresholds for electron and hole tunneling coincide for $\epsilon_0 = 0$, but move apart when ϵ_0 becomes nonzero. When $\epsilon_0 = 0$, a particular sideband 'combines' electron and hole sidebands described by Bessel functions of the same order, and the zeros of the Bessel functions are preserved. For $2\epsilon_0 = \hbar\Omega$, the electron and hole sidebands are described by Bessel functions of neighboring orders. Their zeros no longer coincide and thus the zeros in the observed sideband strengths disappear. This allows one to distinguish true zero-energy states from situations with nonzero ϵ_0 in which electron and hole sidebands coincide because $2\epsilon_0$ and $\hbar\Omega$ are commensurate.

Corresponding results with unequal electron and hole wave functions are shown in Fig. 7.8. Clearly, the splitting due to a small ϵ_0 is most pronounced for equal electron and hole wave functions, for which sidebands emerging from electron and hole sidebands are both equally prominent, as discussed in Section 7.4.1.iii. For a YSR state, the ratio of electron and hole wave functions varies as a function of position. In STM experiments, one should thus choose a tip position where electron and hole wave functions are equal to optimize sensitivity. Finally, notice that the modulations of the sideband strength as a function of V_{HF} reemerge even for $2\epsilon_0 = \hbar\Omega$ once electron and hole wave functions are sufficiently different. In this case, the electron and hole thresholds contribute with different strengths, and the sidebands are dominated by one or the other.

7.6 CONCLUSION

We have developed a theory for photon-assisted resonant Andreev tunneling into subgap states in superconductors. Our results are in excellent agreement with recent STM measurements on YSR states [Pet+20], fully reproducing the observed patterns of sidebands which differ markedly from predictions of a simple Tien-Gordon-like theory.

A central aspect of the theory are independent sideband conditions for the electron and hole tunneling processes. This leads to two sets of sidebands whose relative shift in bias voltage depends on the ratio of the energy of the subgap state and the photon energy. As an interesting consequence, this provides a sensitive technique to measure near-zero energies of subgap states. In the context of topological states of matter this can be instrumental in distinguishing conventional subgap states from Majorana bound states. Simultaneous visibility of the two sets of sidebands is optimal when electron and hole wave functions are of similar magnitude. For YSR states, the ratio of electron and hole wave functions typically varies widely with lateral position [Yaz+97; Mén+15; Rub+16; Cho+17]. This can be exploited in STM experiments by choosing an appropriate lateral position of the STM tip for optimal resolution. The absence of spatial resolution may make this technique less flexible in transport experiments using gate defined tunnel junctions.

The observability of the photon-assisted sidebands of resonant Andreev reflections is constrained by two requirements. On the one hand, tunneling should be sufficiently weak for the tunneling-induced broadening to be small compared to the sideband spacing so that the sidebands are well resolved. At the same time, the underlying resonant Andreev reflections require tunneling to be fast compared to inelastic relaxation processes. The latter provide competing channels which transfer electrons into the quasiparticle continuum of the substrate via the subgap state and which transfer only a single electron between tip and substrate. The experiment of Ref. [Pet+20] shows that these conditions on the junction conductance can be simultaneously satisfied at a temperature of order 1K using a photon frequency of 40 GHz. Since inelastic excitations have an activated temperature dependence, their rate drops rapidly as temperature is lowered. This implies that even though the broadening of the sidebands is independent of temperature, the attainable resolution of small subgap energies improves rapidly at lower temperatures.

In view of recent experiments, we focus on YSR states. However, we emphasize that our theoretical approach is in no way specific to YSR states and applies equally well to other subgap states. Consequently, photon-assisted tunneling could also contribute to distinguishing Andreev from Majorana bound states. At present, our theory assumes a single subgap state. Magnetic impurities frequently induce multiple subgap states within the superconducting gap [Ji+08; Rub+16; Cho+17; Hat+15]. It would thus be interesting to extend the theory to include several subgap states where one would expect additional spectroscopic features to arise when the photon energy becomes comparable to the level spacing between subgap states.

8 | CONCLUSION

This thesis provides theoretical frameworks and calculations to explain three different experiments. While each of them are interesting pieces of research within their own context, the three of them are of relevance in the context of topological state engineering. One can distinguish two branches in this field: one focusing on the engineering of basic physical phenomena to realize topological states of matter, such as Majorana quasiparticles, and a second aiming at the use of topological states of matter to engineer systems of interest. The goal of realizing a quantum computer is the paradigmatic example of such systems and has motivated much scientific effort.

Chapters 2 and 3 introduced basic physical concepts, which are necessary to understand the work presented in this thesis. Among these we highlight: the bulk-boundary correspondence, the recipe to engineer topological superconductivity from Zeeman splitting, spin-orbit coupling and s-wave superconductivity, the physics of magnetic impurities on superconducting substrates leading to Yu-Shiba-Rusinov states, and their signatures in STM measurements.

In Chapter 4, we proposed a theoretical toy model to understand and study the physics of two recent experiments with graphene nanoribbons. These experiments engineered an effective Su-Schrieffer-Heeger (SSH) model from topological boundary states arising at the domain walls of nanoribbons of different widths, predicted to be in distinct topological phases. Our toy model, based on the original SSH model itself, reproduces this behavior through a spatially dependent dimerization parameter. Indeed, the boundary states at the domain walls between distinct topological regions are engineered to develop couplings of alternating strengths among one another, thus realizing an effective SSH of their own. We studied the different possible end state configurations of the model, revealing the interplay between the microscopic and the emergent SSH end states. The model admits a "butterfly" representation, which provides a compact representation of its properties. The graphene nanoribbon experiments, together with our work, constitute a first step in the engineering of more complex systems using topological boundary states as building blocks. It will be interesting to see how this field develops in the coming years.

Chapter 5 presents the first study of the effect of a charge density wave on the wave function and energy of a YSR state. Having sparked interest as a substrate for the realization of magnetic adatom chains hosting Majorana quasiparticles, $NbSe_2$ exhibits a charge-density wave (CDW) order coexisting with superconductivity. For the engineering of a topological superconductor from YSR states, one needs to achieve sufficiently strong coupling among them. The quasi two-dimensional character of 2H-$NbSe_2$ makes it a good candidate, as YSR wave functions have a greater spatial extent than in conventional three-dimensional superconductors. Nevertheless, our study shows that it is crucial to take into account the effects of the CDW on the YSR state. There are two main reasons: first the CDW affects the energy of the YSR state and these couple more strongly if they have similar energies when separated, and secondly, the CDW affects the wave function shape of the YSR state and can reduce or enhance its weight in specific directions of space. We thus find that a careful study of these effects is necessary for the optimal coupling of YSR states in an adatom chain. Preferably, the different adatoms should be placed in equivalent positions with respect to both the atomic lattice and the CDW modulation and along symmetry lines with significant weight of the YSR wave functions. Our theoretical model neglects various physical effects present in the experiment but, in spite of its simplicity, it explains the experimental results satisfactorily making our model in principle applicable to a wider range of adatoms and superconducting substrates.

Chapter 6 presented the results of a recent experiment on photon-assisted tunneling between superconducting leads. In this collaboration, we confirmed that the venerable Tien-Gordon theory successfully explains the experimental results for single-particle tunneling, Cooper pair transfer, and multiple Andreev reflections in pristine superconductors, and showed that it also applies to single-particle tunneling resonantly enhanced by a YSR state. In these cases the Tien-Gordon theory successfully predicts the intensity modulation of the conductance peaks as a function of the radiation amplitude as well as the spacing of the sidebands in bias voltage, both a signature of the amount of charge transferred in the underlying tunneling events. More interestingly, the experiment found a breakdown of this theory when the current though a YSR state is dominated by resonant Andreev reflections. These two-particle processes lead to sidebands spaced as would correspond to single-particle tunnelings in the Tien-Gordon theory. Moreover, the conductance measurements showed previously unseen sideband structures forming a Y-shape. We explained how the individual threshold conditions for electron and hole tunneling, together with their dominance in the broadening of the resonance and the asymmetry in the weight of electron and hole YSR wave function explain these signatures. We showed how applying the Tien-Gordon approach to the individual tunneling rates, modifying the previously-known expressions for the tunneling current, reproduced the experimental measurements excellently.

Chapter 7 develops a full theory of photon-assisted Andreev tunneling resonantly enhanced by subgap states, motivated by the experiment of Chapter 6. Our theoretical framework provides a general picture for the photon-assisted resonant Andreev reflections, applicable to both normal and superconducting tips as well as to YSR states or other subgap states such as Majorana bound states. Our derivation includes the tunneling amplitude to all orders and confirms that individual threshold conditions for the electron and hole tunneling rates play a crucial role in explaining the deviations from the Tien-Gordon approach. We find that a frequency-local (diagonal) approximation of our full theory is in excellent agreement for typical experimental parameters. This approximation is valid as long as the broadening of the resonance remains small compared to the photon energy. Our results show the potential of photon-assisted tunneling as a technique to measure small but non-zero energies of the subgap states. Indeed, the position of the sidebands are directly related of the subgap state energy and the photon energy, allowing a more accurate measurement of the subgap state energy than previous methods. In the context of topological state engineering, this can be instrumental to distinguish conventional subgap states from the sought-for Majorana quasiparticles.

Appendix A

TIP GREEN FUNCTION

In this appendix, we briefly review the derivation of the tips Green function used in Chapter 7. The Nambu Green function g of a BCS superconductor (in the absence of tunneling or a magnetic impurity) takes the form

$$g_L(\mathbf{k}, \omega) = [\omega - \xi_{\mathbf{k}}\tau_z - \Delta\tau_x]^{-1}, \tag{A.1}$$

where τ_x and τ_z denote Pauli matrices in Nambu space. Performing the matrix inversion and computing the corresponding local Green function at the tip position yields

$$g_L(\omega) = \frac{1}{V}\sum_k g(\mathbf{k}, \omega) = \nu_0 \int \mathrm{d}\mathbf{k} \frac{\omega + \xi_{\mathbf{k}} + \Delta\tau_x}{\omega^2 - \xi_{\mathbf{k}}^2 - \Delta^2}. \tag{A.2}$$

Finally doing the integral gives the result

$$g_L(\omega) = -\frac{\pi\nu_0(\omega + \Delta\tau_x)}{\sqrt{\Delta^2 - \omega^2}}. \tag{A.3}$$

This can be used to find the retarded and advanced as well as lesser Green functions which are used throughout the main text.

The retarded and advanced Green functions are purely real at frequencies below the gap, $|\omega| < \Delta$, where one finds

$$g_L^{r/a}(\omega) = -\frac{\pi\nu_0(\omega + \Delta\tau_x)}{\sqrt{\Delta^2 - \omega^2}}, \tag{A.4}$$

and purely imaginary at frequencies above the gap, $|\omega| > \Delta$,

$$g_L^{r/a}(\omega) = \mp\frac{i\pi\nu_0(\omega + \Delta\tau_x)}{\sqrt{\omega^2 - \Delta^2}}\,\mathrm{sgn}(\omega). \tag{A.5}$$

To derive the lesser Green function, we use the relation

$$g_L^<(\omega) = -n_F(\omega)[g_L^r(\omega) - g_L^a(\omega)] \tag{A.6}$$

and obtain

$$g_L^<(\omega) = 2\pi i n_F(\omega)\frac{\nu_0(\omega + \Delta\tau_x)}{\sqrt{\omega^2 - \Delta^2}}\theta(|\omega| - \Delta)\mathrm{sgn}(\omega), \tag{A.7}$$

where $\theta(x)$ denotes the Heaviside function.

Within our calculation of the resonant Andreev reflections through subgap states in the substrate, neglecting Andreev reflections in the tip is equivalent to dropping the off-diagonal contributions to the tip Green function. In this approximation, $g_L(\omega)$ becomes proportional to the unit matrix in Nambu space and we find

$$g_L^{r/a}(\omega) \simeq \begin{cases} -\pi\nu_0 \frac{\omega}{\sqrt{\Delta^2-\omega^2}}, & |\omega| < \Delta \\ \mp i\pi\nu_0 \frac{|\omega|}{\sqrt{\omega^2-\Delta^2}}, & |\omega| > \Delta \end{cases} \tag{A.8}$$

for the retarded and advanced Green functions and

$$g_L^<(\omega) \simeq 2\pi i n_F(\omega) \frac{\nu_0|\omega|}{\sqrt{\omega^2-\Delta^2}}\, \theta(|\omega|-\Delta) \tag{A.9}$$

for the lesser Green function. The above-gap expressions can be expressed more compactly in terms of the BCS density of states in Eq. (7.32).

Appendix B

SUBSTRATE GREEN FUNCTION

This appendix discusses the Green function of the superconducting substrate of Chapter 7. We first consider the bare substrate Green function at subgap energies. In keeping with our approximation of neglecting the (nonresonant) Andreev reflections in the tip, we retain only the bound state contributions to the substrate Green function which are responsible for the resonant Andreev reflections. This approximation was derived in Section 3.2.1 where we wrote:

$$g_R(\omega) = \varphi \frac{1}{\omega - \epsilon_0} \varphi^\dagger \tag{B.1}$$

for the approximate subgap state contribution to the substrate Green function, where $\varphi = (u, v)^T$ at the tip position $\mathbf{R}$. (We assume here for simplicity that there is only one pair of YSR states.)

Tunneling introduces a self energy into the denominator of the retarded and advanced Green functions,

$$G_R^{r/a} = \varphi \frac{1}{\omega - \epsilon_0 - \tilde{\Sigma}_R^{0,r/a}} \varphi^\dagger \tag{B.2}$$

with

$$\tilde{\Sigma}_R^{0,r/a} = \varphi^\dagger \Sigma_R^{0,r/a} \varphi. \tag{B.3}$$

Note that we have written the last two expressions in general operator notation since with ac field, the self energy is generally no longer diagonal in frequency representation.

We also review a general relation for the lesser Green function (including the tunneling to the tip). Using the Langreth rules, the Dyson equation for G_R gives

$$G_R^< = g_R^< + g_G^r \Sigma_R^r G_R^< + g_G^r \Sigma_R^< G_R^a + g_G^< \Sigma_R^a G_R^a, \tag{B.4}$$

which can be readily shown to become

$$G_R^< = \frac{1}{1 - g_R^r \Sigma_R^r} g_R^< \frac{1}{1 - g_R^a \Sigma_R^a} + G_R^r \Sigma_R^< G_R^a. \tag{B.5}$$

The first term on the right-hand side vanishes generally as long as the system was noninteracting in the infinite past. Here, we can also use the explicit expression (A.6), with L replaced by R, to write

$$\begin{aligned} &\frac{1}{1 - g_R^r \Sigma_R^r} g_R^< \frac{1}{1 - g_R^a \Sigma_R^a} \\ &= -n_F(\omega) \frac{1}{1 - g_R^r \Sigma_R^r} [g_R^r - g_R^a] \frac{1}{1 - g_R^a \Sigma_R^a}. \end{aligned} \tag{B.6}$$

Inserting the identity

$$g_R^r - g_R^a = -2i\eta g_R^r g_R^a \tag{B.7}$$

with a positive infinitesimal η yields

$$\frac{1}{1-g_R^r\Sigma_R^r} g_R^< \frac{1}{1-g_R^a\Sigma_R^a} = 2i\eta n_F(\omega) G_R^r G_R^a = 0. \tag{B.8}$$

Thus, we find the identity

$$G_R^< = G_R^r \Sigma_R^< G_R^a. \tag{B.9}$$

REFERENCES

[Aas+16] D. Aasen et al. “Milestones Toward Majorana-Based Quantum Computing”. *Phys. Rev. X* 6.3 (2016). DOI: `10.1103/physrevx.6.031016`.

[AGO20] S. Acero González and F. von Oppen. “Topological Engineering in a Modulated Su-Schrieffer-Heeger Model”. *To be published* (2020).

[AG+20] S. Acero González, L. Melischek, O. Peters, K. Flensberg, K. J. Franke, and F. von Oppen. “Photon-assisted resonant Andreev reflections: Yu-Shiba-Rusinov and Majorana states”. *Phys. Rev. B* 102.4 (2020). DOI: `10.1103/physrevb.102.045413`.

[Ace+15] S. Acero, L. Brey, W. J. Herrera, and A. L. Yeyati. “Transport in selectively magnetically doped topological insulator wires”. *Phys. Rev. B* 92.23 (2015). DOI: `10.1103/physrevb.92.235445`.

[Ali12] J. Alicea. “New directions in the pursuit of Majorana fermions in solid state systems”. *Rep. Prog. Phys.* 75.7 (2012), p. 076501. DOI: `10.1088/0034-4885/75/7/076501`.

[And64] A. F. Andreev. “The thermal conductivity of the intermediate state in superconductors”. *Sov. Phys. JETP* 19.5 (1964), p. 1228.

[Arg+14] C. J. Arguello et al. “Visualizing the charge density wave transition in $2H$-NbSe$_2$ in real space”. *Phys. Rev. B* 89.23 (2014), p. 235115. DOI: `10.1103/PhysRevB.89.235115`.

[Arg+15] C. J. Arguello et al. “Quasiparticle Interference, Quasiparticle Interactions, and the Origin of the Charge Density Wave in $2H-$NbSe$_2$”. *Phys. Rev. Lett.* 114.3 (2015), p. 037001. DOI: `10.1103/PhysRevLett.114.037001`.

[Ata+13] M. Atala, M. Aidelsburger, J. T. Barreiro, D. Abanin, T. Kitagawa, E. Demler, and I. Bloch. “Direct measurement of the Zak phase in topological Bloch bands”. *Nat. Phys.* 9.12 (2013), pp. 795–800. DOI: `10.1038/nphys2790`.

[AA80] S. Aubry and G. André. “Analyticity breaking and anderson localization in incommensurate lattices”. *Ann. Israel Phys. Soc* 3 (1980), pp. 133–140.

[BVZ06] A. V. Balatsky, I. Vekhter, and J.-X. Zhu. “Impurity-induced states in conventional and unconventional superconductors”. *RPM* 78.2 (2006), p. 373. DOI: `10.1103/RevModPhys.78.373`.

[Baw+16] L. Bawden et al. “Spin-valley locking in the normal state of a tran-sition-metal dichalcogenide superconductor”. *Nat. Commun.* 7 (2016), p. 11711. DOI: `10.1038/ncomms11711`.

[Bee13] C. Beenakker. “Search for Majorana Fermions in Superconductors”. *Annu. Rev. Condens. Matter Phys.* 4.1 (2013), pp. 113–136. DOI: `10.1146/annurev-conmatphys-030212-184337`.

[Ber70] V. Berezinsky. "Destruction of long range order in one-dimensional and two-dimensional systems having a continuous symmetry group. I. Classical systems". *Zh. Eksp. Teor. Fiz.* 32 (1970), pp. 493–500.

[BHZ06] B. A. Bernevig, T. L. Hughes, and S.-C. Zhang. "Quantum Spin Hall Effect and Topological Phase Transition in HgTe Quantum Wells". *Science* 314.5806 (2006), pp. 1757–1761. DOI: `10.1126/science.1133734`.

[BH13] B. A. Bernevig and T. L. Hughes. *Topological insulators and topological superconductors*. Princeton university press, 2013.

[Ber84] M. V. Berry. "Quantal phase factors accompanying adiabatic changes". *Proc. R. Soc. Lond.* 392.1802 (1984), pp. 45–57. DOI: `10.1098/rspa.1984.0023`.

[Bli+95] R. H. Blick, R. J. Haug, D. W. Van Der Weide, K von Klitzing, and K Eberl. "Photon-assisted tunneling through a quantum dot at high microwave frequencies". *Appl. Phys. Lett.* 67 (1995), p. 3924. DOI: `10.1063/1.114406`.

[Boa+03] E. Boaknin et al. "Heat Conduction in the Vortex State of $\mathrm{NbSe_2}$: Evidence for Multiband Superconductivity". *Phys. Rev. Lett.* 90.11 (2003), p. 117003. DOI: `10.1103/PhysRevLett.90.117003`.

[Bor+09] S. V. Borisenko et al. "Two Energy Gaps and Fermi-Surface "Arcs" in $\mathrm{NbSe_2}$". *Phys. Rev. Lett.* 102.16 (2009), p. 166402. DOI: `10.1103/PhysRevLett.102.166402`.

[Bra+18] J. Brand, S. Gozdzik, N. Néel, J. L. Lado, J. Fernández-Rossier, and J. Kröger. "Electron and Cooper-pair transport across a single magnetic molecule explored with a scanning tunneling microscope". *Phys. Rev. B* 97 (19 2018), p. 195429. DOI: `10.1103/PhysRevB.97.195429`.

[Bra97] T. Brandes. "Truncation method for Green's functions in time-dependent fields". *Phys. Rev. B* 56 (3 1997), pp. 1213–1224. DOI: `10.1103/PhysRevB.56.1213`.

[BS13] B. Braunecker and P. Simon. "Interplay between classical magnetic moments and superconductivity in quantum one-dimensional conductors: toward a self-sustained topological Majorana phase". *Phys. Rev. Lett.* 111.14 (2013), p. 147202. DOI: `10.1103/PhysRevLett.111.147202`.

[Bra+10] B. Braunecker, G. I. Japaridze, J. Klinovaja, and D. Loss. "Spin-selective Peierls transition in interacting one-dimensional conductors with spin-orbit interaction". *Phys. Rev. B* 82.4 (2010), p. 045127. DOI: `10.1103/PhysRevB.82.045127`.

[Bra06] S. Bravyi. "Universal quantum computation with the $\nu = 5/2$ fractional quantum Hall state". *Phys. Rev. A* 73.4 (2006). DOI: `10.1103/physreva.73.042313`.

[Bry+15] P. Brydon, S. D. Sarma, H.-Y. Hui, and J. D. Sau. "Topological Yu-Shiba-Rusinov chain from spin-orbit coupling". *Phys. Rev. B* 91.6 (2015), p. 064505. DOI: `10.1103/PhysRevB.91.064505`.

[CMM09] M. Calandra, I. I. Mazin, and F. Mauri. "Effect of dimensionality on the charge-density wave in few-layer 2 H-NbSe2". *Phys. Rev. B* 80.24 (2009), pp. 1–4. DOI: `10.1103/PhysRevB.80.241108`. arXiv: `0910.0956`.

[CZL17] T. Cao, F. Zhao, and S. G. Louie. "Topological Phases in Graphene Nanoribbons: Junction States, Spin Centers, and Quantum Spin Chains". *Phys. Rev. Lett.* 119.7 (2017), p. 076401. DOI: `10.1103/physrevlett.119.076401`.

[CFG16] J. C. C. Cestari, A. Foerster, and M. A. Gusmão. "Fate of topological states in incommensurate generalized Aubry-André models". *Phys. Rev. B* 93.20 (2016), p. 205441. DOI: `10.1103/physrevb.93.205441`.

[Cha+06] M. Chauvin, P. vom Stein, H. Pothier, P. Joyez, M. E. Huber, D. Esteve, and C. Urbina. "Superconducting Atomic Contacts under Microwave Irradiation". *Phys. Rev. Lett.* 97 (6 2006), p. 067006. DOI: `10.1103/PhysRevLett.97.067006`.

[Che+17] J. Chen, P. Yu, J. Stenger, M. Hocevar, D. Car, S. R. Plissard, E. P.A. M. Bakkers, T. D. Stanescu, and S. M. Frolov. "Experimental phase diagram of zero-bias conductance peaks in superconductor/semiconductor nanowire devices". *Sci. Adv.* 3.9 (2017), e1701476. DOI: `10.1126/sciadv.1701476`.

[CGW10] X. Chen, Z.-C. Gu, and X.-G. Wen. "Local unitary transformation, long-range quantum entanglement, wave function renormalization, and topological order". *Phys. Rev. B* 82.15 (2010). DOI: `10.1103/physrevb.82.155138`.

[Che45] S. shen Chern. "On the Curvatura Integra in a Riemannian Manifold". *Ann. Math.* 46.4 (1945), p. 674. DOI: `10.2307/1969203`.

[Chi+16] C.-K. Chiu, J. C. Teo, A. P. Schnyder, and S. Ryu. "Classification of topological quantum matter with symmetries". *RPM* 88.3 (2016). DOI: `10.1103/revmodphys.88.035005`.

[Cho+18a] K. Cho, M Kończykowski, S. Teknowijoyo, M. A. Tanatar, J Guss, P. Gartin, J. M. Wilde, A Kreyssig, R. McQueeney, A. I. Goldman, et al. "Using controlled disorder to probe the interplay between charge order and superconductivity in $\mathrm{NbSe_2}$". *Nat. Commun.* 9.1 (2018), p. 2796. DOI: `10.1038/s41467-018-05153-0`.

[Cho+17] D.-J. Choi, C. Rubio-Verdú, J. De Bruijckere, M. M. Ugeda, N. Lorente, and J. I. Pascual. "Mapping the orbital structure of impurity bound states in a superconductor". *Nat. Commun.* 8 (2017), p. 15175. DOI: `10.1038/ncomms15175`.

[Cho+18b] D.-J. Choi, C. G. Fernández, E. Herrera, C. Rubio-Verdú, M. M. Ugeda, I. Guillamón, H. Suderow, J. I. Pascual, and N. Lorente. "Influence of Magnetic Ordering between Cr Adatoms on the Yu-Shiba-Rusinov States of the $\beta-\mathrm{Bi_2Pd}$ Superconductor". *Phys. Rev. Lett.* 120.16 (2018), p. 167001. DOI: `10.1103/PhysRevLett.120.167001`.

[Cho+11] T.-P. Choy, J. Edge, A. Akhmerov, and C. Beenakker. "Majorana fermions emerging from magnetic nanoparticles on a superconductor without spin-orbit coupling". *Phys. Rev. B* 84.19 (2011), p. 195442. DOI: `10.1103/PhysRevB.84.195442`.

[Chu+13] H. O. H. Churchill, V. Fatemi, K. Grove-Rasmussen, M. T. Deng, P. Caroff, H. Q. Xu, and C. M. Marcus. “Superconductor-nanowire devices from tunneling to the multichannel regime: Zero-bias oscillations and magnetoconductance crossover”. *Phys. Rev. B* 87.24 (2013). DOI: `10.1103/physrevb.87.241401`.

[CDS19] N. Cooper, J. Dalibard, and I. Spielman. “Topological bands for ultracold atoms”. *RPM* 91.1 (2019). DOI: `10.1103/revmodphys.91.015005`.

[Cor+17] L. Cornils, A. Kamlapure, L. Zhou, S. Pradhan, A. A. Khajetoorians, J. Fransson, J. Wiebe, and R. Wiesendanger. “Spin-Resolved Spectroscopy of the Yu-Shiba-Rusinov States of Individual Atoms”. *Phys. Rev. Lett.* 119.19 (2017), p. 197002. DOI: `10.1103/PhysRevLett.119.197002`.

[Cue+02] J. C. Cuevas, J. Heurich, A. Martín-Rodero, A. Levy Yeyati, and G. Schön. “Subharmonic Shapiro Steps and Assisted Tunneling in Superconducting Point Contacts”. *Phys. Rev. Lett.* 88 (15 2002), p. 157001. DOI: `10.1103/PhysRevLett.88.157001`.

[Dai+14] J. Dai, E. Calleja, J. Alldredge, X. Zhu, L. Li, W. Lu, Y. Sun, T. Wolf, H. Berger, and K. McElroy. “Microscopic evidence for strong periodic lattice distortion in two-dimensional charge-density wave systems”. *Phys. Rev. B* 89.16 (2014), p. 165140. DOI: `10.1103/PhysRevB.89.165140`.

[Das+12] A. Das, Y. Ronen, Y. Most, Y. Oreg, M. Heiblum, and H. Shtrikman. “Zero-bias peaks and splitting in an Al–InAs nanowire topological superconductor as a signature of Majorana fermions”. *Nat. Phys.* 8.12 (2012), pp. 887–895. DOI: `10.1038/nphys2479`.

[DM62] A. H. Dayem and R. J. Martin. “Quantum interaction of microwave radiation with tunneling between superconductors”. *Phys. Rev. Lett.* 8.6 (1962), pp. 246–248. DOI: `10.1103/PhysRevLett.8.246`.

[Dea+10] R. S. Deacon, Y. Tanaka, A. Oiwa, R. Sakano, K. Yoshida, K. Shibata, K. Hirakawa, and S. Tarucha. “Tunneling Spectroscopy of Andreev Energy Levels in a Quantum Dot Coupled to a Superconductor”. *Phys. Rev. Lett.* 104 (7 2010), p. 076805. DOI: `10.1103/PhysRevLett.104.076805`.

[Den+12] M. T. Deng, C. L. Yu, G. Y. Huang, M. Larsson, P. Caroff, and H. Q. Xu. “Anomalous Zero-Bias Conductance Peak in a Nb–InSb Nanowire–Nb Hybrid Device”. *Nano Lett.* 12.12 (2012), pp. 6414–6419. DOI: `10.1021/nl303758w`.

[Den+16] M. T. Deng, S. Vaitiekėnas, E. B. Hansen, J. Danon, M. Leijnse, K. Flensberg, J. Nygård, P. Krogstrup, and C. M. Marcus. “Majorana bound state in a coupled quantum-dot hybrid-nanowire system”. *Science* 354.6319 (2016), pp. 1557–1562. DOI: `10.1126/science.aaf3961`.

[DNG78] R. C. Dynes, V. Narayanamurti, and J. P. Garno. “Direct Measurement of Quasiparticle-Lifetime Broadening in a Strong-Coupled Superconductor”. *Phys. Rev. Lett.* 41.21 (1978), pp. 1509–1512. DOI: `10.1103/physrevlett.41.1509`.

[EF15] S. R. Elliott and M. Franz. "Colloquium: Majorana fermions in nuclear, particle, and solid-state physics". *RPM* 87.1 (2015), pp. 137–163. DOI: `10.1103/revmodphys.87.137`.

[FBS91] G. Falci, V. Bubanja, and G. Schön. "Quasiparticle and Cooper pair tenneling in small capacitance Josephson junctions". *Z. Phys. B* 85.3 (1991), pp. 451–458. DOI: `10.1007/BF01307643`.

[Far+18] L. Farinacci, G. Ahmadi, G. Reecht, M. Ruby, N. Bogdanoff, O. Peters, B. W. Heinrich, F. von Oppen, and K. J. Franke. "Tuning the Coupling of an Individual Magnetic Impurity to a Superconductor: Quantum Phase Transition and Transport". *Phys. Rev. Lett.* 121 (19 2018), p. 196803. DOI: `10.1103/PhysRevLett.121.196803`.

[Fel+16] B. E. Feldman, M. T. Randeria, J. Li, S. Jeon, Y. Xie, Z. Wang, I. K. Drozdov, B. A. Bernevig, and A. Yazdani. "High-resolution studies of the Majorana atomic chain platform". *Nat. Phys.* 13.3 (2016), pp. 286–291. DOI: `10.1038/nphys3947`.

[Fel+17] B. E. Feldman, M. T. Randeria, J. Li, S. Jeon, Y. Xie, Z. Wang, I. K. Drozdov, B. Andrei Bernevig, and A. Yazdani. "High-resolution studies of the Majorana atomic chain platform". *Nat. Phys.* 13.3 (2017), pp. 286–291. DOI: `10.1038/nphys3947`.

[FB97] M. E. Flatté and J. M. Byers. "Local Electronic Structure of a Single Magnetic Impurity in a Superconductor". *Phys. Rev. Lett.* 78.19 (1997), pp. 3761–3764. DOI: `10.1103/PhysRevLett.78.3761`.

[Fle10] K. Flensberg. "Tunneling characteristics of a chain of Majorana bound states". *Phys. Rev. B* 82 (18 2010), p. 180516. DOI: `10.1103/PhysRevB.82.180516`.

[Fle+07] J. D. Fletcher, A. Carrington, P. Diener, P. Rodière, J. P. Brison, R. Prozorov, T. Olheiser, and R. W. Giannetta. "Penetration Depth Study of Superconducting Gap Structure of $2H-\mathrm{NbSe}_2$". *Phys. Rev. Lett.* 98.5 (2007), p. 057003. DOI: `10.1103/PhysRevLett.98.057003`.

[FW15] F. Flicker and J. van Wezel. "Charge order from orbital-dependent coupling evidenced by NbSe_2". *Nat. Commun.* 6.May (2015), p. 7034. DOI: `10.1038/ncomms8034`.

[F+̈07] S. Fölling, S. Trotzky, P. Cheinet, M. Feld, R. Saers, A. Widera, T. Müller, and I. Bloch. "Direct observation of second-order atom tunnelling". *Nature* 448.7157 (2007), pp. 1029–1032. DOI: `10.1038/nature06112`.

[FSP11] K. Franke, G Schulze, and J. Pascual. "Competition of superconducting phenomena and Kondo screening at the nanoscale". *Science* 332.6032 (2011), pp. 940–944. DOI: `10.1126/science.1202204`.

[FK08] L. Fu and C. L. Kane. "Superconducting Proximity Effect and Majorana Fermions at the Surface of a Topological Insulator". *Phys. Rev. Lett.* 100.9 (2008). DOI: `10.1103/physrevlett.100.096407`.

[FK09] L. Fu and C. L. Kane. "Josephson current and noise at a superconductor/quantum-spin-Hall-insulator/superconductor junction". *Phys. Rev. B* 79.16 (2009). DOI: `10.1103/physrevb.79.161408`.

[GVA02] A. Gabovich, A. Voitenko, and M. Ausloos. “Charge-and spin-density waves in existing superconductors: competition between Cooper pairing and Peierls or excitonic instabilities”. *Phys. Rep.* 367.6 (2002), pp. 583–709. DOI: `10.1016/S0370-1573(02)00029-7`.

[GSS13] S. Ganeshan, K. Sun, and S. D. Sarma. “Topological Zero-Energy Modes in Gapless Commensurate Aubry-André-Harper Models”. *Phys. Rev. Lett.* 110.18 (2013), p. 180403. DOI: `10.1103/physrevlett.110.180403`.

[GO19] S. Głodzik and T. Ojanen. “Engineering nodal topological phases in Ising superconductors by magnetic superstructures”. *New J. Phys.* (2019). DOI: `10.1088/1367-2630/ab61d8`.

[GW81] J. Goldstone and F. Wilczek. “Fractional Quantum Numbers on Solitons”. *Phys. Rev. Lett.* 47.14 (1981), pp. 986–989. DOI: `10.1103/physrevlett.47.986`.

[GBS15] J. Gramich, A. Baumgartner, and C. Schönenberger. “Resonant and Inelastic Andreev Tunneling Observed on a Carbon Nanotube Quantum Dot”. *Phys. Rev. Lett.* 115.21 (2015), p. 216801. DOI: `10.1103/PhysRevLett.115.216801`.

[Gr18] O. Gröning et al. “Engineering of robust topological quantum phases in graphene nanoribbons”. *Nature* 560.7717 (2018), pp. 209–213. DOI: `10.1038/s41586-018-0375-9`.

[Gru94] G. Gruner. *Density waves in solids*. CRC Press, 1994. DOI: `10.1201/9780429501012`.

[Gui+08a] I. Guillamón, H. Suderow, F. Guinea, and S. Vieira. “Intrinsic atomic-scale modulations of the superconducting gap of $2H-\mathrm{NbSe}_2$”. *Phys. Rev. B* 77.13 (2008), p. 134505. DOI: `10.1103/PhysRevB.77.134505`.

[Gui+08b] I. Guillamón, H. Suderow, S. Vieira, L. Cario, P. Diener, and P. Rodière. “Superconducting Density of States and Vortex Cores of 2H-NbS_2”. *Phys. Rev. Lett.* 101.16 (2008), p. 166407. DOI: `10.1103/PhysRevLett.101.166407`.

[G+̈18] Önder Gül et al. “Ballistic Majorana nanowire devices”. *Nat. Nanotechnol.* 13.3 (2018), pp. 192–197. DOI: `10.1038/s41565-017-0032-8`.

[Gus+19] B. Guster et al. “Coexistence of Elastic Modulations in the Charge Density Wave State of $2H$-NbSe_2”. *Nano Lett.* 19.5 (2019), pp. 3027–3032. DOI: `10.1021/acs.nanolett.9b00268`.

[GOY19] G. Gye, E. Oh, and H. W. Yeom. “Topological Landscape of Competing Charge Density Waves in $2H-\mathrm{NbSe}_2$”. *Phys. Rev. Lett.* 122.1 (2019), p. 016403. DOI: `10.1103/PhysRevLett.122.016403`.

[Hal88] F. D. M. Haldane. “Model for a Quantum Hall Effect without Landau Levels: Condensed-Matter Realization of the "Parity Anomaly"”. *Phys. Rev. Lett.* 61.18 (1988), pp. 2015–2018. DOI: `10.1103/physrevlett.61.2015`.

[Har55] P. G. Harper. “Single Band Motion of Conduction Electrons in a Uniform Magnetic Field”. *Proc. Phys. Soc., London, Sect. A* 68.10 (1955), pp. 874–878. DOI: `10.1088/0370-1298/68/10/304`.

[HK10] M. Z. Hasan and C. L. Kane. "Colloquium: Topological insulators". *RPM* 82.4 (2010), pp. 3045–3067. DOI: `10.1103/revmodphys.82.3045`.

[Hat+15] N. Hatter, B. W. Heinrich, M. Ruby, J. I. Pascual, and K. J. Franke. "Magnetic anisotropy in Shiba bound states across a quantum phase transition". *Nat. Commun.* 6 (2015), p. 8988. DOI: `10.1038/ncomms9988`.

[Hee+88] A. J. Heeger, S. Kivelson, J. R. Schrieffer, and W. P. Su. "Solitons in conducting polymers". *RPM* 60.3 (1988), pp. 781–850. DOI: `10.1103/revmodphys.60.781`.

[HPF18] B. W. Heinrich, J. I. Pascual, and K. J. Franke. "Single magnetic adsorbates on s-wave superconductors". *Prog. Surf. Sci.* 93.1 (2018), pp. 1–19. DOI: `10.1016/j.progsurf.2018.01.001`.

[HRW90] H. F. Hess, R. B. Robinson, and J. V. Waszczak. "Vortex-core structure observed with a scanning tunneling microscope". *Phys. Rev. Lett.* 64 (22 1990), pp. 2711–2714. DOI: `10.1103/PhysRevLett.64.2711`.

[Hew93] A. C. Hewson. *The Kondo Problem to Heavy Fermions*. Cambridge University Press, 1993. DOI: `10.1017/CBO9780511470752`.

[Hof76] D. R. Hofstadter. "Energy levels and wave functions of Bloch electrons in rational and irrational magnetic fields". *Phys. Rev. B* 14.6 (1976), pp. 2239–2249. DOI: `10.1103/physrevb.14.2239`.

[Ino+08] D. S. Inosov, V. B. Zabolotnyy, D. V. Evtushinsky, A. A. Kordyuk, B Büchner, R Follath, H Berger, and S. V. Borisenko. "Fermi surface nesting in several transition metal dichalcogenides". *New J. Phys.* 10.12 (2008), p. 125027. DOI: `10.1088/1367-2630/10/12/125027`.

[Ino+09] D. S. Inosov, D. V. Evtushinsky, V. B. Zabolotnyy, A. A. Kordyuk, B. Büchner, R. Follath, H. Berger, and S. V. Borisenko. "Temperature-dependent Fermi surface of $2H$-TaSe$_2$ driven by competing density wave order fluctuations". *Phys. Rev. B* 79.12 (2009), p. 125112. DOI: `10.1103/PhysRevB.79.125112`.

[Iva01] D. A. Ivanov. "Non-Abelian Statistics of Half-Quantum Vortices inp-Wave Superconductors". *Phys. Rev. Lett.* 86.2 (2001), pp. 268–271. DOI: `10.1103/physrevlett.86.268`.

[JR76] R. Jackiw and C. Rebbi. "Solitons with fermion number 1/2". *Phys. Rev. D* 13.12 (1976), pp. 3398–3409. DOI: `10.1103/physrevd.13.3398`.

[Jeo+17] S. Jeon, Y. Xie, J. Li, Z. Wang, B. A. Bernevig, and A. Yazdani. "Distinguishing a Majorana zero mode using spin-resolved measurements." *Science* 358.6364 (2017), pp. 772–776. DOI: `10.1126/science.aan3670`.

[Ji+08] S.-H. Ji, T. Zhang, Y.-S. Fu, X. Chen, X.-C. Ma, J. Li, W.-H. Duan, J.-F. Jia, and Q.-K. Xue. "High-Resolution Scanning Tunneling Spectroscopy of Magnetic Impurity Induced Bound States in the Superconducting Gap of Pb Thin Films". *Phys. Rev. Lett.* 100.22 (2008), p. 226801. DOI: `10.1103/PhysRevLett.100.226801`.

[JM08] M. D. Johannes and I. I. Mazin. "Fermi surface nesting and the origin of charge density waves in metals". *Phys. Rev. B* 77.16 (2008), p. 165135. DOI: `10.1103/PhysRevB.77.165135`.

[JMH06a] M. D. Johannes, I. I. Mazin, and C. A. Howells. "Fermi-surface nesting and the origin of the charge-density wave in $\mathrm{NbSe_2}$". *Phys. Rev. B* 73.20 (2006), p. 205102. DOI: `10.1103/PhysRevB.73.205102`.

[JMH06b] M. Johannes, I. Mazin, and C. Howells. "Fermi-surface nesting and the origin of the charge-density wave in Nb Se 2". *Phys. Rev. B* 73.20 (2006), p. 205102. DOI: `10.1103/PhysRevB.73.205102`.

[Jos62] B. Josephson. "Possible new effects in superconductive tunnelling". *Phys. Lett.* 1.7 (1962), pp. 251 –253. DOI: `https://doi.org/10.1016/0031-9163(62)91369-0`.

[Kal12] C. Kallin. "Chiral p-wave order in Sr2RuO4". *Rep. Prog. Phys.* 75.4 (2012), p. 042501. DOI: `10.1088/0034-4885/75/4/042501`.

[Kam+18] A. Kamlapure, L. Cornils, J. Wiebe, and R. Wiesendanger. "Engineering the spin couplings in atomically crafted spin chains on an elemental superconductor". *Nat. Commun.* 9.1 (2018), pp. 1–7. DOI: `10.1038/s41467-018-05701-8`.

[KMB12] G. Kells, D. Meidan, and P. W. Brouwer. "Near-zero-energy end states in topologically trivial spin-orbit coupled superconducting nanowires with a smooth confinement". *Phys. Rev. B* 86.10 (2012). DOI: `10.1103/physrevb.86.100503`.

[Kez+18a] S. Kezilebieke, M. Dvorak, T. Ojanen, and P. Liljeroth. "Coupled Yu–Shiba–Rusinov states in molecular dimers on NbSe2". *Nano Lett.* 18.4 (2018), pp. 2311–2315. DOI: `10.1021/acs.nanolett.7b05050`.

[Kez+18b] S. Kezilebieke, M. Dvorak, T. Ojanen, and P. Liljeroth. "Coupled Yu-Shiba-Rusinov States in Molecular Dimers on $\mathrm{NbSe_2}$". *Nano Lett.* 18.4 (2018), pp. 2311–2315. DOI: `10.1021/acs.nanolett.7b05050`.

[Kim+18] H. Kim, A. Palacio-Morales, T. Posske, L. Rózsa, K. Palotás, L. Szunyogh, M. Thorwart, and R. Wiesendanger. "Toward tailoring Majorana bound states in artificially constructed magnetic atom chains on elemental superconductors". *Sci. Adv.* 4.5 (2018), eaar5251. DOI: `10.1126/sciadv.aar5251`. eprint: `https://advances.sciencemag.org/content/4/5/eaar5251.full.pdf`.

[Kim+14] Y. Kim, M. Cheng, B. Bauer, R. M. Lutchyn, and S. D. Sarma. "Helical order in one-dimensional magnetic atom chains and possible emergence of Majorana bound states". *Phys. Rev. B* 90.6 (2014), p. 060401. DOI: `10.1103/PhysRevB.90.060401`.

[Kir+15] G. Kiršanskas, M. Goldstein, K. Flensberg, L. I. Glazman, and J. Paaske. "Yu-Shiba-Rusinov states in phase-biased superconductor–quantum dot–superconductor junctions". *Phys. Rev. B* 92.23 (2015), p. 235422. DOI: `10.1103/PhysRevB.92.235422`.

[Kis+07] T. Kiss, T. Yokoya, A. Chainani, S. Shin, T. Hanaguri, M. Nohara, and H. Takagi. "Charge-order-maximized momentum-dependent superconductivity". *Nat. Phys.* 3.10 (2007), pp. 720–725. DOI: `10.1038/nphys699`.

[Kit01] A. Y. Kitaev. "Unpaired Majorana fermions in quantum wires". *Phys.-Uspekhi* 44.10S (2001), pp. 131–136. DOI: `10.1070/1063-7869/44/10s/s29`.

[Kli+13] J. Klinovaja, P. Stano, A. Yazdani, and D. Loss. "Topological superconductivity and Majorana fermions in RKKY systems". *Phys. Rev. Lett.* 111.18 (2013), p. 186805. DOI: `10.1103/PhysRevLett.111.186805`.

[KDP80] K. v. Klitzing, G. Dorda, and M. Pepper. "New Method for High-Accuracy Determination of the Fine-Structure Constant Based on Quantized Hall Resistance". *Phys. Rev. Lett.* 45.6 (1980), pp. 494–497. DOI: `10.1103/physrevlett.45.494`.

[Kli05] K. von Klitzing. "Developments in the quantum Hall effect". *Philosophical Transactions of the Royal Society A: Mathematical, Physical and Engineering Sciences* 363.1834 (2005), pp. 2203–2219. DOI: `10.1098/rsta.2005.1640`.

[KT73] J. M. Kosterlitz and D. J. Thouless. "Ordering, metastability and phase transitions in two-dimensional systems". *J. Phys. C Solid State Phys.* 6.7 (1973), pp. 1181–1203. DOI: `10.1088/0022-3719/6/7/010`.

[Kot+20] P. Kot, R. Drost, M. Uhl, J. Ankerhold, J. C. Cuevas, and C. R. Ast. "Microwave-assisted tunneling and interference effects in superconducting junctions under fast driving signals". *Phys. Rev. B* 101.13 (2020). DOI: `10.1103/physrevb.101.134507`.

[Kou+94] L. P. Kouwenhoven, S. Jauhar, K. McCormick, D. Dixon, P. L. McEuen, Y. V. Nazarov, N. C. Van Der Vaart, and C. T. Foxon. "Photon-assisted tunneling through a quantum dot". *Phys. Rev. B* 50.3 (1994), pp. 2019–2022. DOI: `10.1103/PhysRevB.50.2019`.

[LLN09] K. T. Law, P. A. Lee, and T. K. Ng. "Majorana Fermion Induced Resonant Andreev Reflection". *Phys. Rev. Lett.* 103 (23 2009), p. 237001. DOI: `10.1103/PhysRevLett.103.237001`.

[Lee+12] E. J. H. Lee, X. Jiang, R. Aguado, G. Katsaros, C. M. Lieber, and S. D. Franceschi. "Zero-Bias Anomaly in a Nanowire Quantum Dot Coupled to Superconductors". *Phys. Rev. Lett.* 109.18 (2012). DOI: `10.1103/physrevlett.109.186802`.

[Lee+17] E. J. H. Lee, X. Jiang, R. Aguado, C. M. Lieber, and S. De Franceschi. "Scaling of subgap excitations in a superconductor-semiconductor nanowire quantum dot". *Phys. Rev. B* 95 (18 2017), p. 180502. DOI: `10.1103/PhysRevB.95.180502`.

[LY+97] A. Levy-Yeyati, J. C. Cuevas, A. López-Dávalos, and A. Martín-Rodero. "Resonant tunneling through a small quantum dot coupled to superconducting leads". *Phys. Rev. B* 55 (10 1997), R6137–R6140. DOI: `10.1103/PhysRevB.55.R6137`.

[LXC14] L. Li, Z. Xu, and S. Chen. "Topological phases of generalized Su-Schrieffer-Heeger models". *Phys. Rev. B* 89.8 (2014), p. 085111. DOI: `10.1103/physrevb.89.085111`.

[Lie+19] E. Liebhaber, S. Acero González, R. Baba, G. Reecht, B. W. Heinrich, S. Rohlf, K. Rossnagel, F. von Oppen, and K. J. Franke. "Yu-Shiba-Rusinov states in the charge-density modulated superconductor NbSe2". *Nano Lett.* (2019). DOI: `10.1021/acs.nanolett.9b03988`.

[LGC15] F. Liu, S. Ghosh, and Y. D. Chong. "Localization and adiabatic pumping in a generalized Aubry-André-Harper model". *Phys. Rev. B* 91.1 (2015), p. 014108. DOI: `10.1103/physrevb.91.014108`.

[Liu+12] J. Liu, A. C. Potter, K. T. Law, and P. A. Lee. "Zero-Bias Peaks in the Tunneling Conductance of Spin-Orbit-Coupled Superconducting Wires with and without Majorana End-States". *Phys. Rev. Lett.* 109.26 (2012). DOI: `10.1103/physrevlett.109.267002`.

[Liu+17] T. Liu, P. Wang, S. Chen, and G. Xianlong. "Phase diagram of a generalized off-diagonal Aubry–André model withp-wave pairing". *J. Physics B* 51.2 (2017), p. 025301. DOI: `10.1088/1361-6455/aa98d6`.

[Lut+18] R. M. Lutchyn, E. P.A. M. Bakkers, L. P. Kouwenhoven, P. Krogstrup, C. M. Marcus, and Y. Oreg. "Majorana zero modes in superconductor–semiconductor heterostructures". *Nat. Rev. Mater.* 3.5 (2018), pp. 52–68. DOI: `10.1038/s41578-018-0003-1`.

[LSS10] R. M. Lutchyn, J. D. Sau, and S. D. Sarma. "Majorana Fermions and a Topological Phase Transition in Semiconductor-Superconductor Heterostructures". *Phys. Rev. Lett.* 105.7 (2010). DOI: `10.1103/physrevlett.105.077001`.

[Maj37] E. Majorana. "Teoria simmetrica dell'elettrone e del positrone". *Il Nuovo Cimento* 14.4 (1937), pp. 171–184. DOI: `10.1007/bf02961314`.

[Mal+18] L. Malavolti et al. "Tunable Spin-Superconductor Coupling of Spin 1/2 Vanadyl Phthalocyanine Molecules". *Nano Lett.* 18.12 (2018), pp. 7955–7961. DOI: `10.1021/acs.nanolett.8b03921`.

[MK13] C. D. Malliakas and M. G. Kanatzidis. "Nb-Nb Interactions Define the Charge Density Wave Structure of 2H-NbSe$_2$". *J. Am. Chem. Soc.* 135.5 (2013), pp. 1719–22. DOI: `10.1021/ja3120554`.

[Mat73a] L. Mattheiss. "Band structures of transition-metal-dichalcogenide layer compounds". *Phys. Rev. B* 8.8 (1973), p. 3719. DOI: `10.1103/PhysRevB.8.3719`.

[Mat73b] L. Mattheiss. "Energy Bands for 2 H- Nb Se 2 and 2 H- Mo S 2". *Phys. Rev. Lett.* 30.17 (1973), p. 784. DOI: `10.1103/PhysRevLett.30.784`.

[MAG16] E. J. Meier, F. A. An, and B. Gadway. "Observation of the topological soliton state in the Su–Schrieffer–Heeger model". *Nat. Commun.* 7.1 (2016). DOI: `10.1038/ncomms13986`.

[Mén+15] G. C. Ménard et al. "Coherent long-range magnetic bound states in a superconductor". *Nat. Phys.* 11.October (2015), p. 1013. DOI: `10.1038/nphys3508`.

[MEK07] C. Meyer, J. M. Elzerman, and L. P. Kouwenhoven. "Photon-assisted tunneling in a carbon nanotube quantum dot". *Nano Lett.* 7.2 (2007), pp. 295–299. DOI: `10.1021/nl062273j`.

[Moc+08] C. P. Moca, E. Demler, B. Jankó, and G. Zaránd. "Spin-resolved spectra of Shiba multiplets from Mn impurities in MgB$_2$". *Phys. Rev. B* 77.17 (2008), p. 174516. DOI: `10.1103/PhysRevB.77.174516`.

[MR91] G. Moore and N. Read. "Nonabelions in the fractional quantum hall effect". *Nucl. Phys. B* 360.2-3 (1991), pp. 362–396. DOI: `10.1016/0550-3213(91)90407-o`.

[Mou+12] V. Mourik, K. Zuo, S. M. Frolov, S. R. Plissard, E. P.A. M. Bakkers, and L. P. Kouwenhoven. "Signatures of Majorana Fermions in Hybrid Superconductor-Semiconductor Nanowire Devices". *Science* 336.6084 (2012), pp. 1003–1007. DOI: `10.1126/science.1222360`.

[NTD01] O. Naaman, W. Teizer, and R. C. Dynes. "Fluctuation Dominated Josephson Tunneling with a Scanning Tunneling Microscope". *Phys. Rev. Lett.* 87 (9 2001), p. 097004. DOI: `10.1103/PhysRevLett.87.097004`.

[NP+13] S Nadj-Perge, I. Drozdov, B. A. Bernevig, and A. Yazdani. "Proposal for realizing Majorana fermions in chains of magnetic atoms on a superconductor". *Phys. Rev. B* 88.2 (2013), p. 020407. DOI: `10.1103/PhysRevB.88.020407`.

[NP+14] S. Nadj-Perge, I. K. Drozdov, J. Li, H. Chen, S. Jeon, J. Seo, A. H. MacDonald, B. A. Bernevig, and A. Yazdani. "Observation of Majorana fermions in ferromagnetic atomic chains on a superconductor". *Science* 346.6209 (2014), pp. 602–607. DOI: `10.1126/science.1259327`.

[Nak03] M. Nakahara. *Geometry, topology and physics*. CRC Press, 2003.

[NT99] Y. Nakamura and J. S. Tsai. *J. Supercond.* 12.6 (1999), pp. 799–806. DOI: `10.1023/a:1007793228293`.

[Nak+18] Y. Nakata, K. Sugawara, S. Ichinokura, Y. Okada, T. Hitosugi, T. Koretsune, K. Ueno, S. Hasegawa, T. Takahashi, and T. Sato. "Anisotropic band splitting in monolayer NbSe 2: implications for superconductivity and charge density wave". *NPJ 2D Mater. Appl.* 2.1 (2018), pp. 1–6. DOI: `10.1038/s41699-018-0057-3`.

[NTN13] S. Nakosai, Y. Tanaka, and N. Nagaosa. "Two-dimensional p-wave superconducting states with magnetic moments on a conventional s-wave superconductor". *Phys. Rev. B* 88.18 (2013), p. 180503. DOI: `10.1103/PhysRevB.88.180503`.

[Nay+08] C. Nayak, S. H. Simon, A. Stern, M. Freedman, and S. D. Sarma. "Non-Abelian anyons and topological quantum computation". *RPM* 80.3 (2008), pp. 1083–1159. DOI: `10.1103/revmodphys.80.1083`.

[Nic+17] F. Nichele et al. "Scaling of Majorana Zero-Bias Conductance Peaks". *Phys. Rev. Lett.* 119 (13 2017), p. 136803. DOI: `10.1103/PhysRevLett.119.136803`.

[Noa+10] Y. Noat, T. Cren, F. Debontridder, D. Roditchev, W. Sacks, P. Toulemonde, and A. San Miguel. "Signatures of multigap superconductivity in tunneling spectroscopy". *Phys. Rev. B* 82.1 (2010), p. 014531. DOI: `10.1103/PhysRevB.82.014531`.

[Noa+15] Y. Noat et al. "Quasiparticle spectra of $2H - \mathrm{NbSe}_2$: Two-band superconductivity and the role of tunneling selectivity". *Phys. Rev. B* 92.13 (2015), p. 134510. DOI: `10.1103/PhysRevB.92.134510`.

[OPP17] F. von Oppen, Y. Peng, and F. Pientka. "Topological superconducting phases in one dimension". *Lecture Notes of the Les Houches Summer School: Topological Aspects of Condensed Matter Physics* (2017), pp. 387–447.

[ORO10] Y. Oreg, G. Refael, and F. von Oppen. "Helical Liquids and Majorana Bound States in Quantum Wires". *Phys. Rev. Lett.* 105.17 (2010). DOI: 10.1103/physrevlett.105.177002.

[Paw+16] R. Pawlak, M. Kisiel, J. A. Klinovaja, T. Meier, S. Kawai, T. Glatzel, D. Loss, and E. Meyer. "Probing atomic structure and majorana wavefunctions in mono-atomic fe chains on superconducting Pb surface". *npj Quantum Inf.* 2.1 (2016), p. 16035. DOI: 10.1038/npjqi.2016.35.

[Pei96] R. E. Peierls. *Quantum theory of solids*. Clarendon Press, 1996.

[Pen+15a] Y. Peng, F. Pientka, Y. Vinkler-Aviv, L. I. Glazman, and F. von Oppen. "Robust Majorana Conductance Peaks for a Superconducting Lead". *Phys. Rev. Lett.* 115 (26 2015), p. 266804. DOI: 10.1103/PhysRevLett.115.266804.

[Pen+15b] Y. Peng, F. Pientka, L. I. Glazman, and F. von Oppen. "Strong Localization of Majorana End States in Chains of Magnetic Adatoms". *Phys. Rev. Lett.* 114.10 (2015). DOI: 10.1103/physrevlett.114.106801.

[PG+19] B. Pérez-González, M. Bello, Á. Gómez-León, and G. Platero. "Interplay between long-range hopping and disorder in topological systems". *Phys. Rev. B* 99.3 (2019), p. 035146. DOI: 10.1103/physrevb.99.035146.

[Pet+20] O. Peters, N. Bogdanoff, S. Acero González, L. Melischek, J. R. Simon, G. Reecht, C. B. Winkelmann, F. von Oppen, and K. J. Franke. "Resonant Andreev reflections probed by photon-assisted tunnelling at the atomic scale". *Nat. Phys.* (2020). DOI: 10.1038/s41567-020-0972-z.

[PGO13] F. Pientka, L. I. Glazman, and F. von Oppen. "Topological superconducting phase in helical Shiba chains". *Phys. Rev. B* 88 (15 2013), p. 155420. DOI: 10.1103/PhysRevB.88.155420.

[PGO14] F. Pientka, L. I. Glazman, and F. von Oppen. "Unconventional topological phase transitions in helical Shiba chains". *Phys. Rev. B* 89.18 (2014). DOI: 10.1103/physrevb.89.180505.

[PA04] G. Platero and R. Aguado. "Photon-assisted transport in semiconductor nanostructures". *Phys. Rep.* 395.1 (2004), pp. 1 –157. DOI: https://doi.org/10.1016/j.physrep.2004.01.004.

[PS09] W. Poirier and F. Schopfer. "Resistance metrology based on the quantum Hall effect". *Eur. Phys. J. Spec. Top.* 172.1 (2009), pp. 207–245. DOI: 10.1140/epjst/e2009-01051-5.

[P+̈14] K. Pöyhönen, A. Westström, J. Röntynen, and T. Ojanen. "Majorana states in helical Shiba chains and ladders". *Phys. Rev. B* 89.11 (2014). DOI: 10.1103/physrevb.89.115109.

[QWZ06] X.-L. Qi, Y.-S. Wu, and S.-C. Zhang. "Topological quantization of the spin Hall effect in two-dimensional paramagnetic semiconductors". *Phys. Rev. B* 74.8 (2006). DOI: 10.1103/physrevb.74.085308.

[Rah+12] D. J. Rahn, S. Hellmann, M. Kalläne, C. Sohrt, T. K. Kim, L. Kipp, and K. Rossnagel. “Gaps and kinks in the electronic structure of the superconductor $2H$-NbSe$_2$ from angle-resolved photoemission at 1 K”. *Phys. Rev. B* 85.22 (2012), p. 224532. DOI: `10.1103/PhysRevB.85.224532`.

[Ran+16] M. T. Randeria, B. E. Feldman, I. K. Drozdov, and A. Yazdani. “Scanning Josephson spectroscopy on the atomic scale”. *Phys. Rev. B* 93.16 (2016), p. 161115. DOI: `10.1103/PhysRevB.93.161115`.

[RG00] N. Read and D. Green. “Paired states of fermions in two dimensions with breaking of parity and time-reversal symmetries and the fractional quantum Hall effect”. *Phys. Rev. B* 61.15 (2000), pp. 10267–10297. DOI: `10.1103/physrevb.61.10267`.

[Res94] R. Resta. “Macroscopic polarization in crystalline dielectrics: the geometric phase approach”. *RPM* 66.3 (1994), pp. 899–915. DOI: `10.1103/revmodphys.66.899`.

[Res00] R. Resta. “Manifestations of Berry’s phase in molecules and condensed matter”. *Journal of Physics: Condensed Matter* 12.9 (2000), R107–R143. DOI: `10.1088/0953-8984/12/9/201`.

[RBB17] J.-W. Rhim, J. Behrends, and J. H. Bardarson. “Bulk-boundary correspondence from the intercellular Zak phase”. *Phys. Rev. B* 95.3 (2017). DOI: `10.1103/physrevb.95.035421`.

[Rit+13] T Ritschel, J Trinckauf, G Garbarino, M Hanfland, M. v. Zimmermann, H Berger, B Büchner, and J Geck. “Pressure dependence of the charge density wave in 1 T-TaS 2 and its relation to superconductivity”. *Phys. Rev. B* 87.12 (2013), p. 125135. DOI: `10.1103/PhysRevB.87.125135`.

[Riz+18] D. J. Rizzo, G. Veber, T. Cao, C. Bronner, T. Chen, F. Zhao, H. Rodriguez, S. G. Louie, M. F. Crommie, and F. R. Fischer. “Topological band engineering of graphene nanoribbons”. *Nature* 560.7717 (2018), pp. 204–208. DOI: `10.1038/s41586-018-0376-8`.

[RV04] J. G. Rodrigo and S. Vieira. “STM study of multiband superconductivity in NbSe$_2$ using a superconducting tip”. *Physica C* 404.1-4 (2004), pp. 306–310. DOI: `10.1016/j.physc.2003.10.030`.

[RLF12] L. P. Rokhinson, X. Liu, and J. K. Furdyna. “The fractional a.c. Josephson effect in a semiconductor–superconductor nanowire as a signature of Majorana particles”. *Nat. Phys.* 8.11 (2012), pp. 795–799. DOI: `10.1038/nphys2429`.

[Ros+01] K. Rossnagel, O. Seifarth, L. Kipp, M. Skibowski, D. Voß, P. Krüger, A. Mazur, and J. Pollmann. “Fermi surface of $2H-\mathrm{NbSe}_2$ and its implications on the charge-density-wave mechanism”. *Phys. Rev. B* 64.23 (2001), p. 235119. DOI: `10.1103/PhysRevB.64.235119`.

[Ros+05] K. Rossnagel, E. Rotenberg, H. Koh, N. V. Smith, and L. Kipp. “Fermi surface, charge-density-wave gap, and kinks in $2H-\mathrm{TaSe}_2$”. *Phys. Rev. B* 72.12 (2005), p. 121103. DOI: `10.1103/PhysRevB.72.121103`.

[Roy+15] A. Roychowdhury, M. Dreyer, J. R. Anderson, C. J. Lobb, and F. C. Wellstood. “Microwave photon-assisted incoherent cooper-pair tunneling in a Josephson STM”. *Phys. Rev. Appl.* 4.3 (2015).

[Rub+15a] M. Ruby, F. Pientka, Y. Peng, F. von Oppen, B. W. Heinrich, and K. J. Franke. "End States and Subgap Structure in Proximity-Coupled Chains of Magnetic Adatoms". *Phys. Rev. Lett.* 115 (19 2015), p. 197204. DOI: `10.1103/PhysRevLett.115.197204`.

[Rub+15b] M. Ruby, F. Pientka, Y. Peng, F. von Oppen, B. W. Heinrich, and K. J. Franke. "Tunneling Processes into Localized Subgap States in Superconductors". *Phys. Rev. Lett.* 115 (8 2015), p. 087001. DOI: `10.1103/PhysRevLett.115.087001`.

[Rub+16] M. Ruby, Y. Peng, F. von Oppen, B. W. Heinrich, and K. J. Franke. "Orbital Picture of Yu-Shiba-Rusinov Multiplets". *Phys. Rev. Lett.* 117.18 (2016), p. 186801. DOI: `10.1103/PhysRevLett.117.186801`.

[Rub+17] M. Ruby, B. W. Heinrich, Y. Peng, F. von Oppen, and K. J. Franke. "Exploring a Proximity-Coupled Co Chain on Pb(110) as a Possible Majorana Platform". *Nano Lett.* 17.7 (2017), 4473–4477. DOI: `10.1021/acs.nanolett.7b01728`.

[Rub+18] M. Ruby, B. W. Heinrich, Y. Peng, F. von Oppen, and K. J. Franke. "Wave-Function Hybridization in Yu-Shiba-Rusinov Dimers". *Phys. Rev. Lett.* 120.15 (2018), p. 156803. DOI: `10.1103/PhysRevLett.120.156803`.

[Rus69] A. Rusinov. "Theory of gapless superconductivity in alloys containing paramagnetic impurities". *Sov. Phys. JETP* 29.6 (1969), pp. 1101–1106.

[Sak70] A. Sakurai. "Comments on superconductors with magnetic impurities". *Prog. Theor. Phys.* 44.6 (1970), pp. 1472–1476. DOI: `10.1143/PTP.44.1472`.

[SBS97] M. I. Salkola, A. V. Balatsky, and J. R. Schrieffer. "Spectral properties of quasiparticle excitations induced by magnetic moments in superconductors". *Phys. Rev. B* 55.18 (1997), pp. 12648–12661. DOI: `10.1103/PhysRevB.55.12648`.

[SF16] M. Sato and S. Fujimoto. "Majorana Fermions and Topology in Superconductors". *J. Phys. Soc. Jpn.* 85.7 (2016), p. 072001. DOI: `10.7566/jpsj.85.072001`.

[Sch+18] F. Schindler, A. M. Cook, M. G. Vergniory, Z. Wang, S. S. P. Parkin, B. A. Bernevig, and T. Neupert. "Higher-order topological insulators". *Sci. Adv.* 4.6 (2018), eaat0346. DOI: `10.1126/sciadv.aat0346`.

[Sch+20] L. Schneider, S. Brinker, M. Steinbrecher, J. Hermenau, T. Posske, M. dos Santos Dias, S. Lounis, R. Wiesendanger, and J. Wiebe. "Controlling in-gap end states by linking nonmagnetic atoms and artificially-constructed spin chains on superconductors" (2020). arXiv: `2002.12294`.

[SW63] J. R. Schrieffer and J. W. Wilkins. "Two-Particle Tunneling Processes Between Superconductors". *Phys. Rev. Lett.* 10 (1 1963), pp. 17–20. DOI: `10.1103/PhysRevLett.10.17`.

[SS+06] J. Sebby-Strabley, M. Anderlini, P. S. Jessen, and J. V. Porto. "Lattice of double wells for manipulating pairs of cold atoms". *Phys. Rev. A* 73.3 (2006). DOI: `10.1103/physreva.73.033605`.

[Sen+19] J. Senkpiel et al. "Robustness of Yu-Shiba-Rusinov resonances in the presence of a complex superconducting order parameter". *Phys. Rev. B* 100.1 (2019), p. 014502. DOI: `10.1103/PhysRevB.100.014502`.

[Shi68] H. Shiba. "Classical spins in superconductors". *Prog. Theor. Phys.* 40.3 (1968), pp. 435–451. DOI: `10.1143/PTP.40.435`.

[SKD85] N. V. Smith, S. D. Kevan, and F. J. DiSalvo. "Band structures of the layer compounds 1T-TaS_2 and 2H-$TaSe_2$ in the presence of commensurate charge-density waves". *J. Phys. C: Solid State Phys.* 18.16 (1985), pp. 3175–3189. DOI: `10.1088/0022-3719/18/16/013`.

[Sou+13] A. Soumyanarayanan, M. M. Yee, Y. He, J. van Wezel, D. J. Rahn, K. Rossnagel, E. W. Hudson, M. R. Norman, and J. E. Hoffman. "Quantum phase transition from triangular to stripe charge order in $NbSe_2$". *Proc. Natl. Acad. Sci.* 110.5 (2013), pp. 1623–7. DOI: `10.1073/pnas.1211387110`.

[SM19] D. Sticlet and C. Morari. "Topological superconductivity from magnetic impurities on monolayer NbSe 2". *Phys. Rev. B* 100.7 (2019), p. 075420. DOI: `10.1103/PhysRevB.100.075420`.

[SSH79] W. P. Su, J. R. Schrieffer, and A. J. Heeger. "Solitons in Polyacetylene". *Phys. Rev. Lett.* 42.25 (1979), pp. 1698–1701. DOI: `10.1103/physrevlett.42.1698`.

[Sud+05] H. Suderow, V. G. Tissen, J. P. Brison, J. L. Martínez, and S. Vieira. "Pressure Induced Effects on the Fermi Surface of Superconducting 2H$-$$NbSe_2$". *Phys. Rev. Lett.* 95.11 (2005), p. 117006. DOI: `10.1103/PhysRevLett.95.117006`.

[Suo+17] H. Suominen, M. Kjaergaard, A. Hamilton, J. Shabani, C. Palmstrøm, C. Marcus, and F. Nichele. "Zero-Energy Modes from Coalescing Andreev States in a Two-Dimensional Semiconductor-Super-conductor Hybrid Platform". *Phys. Rev. Lett.* 119.17 (2017). DOI: `10.1103/physrevlett.119.176805`.

[TZL15] H.-Z. Tang, Y.-T. Zhang, and J.-J. Liu. "Photon-assisted tunneling through a topological superconductor with Majorana bound states". *AIP Adv.* 5.12 (2015), p. 127129. DOI: `10.1063/1.4939096`.

[Ter+06] M. Ternes, W. D. Schneider, J. C. Cuevas, C. P. Lutz, C. F. Hirjibehedin, and A. J. Heinrich. "Subgap structure in asymmetric superconducting tunnel junctions". *Phys. Rev. B* 74.13 (2006), p. 132501. DOI: `10.1103/PhysRevB.74.132501`.

[Tho+82] D. J. Thouless, M. Kohmoto, M. P. Nightingale, and M. den Nijs. "Quantized Hall Conductance in a Two-Dimensional Periodic Potential". *Phys. Rev. Lett.* 49.6 (1982), pp. 405–408. DOI: `10.1103/physrevlett.49.405`.

[TG63] P. K. Tien and J. P. Gordon. "Multiphoton process observed in the interaction of microwave fields with the tunneling between superconductor films". *Phys. Rev.* 129.2 (1963), pp. 647–651. DOI: `10.1103/PhysRev.129.647`.

[Uge+16] M. M. Ugeda et al. "Characterization of collective ground states in single-layer $NbSe_2$". *Nat. Phys.* 12.1 (2016), pp. 92–97. DOI: `10.1038/nphys3527`.

[UW05] Y. Uzawa and Z. Wang. “Coherent Multiple Charge Transfer in a Superconducting NbN Tunnel Junction”. *Phys. Rev. Lett.* 95 (1 2005), p. 017002. DOI: `10.1103/PhysRevLett.95.017002`.

[Vai+20] S Vaitiekėnas, Y Liu, P Krogstrup, and C. Marcus. “Zero-field Topological Superconductivity in Ferromagnetic Hybrid Nanowires”. *arXiv preprint arXiv:2004.02226* (2020).

[VF13] M. Vazifeh and M. Franz. “Self-organized topological state with Majorana fermions”. *Phys. Rev. Lett.* 111.20 (2013), p. 206802. DOI: `10.1103/PhysRevLett.111.206802`.

[WZ17] J. Wang and S.-C. Zhang. “Topological states of condensed matter”. *Nat. Mater.* 16.11 (2017), pp. 1062–1067. DOI: `10.1038/nmat5012`.

[Web+11] F. Weber, S. Rosenkranz, J.-P. Castellan, R. Osborn, R. Hott, R. Heid, K.-P. Bohnen, T. Egami, A. H. Said, and D. Reznik. “Extended Phonon Collapse and the Origin of the Charge-Density Wave in $2H-\mathrm{NbSe}_2$”. *Phys. Rev. Lett.* 107.10 (2011), p. 107403. DOI: `10.1103/PhysRevLett.107.107403`.

[Weg71] F. J. Wegner. “Duality in Generalized Ising Models and Phase Transitions without Local Order Parameters”. *J. Math. Phys.* 12.10 (1971), pp. 2259–2272. DOI: `10.1063/1.1665530`.

[Wen95] X.-G. Wen. “Topological orders and edge excitations in fractional quantum Hall states”. *Adv. Phys.* 44.5 (1995), pp. 405–473. DOI: `10.1080/00018739500101566`.

[Xi+15] X. Xi, L. Zhao, Z. Wang, H. Berger, L. Forró, J. Shan, and K. F. Mak. “Strongly enhanced charge-density-wave order in monolayer NbSe 2”. *Nat. Nanotechnol.* 10.9 (2015), p. 765. DOI: `10.1038/nnano.2015.143`.

[Xi+16] X. Xi, Z. Wang, W. Zhao, J.-H. Park, K. T. Law, H. Berger, L. Forró, J. Shan, and K. F. Mak. “Ising pairing in superconducting NbSe$_2$ atomic layers”. *Nat. Phys.* 12.2 (2016), pp. 139–143. DOI: `10.1038/nphys3538`.

[Xin+17] Y. Xing, K. Zhao, P. Shan, F. Zheng, Y. Zhang, H. Fu, Y. Liu, M. Tian, C. Xi, H. Liu, et al. “Ising superconductivity and quantum phase transition in macro-size monolayer NbSe2”. *Nano Lett.* 17.11 (2017), pp. 6802–6807. DOI: `10.1021/acs.nanolett.7b03026`.

[Yaz+97] A. Yazdani, B. A. Jones, C. P. Lutz, M. F. Crommie, and D. M. Eigler. “Probing the Local Effects of Magnetic Impurities on Superconductivity”. *Science* 275.5307 (1997), pp. 1767–1770. DOI: `10.1126/science.275.5307.1767`.

[Yok+01] T. Yokoya, T. Kiss, A. Chainani, S. Shin, M. Nohara, and H. Takagi. “Fermi Surface Sheet-Dependent Superconductivity in $2H$-NbSe$_2$”. *Science* 294.5551 (2001), pp. 2518–2520. DOI: `10.1126/science.1065068`.

[Yu65] L. Yu. “Bound state in superconductors with paramagnetic impurities”. *Acta Phys. Sin* 21.1 (1965), pp. 75–91. DOI: `10.7498/aps.21.75`.

[Zak89] J. Zak. “Berry’s phase for energy bands in solids”. *Phys. Rev. Lett.* 62.23 (1989), pp. 2747–2750. DOI: `10.1103/physrevlett.62.2747`.

[Zan+19] D. M. T. van Zanten et al. “Photon Assisted Tunneling of Zero Modes in a Majorana Wire” (2019). arXiv: `1902.00797`.

[ZCL16] Q.-B. Zeng, S. Chen, and R. Lü. “Generalized Aubry-André-Harper model withp-wave superconducting pairing”. *Phys. Rev. B* 94.12 (2016), p. 125408. DOI: `10.1103/physrevb.94.125408`.

[Zha+17a] H. Zhang et al. “Ballistic superconductivity in semiconductor nanowires”. *Nat. Commun.* 8.1 (2017). DOI: `10.1038/ncomms16025`.

[Zha+17b] X. L. Zhao, Z. C. Shi, C. S. Yu, and X. X. Yi. “Influence of localization transition on dynamical properties for an extended Aubry–André–Harper model”. *J. Physics B* 50.23 (2017), p. 235503. DOI: `10.1088/1361-6455/aa92df`.

[ZK96] U. Zimmermann and K. Keck. “Multiple Andreev-reflection in superconducting weak-links in the interaction with external microwave-fields”. *Z. Phys. B* 101.4 (1996), pp. 555–560. DOI: `10.1007/s002570050245`.

[Žit16] R. Žitko. “Spectral properties of Shiba subgap states at finite temperatures”. *Phys. Rev. B* 93.19 (2016). DOI: `10.1103/physrevb.93.195125`.

PUBLICATIONS

This doctoral thesis is based in the following publications:

[Lie+19] E. Liebhaber, S. Acero González, R. Baba, G. Reecht, B. W. Heinrich, S. Rohlf, K. Rossnagel, F. von Oppen, and K. J. Franke. “Yu-Shiba-Rusinov states in the charge-density modulated superconductor NbSe2”. *Nano Lett.* (2019). DOI: `10.1021/acs.nanolett.9b03988`

[AG+20] S. Acero González, L. Melischek, O. Peters, K. Flensberg, K. J. Franke, and F. von Oppen. “Photon-assisted resonant Andreev reflections: Yu-Shiba-Rusinov and Majorana states”. *Phys. Rev. B* 102.4 (2020). DOI: `10.1103/physrevb.102.045413`

[Pet+20] O. Peters, N. Bogdanoff, S. Acero González, L. Melischek, J. R. Simon, G. Reecht, C. B. Winkelmann, F. von Oppen, and K. J. Franke. “Resonant Andreev reflections probed by photon-assisted tunnelling at the atomic scale”. *Nat. Phys.* (2020). DOI: `10.1038/s41567-020-0972-z`

[AGO20] S. Acero González and F. von Oppen. “Topological Engineering in a Modulated Su-Schrieffer-Heeger Model”. *To be published* (2020)

Other publications:

[Ace+15] S. Acero, L. Brey, W. J. Herrera, and A. L. Yeyati. “Transport in selectively magnetically doped topological insulator wires”. *Phys. Rev. B* 92.23 (2015). DOI: `10.1103/physrevb.92.235445`

Acknowledgements

First, I would like to thank my advisor, Felix, for the opportunity of working under his supervision and learning from him. I do think that his physical intuition and guidance have shaped the way I approach physical problems and think about them. His good-humored nature and high human quality made working with him particularly enjoyable. Secondly, I would like to thank Katharina Franke and her group, specially Eva and Olof, for the productive collaborations that made this thesis possible. I would also like to thank Marietta for her help, professionalism and friendliness.

I am grateful for having met wonderful colleagues at the department. I say thanks to Christian Klöckner, eternal office companion, who ventured into Hezekiah's darkness by my side and whose input was often of help. I say thanks to my friends Laëtitia Farinacci and Max Geier. To José Manuel and Colin for the hundreds of hours we spent 'together'. To Jonas, Kevin and Luka. To Jacob, Peter, Larissa and Zoe. To Josias, Daniel, Andishe and Benjamin. To Andi, Markus and Alex. To anyone who came to a Boardgame Evening and to The Guardian for its crosswords.

I am thankful to my brother, Víctor, and my mother, Nélida, who never doubted me and were always supportive. I am also grateful to my father, Javier, from whom I believe I inherited a taste for science and whom we lost recently. I love the three of you.

Finally, I am unspeakably grateful to my partner, Florina, for her advice, patience, support, brightness and laughter. Her bowls of yogurt with fruit saw me through the darkest moments of the writing.

CURRICULUM VITAE

For reasons of data protection, the curriculum vitae is not published in the electronic version.